DEVELOPMENT OF LASER ULTRASONIC AND INTERFEROMETRIC INSPECTION SYSTEM FOR HIGH-VOLUME ON-LINE INSPECTION OF MICROELECTRONIC DEVICES

A Thesis Presented to
The Academic Faculty

By
Abel Valdes

In Partial Fulfillment
of the Requirements for the Degree
Master of Science in Mechanical Engineering

Georgia Institute of Technology
May 2009

DEVELOPMENT OF LASER ULTRASONIC AND INTERFEROMETRIC INSPECTION SYSTEM FOR HIGH-VOLUME ON-LINE INSPECTION OF MICROELECTRONIC DEVICES

Approved by:

Dr. I. Charles Ume, Chairman
School of Mechanical Engineering
Georgia Institute of Technology

Dr. Kyriaki Kalaitzidou
School of Mechanical Engineering
Georgia Institute of Technology

Dr. J. Rhett Mayor
School of Mechanical Engineering
Georgia Institute of Technology

Date Approved: May 2009

Acknowledgements

First, I would like to thank my advisor, Professor I. Charles Ume for his support and guidance, for allowing me to explore my interests, and for helping me to develop as an engineer.

I would like to acknowledge the financial and technical supporters of this research: National Science Foundation (NSF), Siemens AG, and Intel Corporation.

I would like to thank my colleagues, Dr. Jin Yang, Jie Gong, Tsun-Yen Wu, Matt Rogge, Tyler Randolph, and Razid Ahmad for their support and encouragement.

I would also like to thank my thesis reading committee members: Professors Kyriaki Kalaitzidou and. Rhett Mayor.

Table of Contents

List of Tables

List of Figures

Summary

Consumer demands and advances in microelectronic devices continue to drive industry towards more compact, cheap, reliable, and integrated electronic packaging solutions. The industry has met these demands by evolving from through-hole to surface mount technologies (SMT), such as flip chip packages (FCPs), chip scale packages (CSPs), ball grid arrays (BGAs), and land grid arrays (LGAs). These packaging technologies have achieved the previously stated goals by using solder bumps as mechanical and electrical interconnects between the devices and the substrates/printed wiring boards (PWBs). Since the solder bumps are located between the device and the substrate, the complete area of the chip can be used to maximize the number of input/outputs. However, this also makes it difficult to inspect for solder bump defects.

Nondestructive inspection methods have been crucial to the development of the microelectronics packaging industry, aiding the industry in reducing manufacturing costs, improving yields, and ensuring product quality and reliability. New inspection techniques are needed to fill the gap between available inspection capabilities and the industry's requirement for low-cost, fast, and highly reliable inspection systems. The laser ultrasonic and interferometric inspection system under development aims to provide a solution that can overcome some of the limitations of current inspection techniques.

The laser ultrasonic and interferometric inspection technique utilizes a high-power pulsed laser to generate ultrasonic waves on the device surface, exciting structural vibration. An interferometer is used to measure the vibration displacement of the chip's surface at several inspection points. Since defective interconnects cause changes in the vibration of the device, quality can be assessed by comparing the vibration response of

the sample under inspection to the response of a known good device. Previous research has demonstrated the utility of this technique in detecting solder bump defects in FCPs, CSPs, chip capacitors, and other surface mount devices. However, some challenges still need to be met to make the laser ultrasonic technique directly applicable to high-volume, on-line inspection of packaged electronic devices. The research presented in this thesis focuses on the continued development of this technique towards expanding its application scope to high-volume, on-line inspection. This thesis has the following research objectives: 1) Develop a method that can be used to analyze measurements taken with the laser ultrasonic and interferometric inspection system without requiring a previously established reference device. 2) Develop an excitation/measurement scheme capable of providing a strong vibration response in high-density and stiff devices. 3) Improve system repeatability by designing and testing a calibration fixture/method which allows measurements taken before and after any system modifications to be comparable. 4) Characterize the laser energy density delivered to the device surface as a function of laser power and laser spot size. 5) Design a process to experimentally determine the threshold for surface damage for a particular device/surface as a function of laser energy density.

The realization of these research objectives will improve the overall utility of the laser ultrasonic inspection technique for on-line inspection applications where no other nondestructive methods are currently available.

Chapter 1: Introduction

The progression of electronic packaging technology from traditional through-hole assembly to surface mount assembly has accomplished a significant step in the evolution of microelectronic devices, by increasing I/O density while continuing to reduce package size. Advances in the field of microelectronic devices, as well as the move toward system-on-chip (SoC) and system-in-package solutions, have triggered research into new advanced electronic packaging technologies to improve device performance, functionality, and reliability. In many ways, electronic packaging research is given the same if not more importance than the silicon wafer that it incorporates.

These new packaging technologies are needed to support system integration and the increasing complexity of devices which require a higher number of I/Os, lower power consumption, better connectivity, and finer pitch while also preserving quality and reliability. Surface mount packaging technologies, such as FCPs, CSPs, BGAs, and LGAs have become vital for the development of next-generation devices. These packaging technologies provide a high I/O density by utilizing solder bump interconnects which can be placed on the entire device surface and lie between the devices and the substrates/PWBs, as shown in Figure 1.0.1. Surface mount packages reduce package size, increase I/O density, improve package reliability, and reduce cost of assembly.

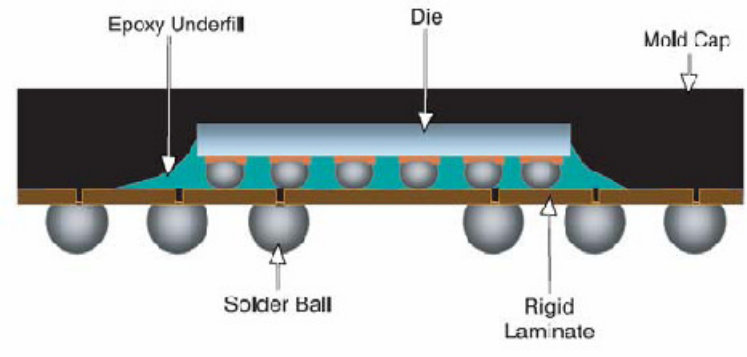

Figure 1.0.1 BGA device with solder bump die packaging

As these advanced packaging technologies progress and continue to push the envelope in materials, manufacturing, and assembly capabilities, reliability and quality become increasingly important. Reliability of microelectronic devices is a critical issue because most applications have long life cycles where the devices are often exposed to extensive power and thermal cycling, vibration and other mechanical loads and are often exposed to environmental stresses. The manufacturing process and device architecture can also have a significant effect on the reliability of the packaged device. Common manufacturing defects in solder bump interconnects include cracked, head-in-pillow (HIP), open, shorted, starved, misaligned, missing, and voids. Table 1.0.1 shows the distribution of common defects in solder bumps interconnects. Thermal cycling due to reflow, rework, and power cycles are also sources for cracked solder bumps that can appear during the effective life of the device. Current trends, such as decreasing pitch, decreasing diameter, vertical integration, and lead-free solder materials, will further intensify the focus on packaging research, with a special emphasis on quality and reliability. These trends place an ever-increasing importance on technologies that are capable of identifying solder bump defects in manufacturing and research applications to

help reduce cost. Inspecting solder bump interconnects is a challenging endeavor because they are hidden from view between the device and substrate, and modern packages can have hundreds to thousands of interconnects. Assessing interconnect quality is a critical part of ensuring device reliability, because even small defects can propagate and become dominant factors during the life cycle of the device.

Table 1.0.1 Typical solder bump interconnect defects

Defect Type	Percent Occurrences
Open joint	48%
Short joint	23%
Starved solder	15%
Misaligned joint	4%
Missing joint	4%
Void in joint	2%
Excess solder	2%
Other	2%

There are three main, commercially available nondestructive methods for inspection of solder bump interconnects: electrical testing, acoustic inspection, and x-ray inspection. These methods are suitable for certain inspection tasks but often fail to identify the root cause of failure or to access the integrity of the assembly as a whole. Also, none of these methods is able to provide the throughput necessary for high-volume, on-line inspection while providing an adequate assessment of interconnect quality. The laser ultrasonic inspection system under development aims to provide a solution that can overcome some of the limitations of the current inspection techniques. A fully developed system will be capable of inspecting hidden solder joints with multiple defect types, including, but not limited to, missing solder bumps, misaligned IC chips, HIP, open solder joints, solder joint cracks, and other defect types that are difficult or impossible to evaluate using current nondestructive inspection methods.

1.1 Nondestructive Inspection Methods for Packaged Microelectronic Devices

Before the widespread use of surface mount devices, machine vision systems could be used for real-time inspection of solder joints. These techniques were able to detect the shape of solder interconnects and could use it to infer quality. Vision-based systems are still utilized to inspect the size, shape, and placement of solder bumps before the device is placed over them, but they cannot be used after reflow. Currently, high-volume nondestructive testing of interconnects is performed via electrical testing. This method tests the electrical functionality of devices by applying controlled electrical inputs to the device and accompanying circuitry while examining the electrical response. This method is usually implemented in the form of in-circuit or functional testing [Tummala R., 2001].

In-circuit testing checks the conductivity of interconnections and can be performed at several levels of the package assembly because it does not require a functioning device. Functional testing verifies the device functionality by exercising a variety of test functions and not only tests the package assembly but also its intended performance. Functional testing is capable of testing many levels of device operation and is crucial in testing a device before it is integrated into an end product, but it often lacks the ability to locate specific failures. Electrical testing is a cost-effective way to check interconnect quality but lacks the ability to pinpoint specific faulty interconnects and cannot detect defects where there is still solder contact, such as in partial cracks, voids, starved solder, and misalignments [Yang, J., 2008]. In addition, both of these forms of electrical inspection are time consuming, lack resolution, and require additional space on

the substrate for contact pads, becoming more impractical as interconnect density, integration, and complexity increase

Acoustic inspection methods are also widely applied in the electronic packaging industry as a way to detect cracks, voids, and delamination in microelectronic devices. Acoustic inspection generates images of the device by interpreting the reflection and refraction of ultrasonic waves transmitted through a coupling medium to the device. Scanning acoustic microscopy (SAM) uses an ultrasound (10 MHz to 2 GHz) point source to sample across the surface while capturing the reflections at a particular depth [Yang, J., 2008]. Although SAM and other ultrasonic techniques are commonly applied, they have several drawbacks which limit their application scope. First, the technique provides poor resolution and requires an experienced operator to interpret the generated images. Second, the need for an acoustic coupling medium causes problems in tightly packed spaces, and is therefore unsuitable for devices with solder bump interconnects. Although these nondestructive techniques are valuable in some applications, they have a limited scope in on-line testing because of the long inspection time and the need to immerse the device in an acoustic coupling medium.

Several x-ray imaging methods, such as radiography, laminography, and tomography, are routinely utilized in nondestructive inspection of microelectronic devices for process development and on-line inspection [O'Conchuir D., 1991, Goyal D., 2000]. The short wavelength of x-ray emissions allows for good penetration across the package materials, and a digital camera can be used to convert them to images for interpretation. The simplest method is radiography, which provides 2D images by transmitting the x-rays through the opaque materials to the detector on the other side.

Although fast and easily implemented, radiography produces images that are difficult to interpret, and it cannot detect defects such as solder bump cracks or to inspect multilayer devices. Laminography is able to produce layered images of virtual slices of the sample by changing the angle of observation of the sensor, therefore providing some depth information. Although able to provide adequate resolution, x-ray laminography is often impractical because of high operating and equipment costs. Tomography follows a similar principle, but by rotating the x-ray source and detector, it can reconstruct a 3D image of the device and therefore provide a virtual cross-section of the package. X-ray tomography is able to provide the resolution to effectively detect most defects in interconnects, but because of the long data acquisition and post processing times and the high equipment and operating costs, it is impractical for most applications.

The nondestructive inspection methods presented are crucial to the microelectronics industry as quality and process development tools, but their cost and low throughput limit their applications in high-volume and on-line inspection. The laser ultrasonic inspection system under development aims to provide a solution that can overcome some of the practical limitations of current nondestructive inspection techniques.

1.2 Laser Ultrasonic and Interferometric Nondestructive Inspection System

Previous researchers have demonstrated the utility of laser ultrasonic inspection for non-destructive evaluation of interconnect quality in packaged electronic devices, such as FCPs, CSPs, wafer-level packages, BGAs, LGAs, and chip capacitors. This noncontact and nondestructive inspection technique has great potential for manufacturing applications where on-line inspection after device assembly may be performed to analyze

device quality and to aid in process control and development. Figure 1.2.1 shows the operating principle of the laser ultrasonic and interferometric technique. A high-power pulsed laser focused on the device surface generates stress waves that induce vibrations. Meanwhile, an interferometer is used to measure the out-of-plane displacement. Device quality can then be assessed by comparing the vibration response of the device under inspection to the response of a known-good reference device.

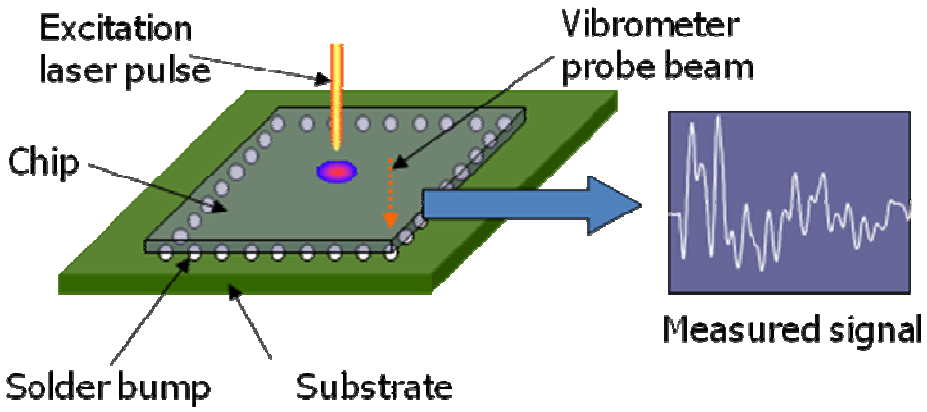

Figure 1.2.1 Principles of laser ultrasonic inspection of microelectronic devices

The laser ultrasonic inspection system utilizes several integrated subsystems to generate vibrations in microelectronic devices and to measure the response. Figure 1.2.2 shows a schematic representation of the whole system. The main components include an Nd:YAG pulsed laser for ultrasound generation, a fiber optic delivery system to transmit and focus the laser pulses to the device surface, a laser vibrometer (interferometer) to measure the out-of-plane displacement of the device, a manual X-Y stage to control the location of the excitation laser on the device surface, an automated X-Y stage to position the inspection locations on the device surface under the interferometer, a machine vision

system to perform calibration measurements, and a PC for motion control, data capture, and calibration.

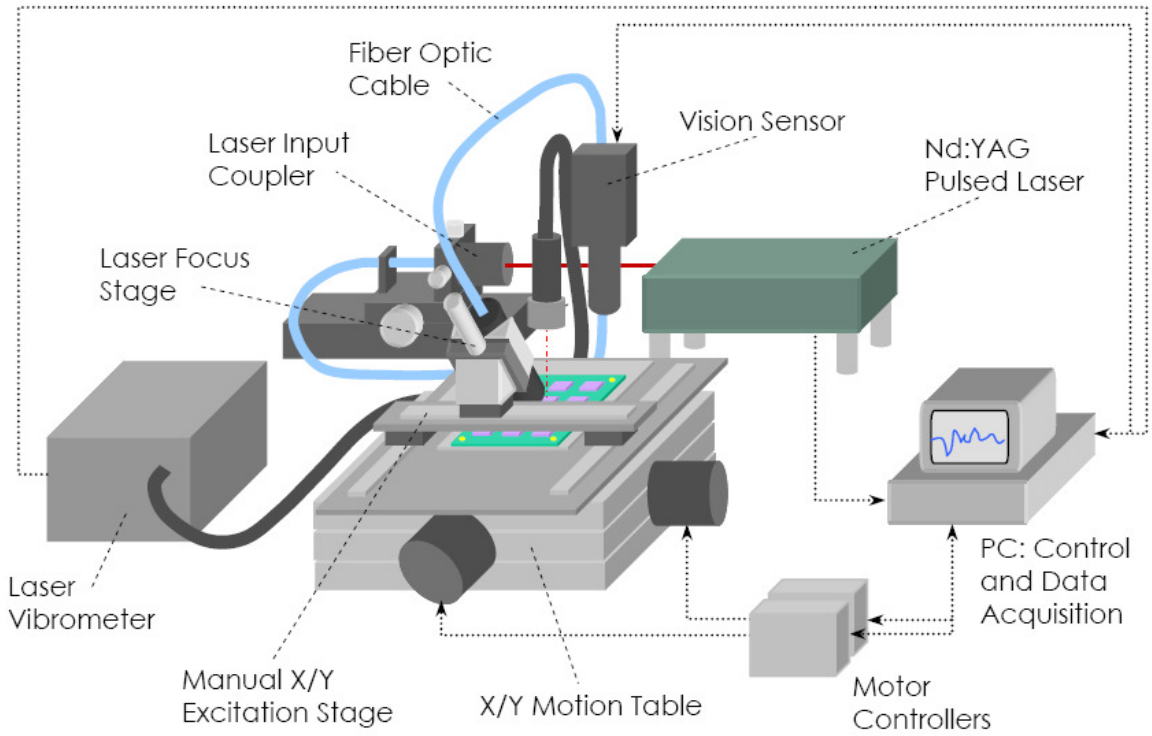

Figure 1.2.2 Laser ultrasonic and interferometric inspection system schematic

The source of the laser-generated ultrasound is a Q-switched Nd:YAG laser outputting 5 nanosecond pulses at a 20 Hz repetition rate and with a wavelength of 1064 nm. The laser pulse energy is controlled by an optical attenuator which can deliver a maximum energy of 45 mJ per pulse. The laser power is measured with a calorimeter and adjusted prior to taking measurements.

The laser emitter is aligned to a focusing lens that is the input for a 600 µm high-damage-threshold fused silica optical fiber that is packaged in a rugged sheath. At the other end of the fiber are a collimating lens and a focusing objective [Howard T., 2002]. Figure 1.2.3 shows the laser delivery system components. The focusing objective is

attached to a manual, micrometer controlled unidirectional stage that can be moved to adjust the laser focus for different spot sizes and device heights. The stage is placed at a 45° angle to keep the focusing objective from obstructing the interferometer beam. This delivery method allows the laser to be positioned remotely, while maintaining the flexibility to place the ultrasound source anywhere on the device. The focusing objective and manual offset positioning stage are shown in Figure 1.2.4

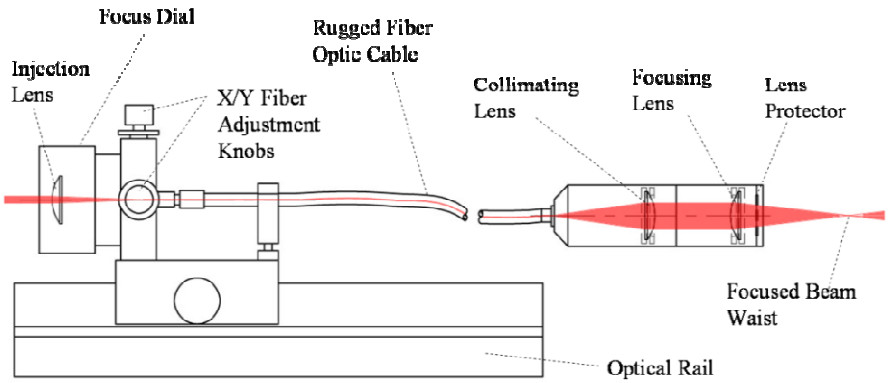

Figure1.2.3 Fiber optic laser delivery and focusing objective

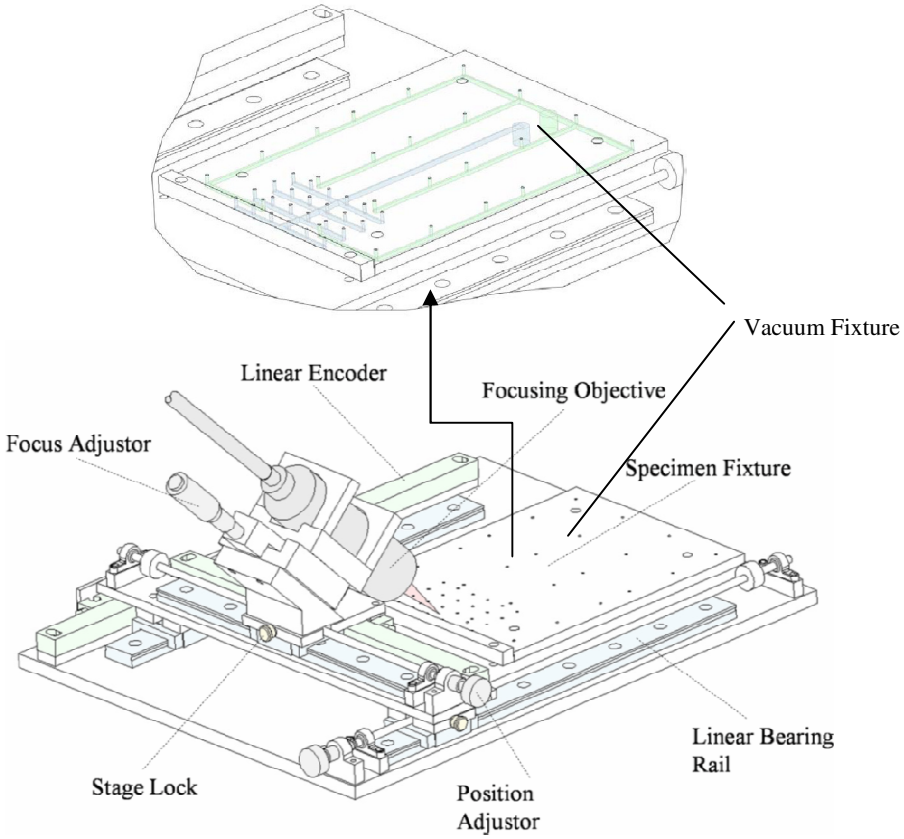

Figure 1.2.4 Vacuum fixture, laser positioning stage, and focusing objective

The substrate carrying the devices under inspection is held in place using a vacuum fixture. The vacuum, generated by compressed air and a venturi vacuum pump, is delivered by a flat manifold with 48 orifices that can support 150 mm by 200 mm boards. The vacuum manifold is attached to the top of an automated X-Y positioning stage that moves the sample under the interferometer. The manufacturer specifies an accuracy of 7.5 μm per 100 mm of travel and an orthogonality error less than 7.5 arc-seconds, with a bidirectional repeatability of ±1 μm [Yang J., 2008]. Accurate and precise positioning of this stage is crucial to the repeatability of measurements utilizing this system, because the stage controls the location where the interferometer is measuring the out-of-plane displacement caused by the propagation of laser generated ultrasound.

This stage is automatically controlled to move to the inspection points during testing and has an experimentally determined repeatability of ±6 μm in the X-direction and ±4 μm in the Y-direction [Howard T., 2002].

The stage controlling the focusing of the excitation laser is positioned at 45º angle with respect to the horizontal plane and placed on a roller bearing X-Y stage on top of the automated X-Y stage. The stage position is measured using 1 μm resolution encoders with an estimated precision of ±10 μm [Howard T., 2002]. This stage is moved to control the location on the device where the laser is incident on the device surface. Since the focusing objective is mounted on the same X-Y positioning stage as the vacuum fixture and device under inspection, the location of the focused laser spot remains constant for all inspection positions.

Fiducial marks are usually circular, square, or cross-shaped solid pads on the PWBs used for the placement of critical components. In this system, they are used to precisely align the test specimen. The camera used to capture the location of these features is an integrated stand-alone vision system with an 8-bit 480 by 640 pixel resolution CCD camera and a field of view of 3.6 mm by 4.8 mm. This corresponds to an image resolution of 7.5 μm by 7.5 μm pixels. The camera software uses several image transformations to separate the fiducials or other desired features from the background and to measure how far they are from the center of the CCD coordinate frame. The software also allows for compensation of lens distortion and varying lighting conditions. Figure 1.2.5 shows the separation of the fiducial feature, which can be measured with a resolution of ±1.0 μm [Zhang L., 2005].

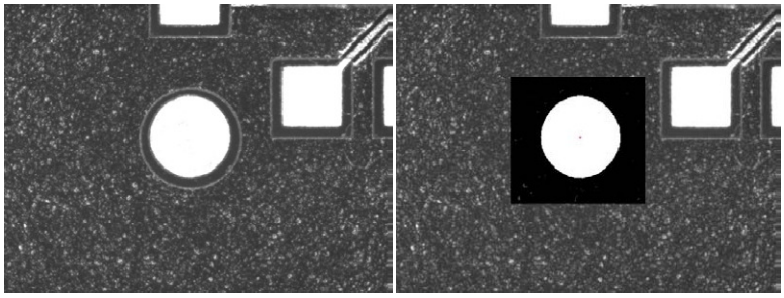

Figure 1.2.5 Fiducial blob identification

A laser Doppler vibrometer is used to measure the transient out-of-plane displacement of the device during laser ultrasound excitation. The heterodyne optical fiber interferometer has a remote optical sensor head with an objective lens that can focus the laser beam to a spot 3 μm in diameter, giving it a high spatial resolution. The focusing lens is mounted on a cantilevered beam over the X-Y positioning stage, perpendicular to the device under inspection. The interferometer has a maximum measurable displacement of 150 nm peak to peak, a resolution of 0.3 nm, and a response bandwidth of 50 kHz to 25 MHz. The analog signal output for this interferometer is 50 nm/V analog signal output, which is captured by a 12-bit data acquisition card operating at 25 MHz.

To locate the devices, inspection points, and excitation locations, Howard developed a set of coordinate frames to describe the location of all important components [Howard, T., 2002]. The coordinate system displayed in Figure 1.2.6 is based on four frames of reference: CCD, FIXTURE, BOARD and CHIP. CCD is located at the center of the positioning camera's field of view, FIXTURE is located at the (0, 0) position of the automated X-Y positioning stage, BOARD is a user-defined location on the substrate, and CHIP is the location on the device from which the laser excitation location and the

inspection points are defined. These coordinate frames will be referred to when performing the system calibration prior to an inspection. A coordinate transformation is performed to transfer all measurements and user input into the FIXTURE frame, which corresponds to the automated X-Y positioning stage.

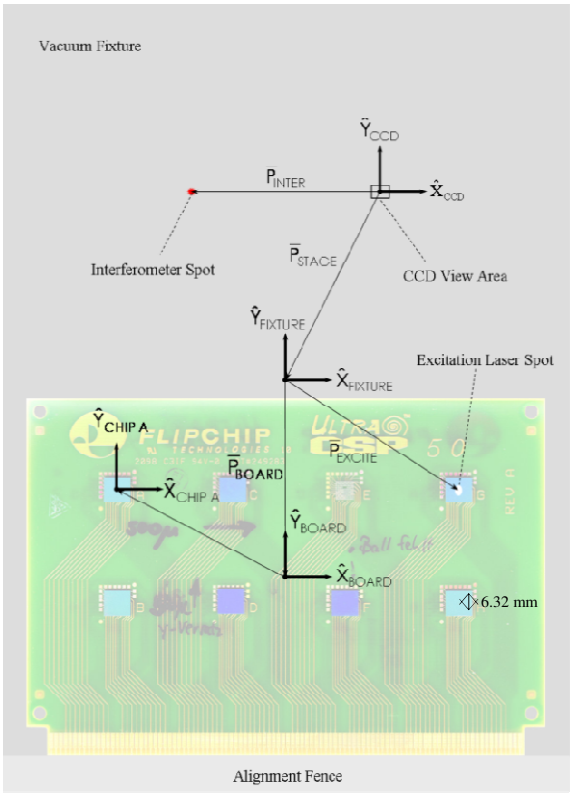

Figure 1.2.6 Coordinate frames of reference for component location

1.3 Laser Generated Ultrasound

Laser ultrasonic techniques utilize a high-power pulsed laser to generate elastic waves in a medium. These acoustic waves cover a frequency range from 20 kHz to 20 MHz. Laser ultrasound generation is typically classified into two extreme regimes: thermoelastic and ablative [Scruby et al (1990), Davies et al (1993)]. The ablative regime

is defined by the presence of a strong normal force component caused by the generation of plasma at the surface. At low power levels of the thermoelastic regime, surface damage is avoided, but the normal force component is lost. Each of these regimes, shown in Figure 1.3.1, provides a distinct source for ultrasonic wave propagation.

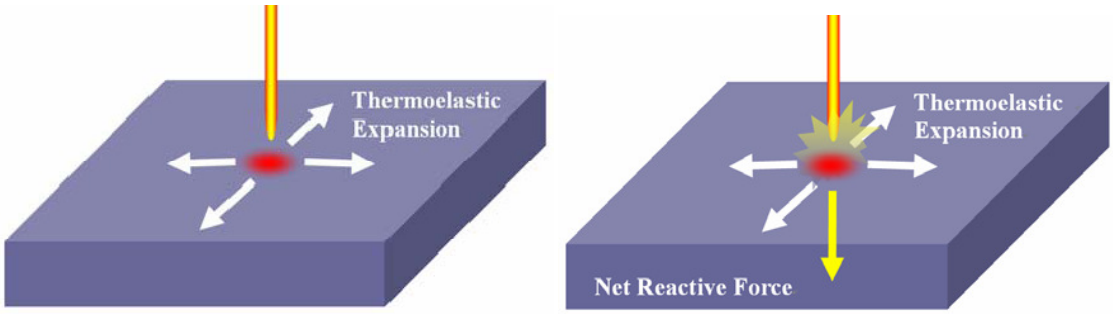

a) Thermoelastic regime b) Ablation regime

Figure 1.3.1 Ultrasound generation regimes in a solid medium

When a laser is incident on a surface, some of the electromagnetic radiation is absorbed by the electrons on the sample surface, causing rapid local heating, while the remaining energy is reflected. The resulting steep thermal gradient generates the stress and strain fields of the elastic waves by thermal expansion. The temperature gradient is only a few microns deep, and therefore the ultrasound source can be approximated as a point source of expansion, with the principal stress components parallel to the surface and no normal component, as indicated in Figure 1.3.1a. In the thermoelastic regime, the amplitude of the ultrasonic waves increases linearly with the applied power density. Further increasing of the laser power density at the surface will start vaporizing the surface material. This ejected material produces a reactive stress predominantly normal to the surface, as shown in Figure 1.3.1b. In the ablative regime, the generation of compression and surface waves is enhanced with increasing power density, but amplitude

of the shear and of the waves will reach a maximum near the onset of ablation and then decrease [Scruby et al (1990)].

The laser ultrasonic technique under development operates within the thermoelastic regime to prevent damaging the package under inspection. Ablation is avoided by carefully choosing the power level and the area of the laser spot. In most electronic packaging materials, visible surface damage appears before the onset of a strong normal force component.

1.4 Signal Processing Methods

The development of signal processing methods capable of identifying the changes in vibration caused by solder bump defects is a fundamental part of the research efforts towards advancing laser ultrasonic inspection as a technique. The goal of these signal processing methods is to identify defective devices while providing the defect location and defect type. Several techniques and methods have been developed and employed by Yang, Zhang, and Liu to detect missing, cracked, and misaligned solder bumps. The laser ultrasonic inspection technique identifies defects by quantifying the difference in transient out-of-plane response between the device under inspection and a known-good reference device. Various approaches, including Error Ratio, Correlation Coefficient Method, Power Spectrum Analysis, Local Temporal Coherence Method and Wavelet Analysis, have been successfully applied to the inspection of FCPs, CSPs, BGAs, and chip capacitors [Yang J. 2008].

Liu introduced the Error Ratio (ER) method to directly compare signals in the time domain [Liu S., 2003]. This method quantified the difference between the reference

waveform r(t) and the measured waveform f(t) by integrating the squared difference over time and normalizing by the integral of the reference waveform squared. Although able to detect the waveform changes with enough sensitivity to identify certain solder bump defects, the ER was shown to be too sensitive to variations in laser power level and other experimental factors [Zhang L. 2005].

$$ER = \frac{\int [f(t) - r(t)]^2 dt}{\int [r(t)]^2 dt} \qquad (1.4.1)$$

$$where \begin{cases} r(t)\ is\ the\ reference\ signal \\ f(t)\ is\ the\ measurement\ signal \end{cases}$$

To address some of the problems associated with the Error Ratio, Zhang proposed the Modified Correlation Coefficient method (MCC). Generally speaking, the correlation coefficient or cross-correlation coefficient, as it is sometimes called, is a quantity that gives the quality of a least squares fitting to the original data. This method yields a correlation r, from 0 to 1 between the reference signal and the measurement signal according to Equation 1.4.2, where A and B are the row matrices containing the measurement signal data and reference signal data, respectively. The MCC values referred to in this thesis are (1-r), where r is a normalized measure of the strength of the linear relationship between the signals represented in matrices A and B, with an MCC value of *0* representing identical signals and *1* no correlation. This method has been demonstrated by various researchers to be effective in identifying the signal differences caused by missing, cracked, and misaligned solder bumps in flip chip, chip scale and BGA devices [Zhang L., 2005].

$$MCC = 1 - \frac{\sum_m \sum_n (A_{mn} - \bar{A})(B_{mn} - \bar{B})}{\sqrt{(\sum_m \sum_n (A_{mn} - \bar{A})^2)(\sum_m \sum_n (A_{mn} - \bar{A})^2)}} \quad (1.4.2)$$

$$where \begin{cases} A\ is\ the\ reference\ signal \\ B\ is\ the\ measurement\ signal \end{cases}$$

1.5 Inspection System Throughput

The throughput of an inspection system is a central factor in its implementation in on-line and high-volume applications. In this characteristic, the laser ultrasonic inspection system under development provides a clear advantage over x-ray and acoustic inspection techniques. This section will present an overview of the current and potential inspection throughput of the laser ultrasonic technique.

With the current system implementation, the total inspection time per boards is divided into two distinct steps; the setup calibration and the inspection measurements at each inspection location. The setup calibration process described in section 1.2 will not be included in the analysis of inspection as it will vary significantly as the level of system automation continues to improve. The inspection measurement time shown in Equation 1.5.1, consists of, positioning the X-Y stage for each inspection location, focusing the interferometer, and data acquisition.

The positioning time is determined by the speed of X-Y stage and the distance traveled between the inspection points. The speed achieved by the current X-Y positioning stage is approximately 5080 μm per second. The positioning time, S_t, is the time it takes the X-Y stage to go through all of the inspected locations divided by the number of inspected locations. The interferometer focusing time, F_t, varies according to the surface roughness of the device and refocusing may not be required at every

inspection location. An auto-focusing system developed by Randolph, has reduced the focusing time to approximately 2.1 seconds [Randolph, T., 2009]. Data acquisition time, F_t, takes 0.05 seconds per measurement, but the total time depends on the number of averages used to reduce noise. Depending on the quality of the interferometer signal, averaging is usually performed on 16, 32, 64 or 128 measurements at each inspection location.

$$I_t = \sum_{1}^{n} S_t + F_t + C_t$$

$$where \begin{cases} I_t : \ total\ inspection\ time \\ S_t : \ stage\ movements\ time \\ F_t : \ interferometer\ focusing\ time \\ C_t : data\ capture\ time \\ n : inspected\ locations \\ S_t = \left(\frac{total\ distance\ traveled}{5080_{\mu m/sec}}\right) / number\ of\ inspection\ locations \\ C_t = (0.05_{sec})(number\ of\ averages) \end{cases} \quad (1.5.1)$$

To determine the average inspection time for the current system implementation without auto-focusing, the inspection time for four different packages was extracted using the data logs for the measurements presented in this thesis. The four packages were, a BGA package with a rough plastic surface, a ceramic chip capacitor, a flip chip package with an etched silicon surface, and a high density flip chip device with a reflective gold coated surface. The inspection time is expressed as the average inspection time per inspected location.

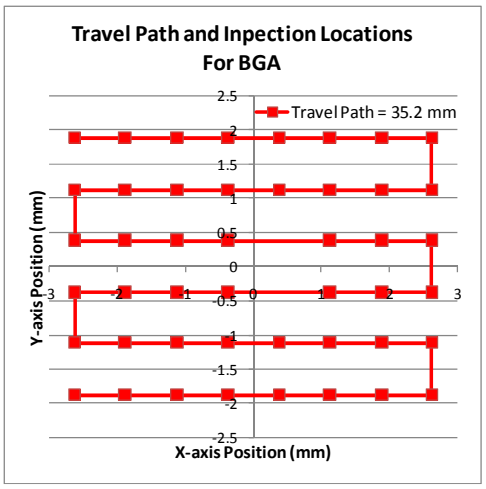

a) BGA

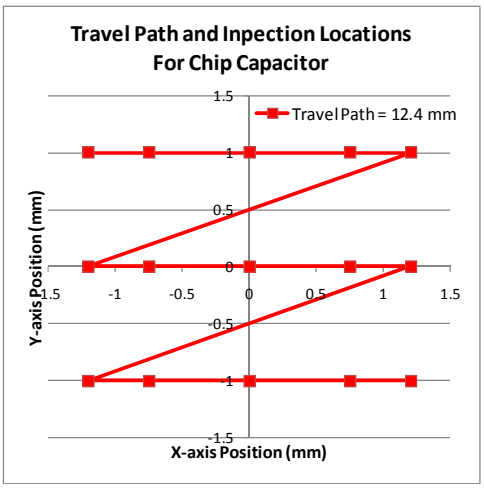

b) Chip Capacitor

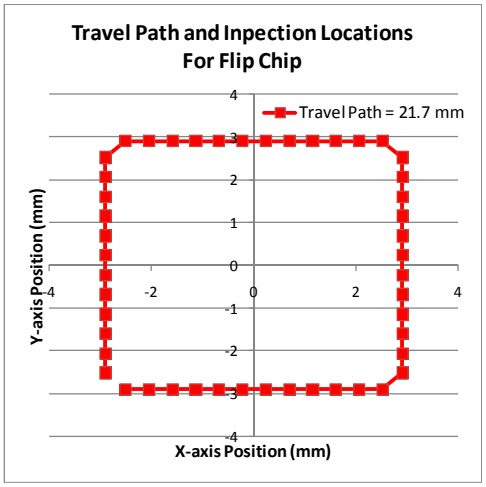

c) Flip Chip

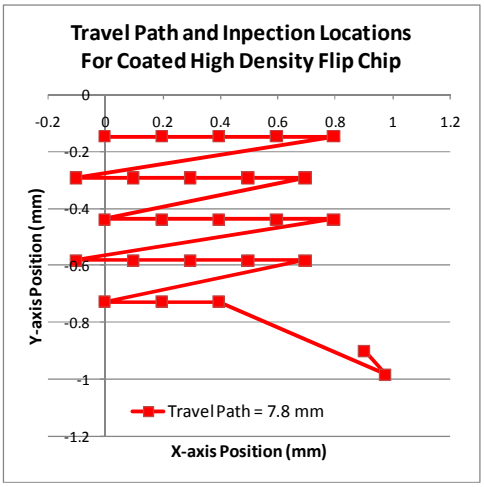

d) Coated Flip Chip

Figure 1.5.1 Inspection patters for inspected devices

The pattern for the inspection locations and total distance traveled are shown in Figure 1.5.1. The time it takes the X-Y positioning stage to move from one inspection location to the next, was calculated using the stage velocity; ramp-up time was small enough to be ignored. The stage movement time was found to be less than 1% of the total inspection time. The data collection time was 6.4 seconds for the BGA device, which required 128 measurement averages at every inspected location and 3.2 seconds for the

other three devices, which required only 64 averages. The focusing time is by far the most variable of the three factors in the inspection time. Devices with large surface roughness and low reflectivity require more frequent refocusing and longer focusing time. The focusing time was measured by subtracting stage movement and data collection time from the total inspection time. Table 1.5.1 and Figure 1.5.2 show the individual components of the average inspection time per inspection location and the standard deviation of the average inspection time, as calculated from the experimental data.

Table 1.5.1 Measured Average Inspection Time per Inspection Location

Package	Average Time (s)	Standard Deviation (s)	Focusing (s)	Stage Movement (s)	Data Collection (s)	Number of averages
BGA	51.96	25.97	45.54	0.02	6.40	128
Chip Capacitor	33.00	6.83	29.65	0.15	3.20	64
Flip Chip	18.68	9.45	15.39	0.09	3.20	64
Coated Flip Chip	7.46	0.95	4.19	0.07	3.20	64

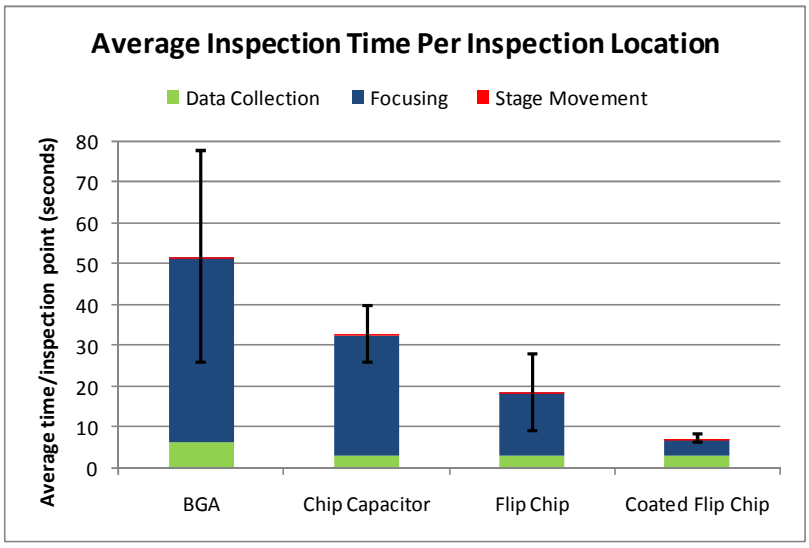

Figure 1.5.2 Inspection time per inspection point for four common packages

This section has presented the analysis of the theoretical throughput, per inspection location, of the inspection time for the current hardware implementation of the laser ultrasonic inspection system. The actual inspection time per inspected location is shown for the four test vehicles utilized in the research. The results presented can be used to estimate the total inspection time for future devices.

1.6 Measurement Resolution

The smallest defect that can be detected by this system is mainly determined by the sensitivity of the interferometer and by signal quality. In the current system, the minimum detectable displacement measurable by the interferometer is 0.25 nm. Therefore, solder joints defects must cause changes in the surface vibration of at least 0.25 nm before they can potentially be detected. To provide good signal quality, the laser Doppler vibrometer must also have enough light returning from the incident laser beam focused on the sample. In devices with rough/non-reflective surfaces, the amount of light returning to the sensor decreases, and the signal quality deteriorates. This causes an increase in noise, which can hide changes in vibration caused by the defects.

1.7 Sampling Inspection

Inspection refers to the gathering of information or measurements regarding the output of a process and the comparisons of these measurements with a standard or specification. In laser ultrasonic inspection, the specification is defined by the vibration response of the reference device. Quality is gauged according to the deviation from the reference response. This makes the selection of the reference vibration response a critical part of the design, accuracy, and outcome of the inspection process. Equal importance

must be given to the selection of the reference response as to the rest of the sampling plan [Hald, H, 1981].

A complete statistical model for sampling inspection, using a single attribute to measure quality, contains the following components: 1) The expected (prior) distribution of measured attributes according to quality. 2) The costs of inspection, acceptance, and rejection. 3) A method of sampling (sampling plan) designed to reduce the risk against rejecting good quality (alpha-risk) and accepting poor quality (beta-risk). Alpha-risk occurs when the inspection results conclude that the product quality is not acceptable when in fact it is. Alpha- risk incurs additional costs to the manufactures, as either loss of product or readjustments to production. Beta-risk is the opposite condition, it occurs when the inspection results conclude that a defective product is acceptable. These risks are transferred to either the producer or the customer. Knowledge of these components allows for a systematic approach to designing an inspection and sampling plan that reduces the average inspection costs and the risks associated with quality inspection. In practice, some of these parameters may not be available or may be costly to determine; therefore, most applications rely on an incomplete model to make inspection sampling decisions [Wetheril, B.G., 1969].

There are two categories of sampling or inspection plans: batch inspection or continuous inspection. In batch inspection, a group of items is accepted, rejected or otherwise classified according to the inspection results of a selected group. In contrast, continuous inspection treats every item individually during the process flow. Classification into one of these plans largely depends on the problem statement. For example, in the assembly of electronic components, batch inspection might be used to

accept or reject all of the devices placed in an assembly process during a period of time or process interval. Continuous inspection would be used to assess the quality of each component independently to make a pass/fail decision individually. Another option in this example would be to treat individual boards as batches and the pass/fail decision for that board is based on the assessment of a few components. In the research presented in this thesis, a continuous sampling of every device is assumed. Therefore, every device is inspected and its quality assessed according to the individual results of laser ultrasonic inspection.

The following chapter focuses on the calibration and characterization of the laser ultrasonic and interferometric inspection system. Chapter 3 presents the hardware implementation and validation of a new local laser-ultrasound generation and measurement scheme. A method for identifying suitable reference devices without a pre-established reference response is discussed in Chapter 4. The results for the inspection of a high-density flip chip package are shown in Chapter 5. Summary, contributions and recommendations for future work are presented in Chapter 6.

Chapter 2: Calibration of the Laser Ultrasonic and Interferometric Inspection System

This chapter discusses improvements of the calibration and characterization of the laser ultrasonic inspection system being developed. The first topic addresses the image processing algorithms that extract the reference fiducials used to locate the substrate and the devices when the manufacturer has not provided these coordinates. Second, the chapter presents a fixture and a procedure for determining the vector P_{inter} that describes the relative position of the interferometer laser spot with respect to the center of the CCD camera. As shown in Figure 1.2.6, this vector is used to transfer the coordinates of the reference fiducials and devices from the CCD camera frame to the interferometer frame. This calibration method improves the precision of the P_{inter} measurements, which allows for the correlation of data taken before and after any hardware modifications. Finally, a discussion of the calibration of the laser energy density as a function of the position of the laser focusing objective leads to the characterization of the laser spot size. This information is used to experimentally determine the ablation threshold as a function of the laser energy density.

2.1 Device Coordinate Measurements

Accurate information about the locations of the fiducials and the devices is needed to inspect a microelectronic device using the laser ultrasonic inspection system. Two sets of coordinates are required to set up the movement of the automated X-Y positioning stage and to define the inspection locations: first, the location of the reference features (fiducials) used to compensate for the position and rotation of the board on the X-Y stage; and second, the location of the individual devices with respect to these

fiducials to define the inspection points. This coordinate information is usually extracted from a CAD file of the substrate or is explicitly provided by the manufacturer of the device. When this information is not available, these measurements can be made using the procedure discussed in this section.

The image capture method used to obtain the coordinate information has a measurement resolution of 2.5 µm and provides a flexible approach for capturing this important data by extracting the features from high-resolution images of the board and devices. The images are captured using a flatbed scanner to reduce lens distortion and to achieve very high resolutions. The board is scanned at a resolution of 5000 dpi (dots per inch), which translates to 5 µm per pixel. An image processing algorithm implemented in Matlab separates the fiducials and the devices from the background and measures their relative locations. The algorithm can be easily modified to compensate for the variety of colors and surface finishes of the desired features shown in Figure 2.1.1.

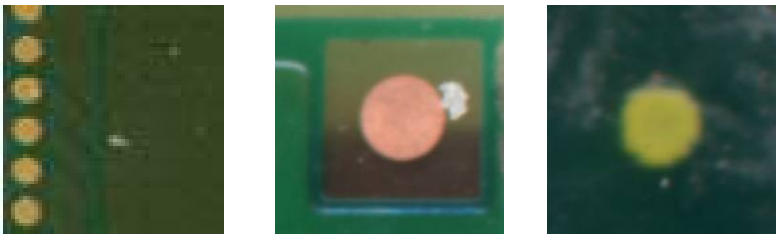

Figure 2.1.1 Sample fiducials with different surface finishes

This approach was first taken when testing the chip capacitors shown in Figure 2.1.2. The devices were soldered on two boards that were manually cut by the manufacturer and, therefore, not identical. Each board had different fiducials and

capacitor locations. The method was also used to capture the geometric information for the flip chip device shown in Figure 2.1.4.

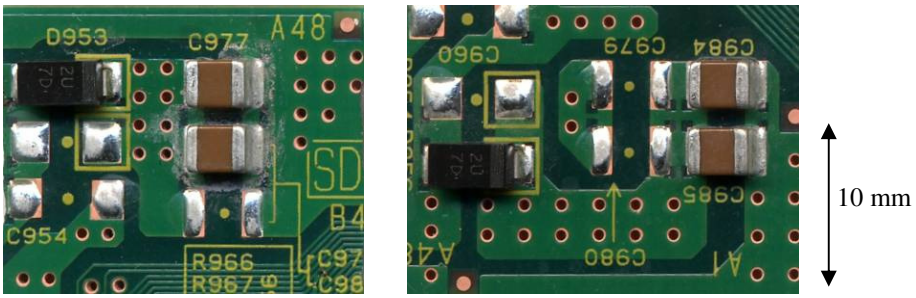

(a) Board A (b) Board B

Figure 2.1.2 High-resolution scanned images of two boards with chip capacitors

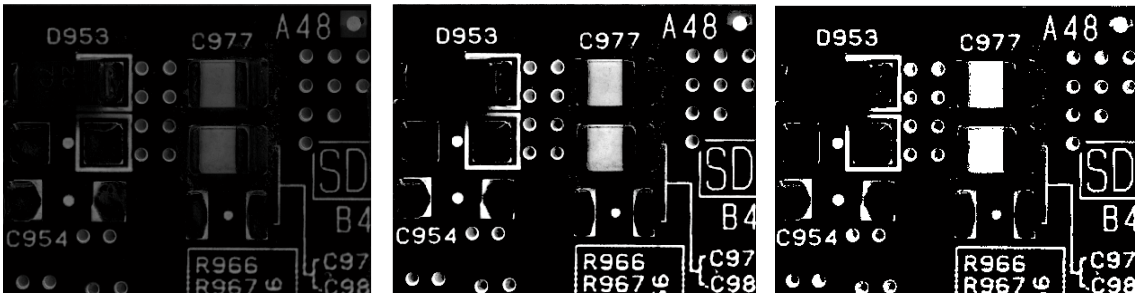

(a) Hue channel (HSV) (b) gamma adjustment (c) binary image

Figure 2.1.3 Image processing sequence used to extract the location and orientation of capacitors and the locations of fiducials on each test board

The process starts by transforming the images of the board from RGB to the hue, saturation, value (HSV) color space and then extracting the hue channel, containing the color information. A gamma correction on the hue channel is then performed to increase contrast between the desired features and the background. A threshold is then applied to generate the binary image shown in Figure 2.1.3c. The threshold value will vary according to the color of the fiducials, devices, or other desired features. The binary

image then goes through a blob detection algorithm from the Matlab Image Processing Toolbox. The algorithm finds the location, area, and eccentricity of each blob. The blob properties are then used to extract the desired fiducials and device locations. The coordinates of the center of the desired features are given in terms of pixels, with the origin at the top left corner of the image. The unit conversion from the image resolution in dots per inch to microns was verified by taking measurements of features with known dimensions.

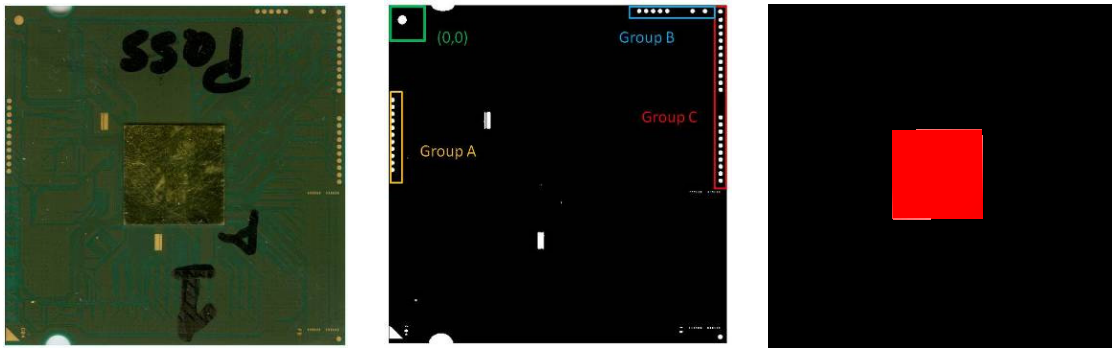

(a) high-resolution image (b) extracted fiducials (c) extracted device

Figure 2.1.4 High-resolution scanned images of substrate and flip chip device and results for measuring fiducials and device locations

2.2 Interferometer to Camera Offset Calibration

The laser ultrasonic inspection system utilizes a digital camera to locate preprogrammed features on a device-carrying board and then uses the P_{inter} vector shown in Figure 1.2.6 to calculate the translation of the X-Y stage so that those features measured in the CCD reference frame are positioned at the interferometer frame. When the system was first installed, the P_{inter} offset was measured to an estimated accuracy of ±15 µm [Howard T., 2002]. The method utilized for that initial calibration provided adequate accuracy; but, because it relied on visual observations, it was not adequate for

the fast and repeatable measurements needed for high-volume, on-line applications. To maintain the system's repeatability, a new measurement of the P_{inter} vector must be made whenever any system modifications move the interferometer or the CCD camera. The precision of this measurement is relevant, because the inspection system evaluates devices by comparing their responses, and therefore the measurements must take place at the same location on every device.

The fixture designed for calibrating P_{inter} measurements is shown in Figure 2.2.1. The fixture holds one end of a 500 µm diameter (100 µm core) optical fiber perpendicular to the surface of the X-Y positioning stage, while the other end has a connector that holds the fiber so that it can be attached to either a light source or a sensor.

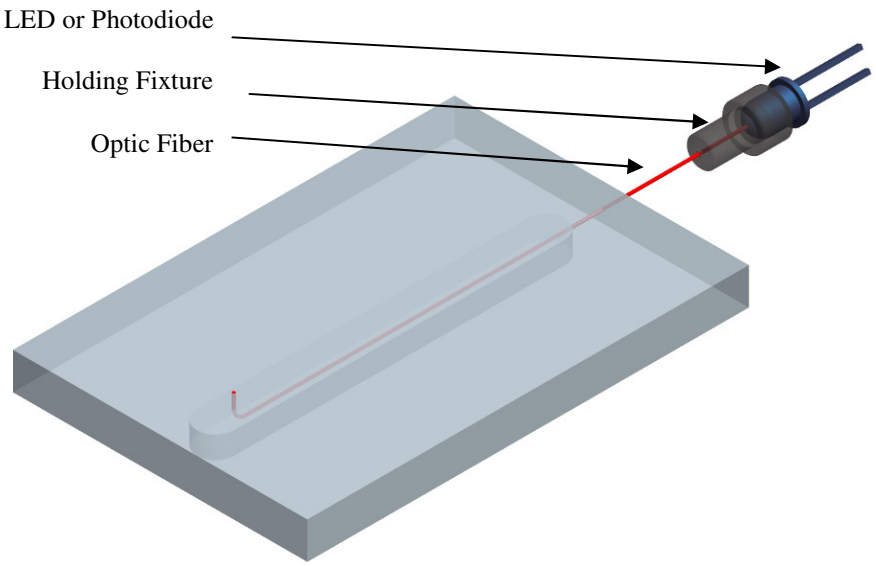

Figure 2.2.1 Calibration fixture

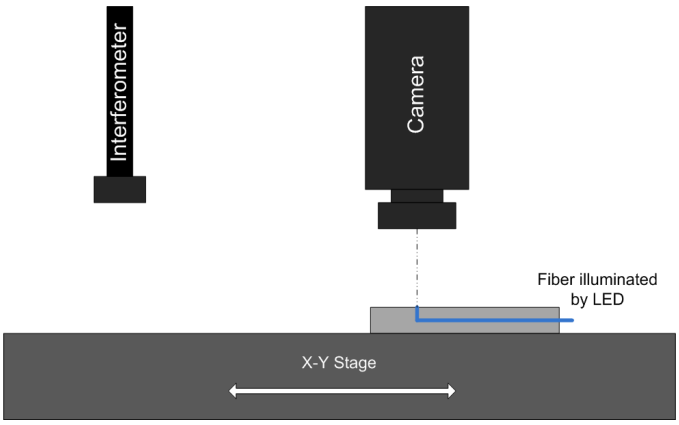

(a) fixture located at the center of the camera's field of view

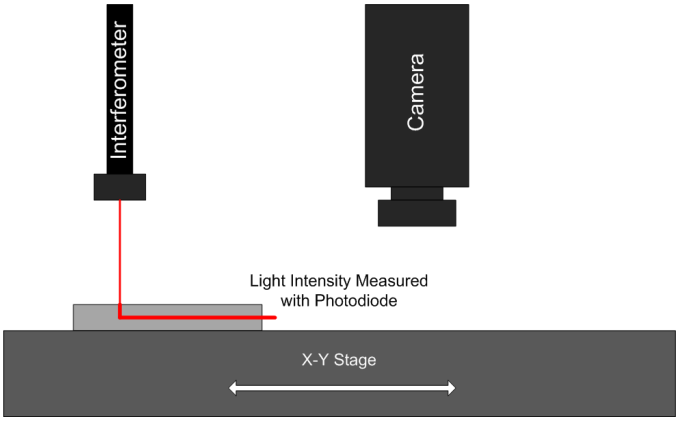

(b) fixture is moved under interferometer to locate the center of the fiber

Figure 2.2.2 Calibration procedure using proposed fixture and method

The first step in the calibration is to place the fixture in the X-Y positioning stage, where it is held in place by the vacuum that holds the substrate during testing. The optical fiber is then lit using an LED placed at the free end, and the X-Y positioning stage is moved until the (perpendicular) lit fiber end is within the camera's field of view. The camera software is then used to measure the location of the fiber and to move the X-Y positioning stage until the fiber coincides with the center of the CCD frame of reference (camera center) as shown in Figure 2.2.2a. Once the stage location is recorded, the LED

is replaced with a photodiode, and the stage is moved towards the interferometer until the laser is hitting the perpendicular end of the optical fiber, as shown in Figure 2.2.2b. Finally, the stage is independently swept in the ±X and ±Y directions while measuring the amount of light transmitted through the fiber. These perpendicular sweeps generate the two intensity profiles shown in Figure 2.2.3.

The interferometer utilized in this inspection system has a focused spot size of approximately 3 μm [Yang, J., 2008]. Therefore, when the laser spot is on the fiber core, the light is transmitted to the photodiode, but as the laser moves towards the cladding, the light is attenuated. This results in the hat-shaped profile with a diameter approximately equal to the diameter of the fiber core. The measured intensity profile is used to determine the absolute X-Y stage position where the interferometer's laser spot is at the center of the optical fiber. With the X-Y stage coordinates for where the fiber is at the camera's center and where the interferometer is at the fiber's center, the distance between the camera and interferometer can be expresed in terms of the X-Y stage steps.

The first proof of concept calibration revealed that the center of the interferometer spot was located at an absolute position (-263320 steps, -382880 steps) on the X-Y positioning stage. The center position in each orthogonal direction was determined by finding the centroid of each profile independently. This revealed that, as expected, neither orthogonal sweep was performed about the measured center of the laser spot. To verify the shape of the profile, a second calibration performed sweeps with 400 steps between sweeps and at a measurement interval of 100 steps. The measured shape of the complete profile is shown in Figure 2.2.4. The individual center for each sweep was calculated to verify that, if the sweep was done far away from the center of the interferometer spot, the

outcome of the calibration would remain the same. Table 2.2.1 shows the five sweeps in each direction with the results for the center of the interferometer. These results show that the standard deviation for the calculated center is below the 7 µm resolution of the X-Y positioning stage.

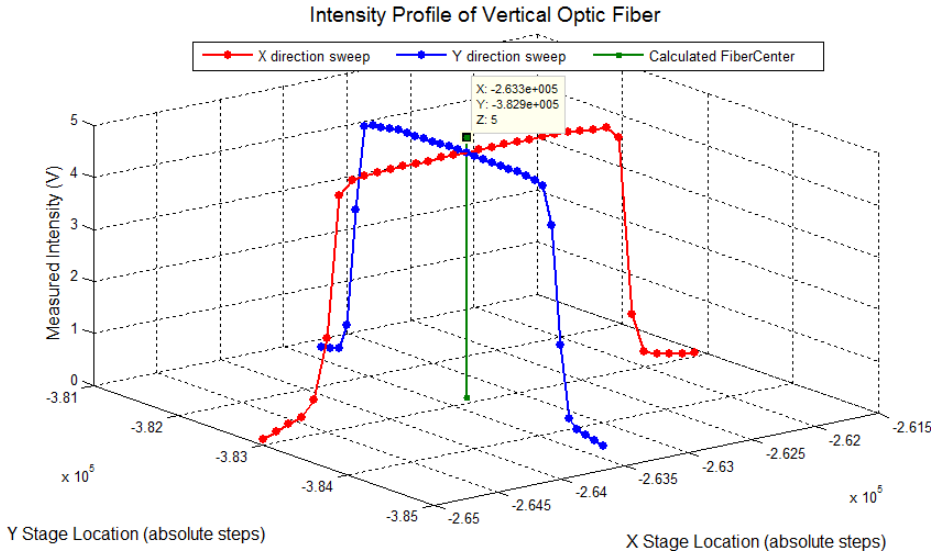

Figure 2.2.3 Measured light intensity profiles in X and Y directions.

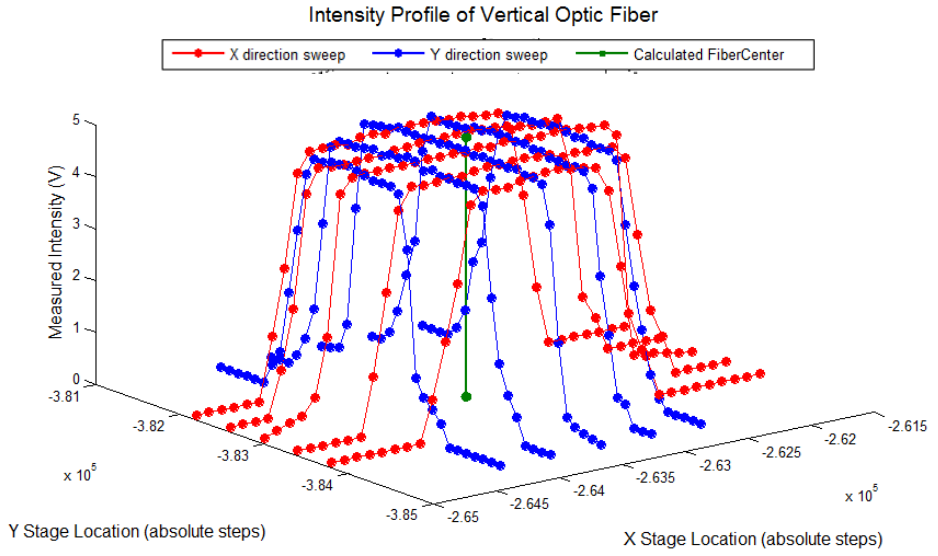

Figure 2.2.4 Measured light intensity profiles for five sweeps on each axis

Table 2.2.1 Center location from five different sweeps

	Sweep 1	Sweep 2	Sweep 3	Sweep 4	Sweep 5	**Average (step)**	**STD (step)**	**STD (um)**
X direction	-263320	-263360	-263350	-263290	-263360	-263336	30.50	2.38
Y direction	-382880	-382910	-382860	-382910	-382900	-382892	21.68	1.69

Another method to measure the center of the profile was performed by fitting a surface to the sweep data, as shown in Figure 2.2.5. The center, calculated using the volume of the fitted surface, showed that the center of the interferometer lies at (-263320 steps, -38290 steps). In conclusion, these three methods of finding the fiber center from orthogonal sweeps demonstrated that a simple two-axis sweep of the light intensity across the optical fiber provides a robust measurement of the center of the interferometer spot independently of where along the diameter of the fiber these sweeps are made; they also demonstrate that multiple sweeps are not required.

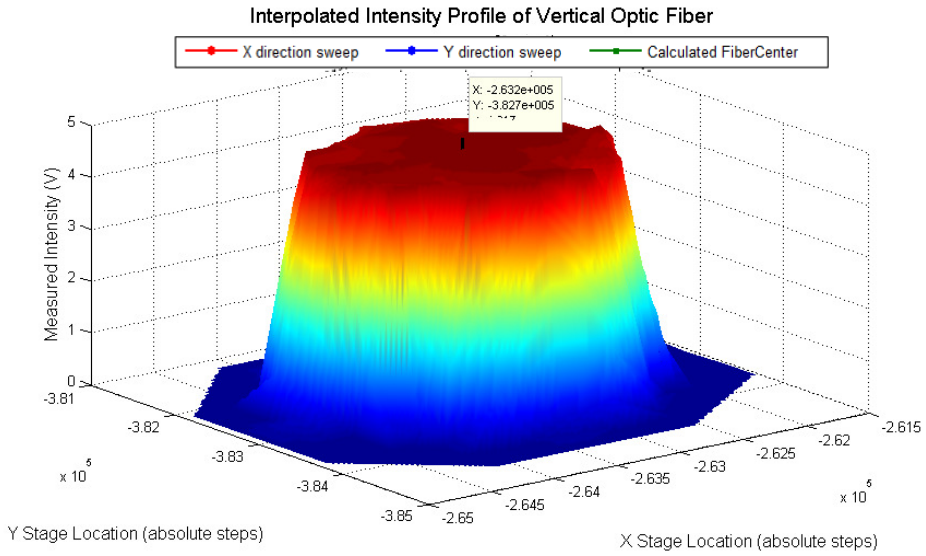

Figure 2.2.5 Surface fitted to the light intensity profile measurements

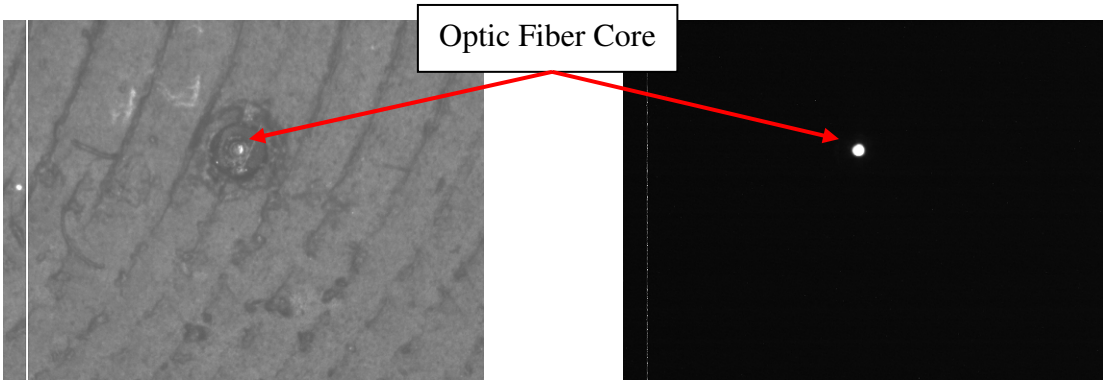

(a) fixture surface (b) lit optic fiber

Figure 2.2.6 Calibration fixture and optical fiber end as seen from CCD camera

Once the center of the interferometer is known, the fixture is moved under the camera, and the fiber is illuminated with an LED. The X-Y stage is then moved so that the optical fiber is at the center of the camera's frame of reference by using the blob-finding algorithms provided by the camera software [Turner, H., 2002]. The surface of the fixture with the exposed vertical optical fiber end and the result from the image processing are shown in Figure 2.2.6. The absolute location of the X-Y stage when the center of the optical fiber coincided with the center of the camera's field of view was (3585 steps, -339500 steps); therefore, the offset needed for the coordinate transformations was (-266923 steps, -43392 steps).

The precision of the calibration process and of the fixture were studied by performing repeatability measurements on a flip chip device with 48 solder bumps along the perimeter. The same device was inspected twice, and the two measurements were correlated to establish that the noise level for this device had a mean Modified Correlation Coefficient (MCC) value of 0.01504. The location of the interferometer was then altered and the P_{inter} determination performed. The same device was again inspected

and correlated to the initial inspection before the interferometer was moved, and the mean MCC value was 0.01628. The interferometer was moved a third time, and P_{inter} determined once again. Inspecting the same device and correlating with the original measurement yielded a mean MCC value of 0.01562. The results of these correlations are shown in Figure 2.2.7.This study demonstrated that this calibration method allows the comparison of data captured before and after any system changes that affect the distance between the interferometer laser spot and the center of the CCD camera.

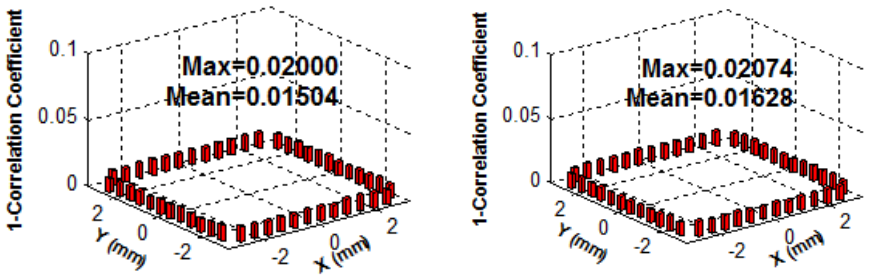

(a) repeatability with no changes (b) repeatability after one system change

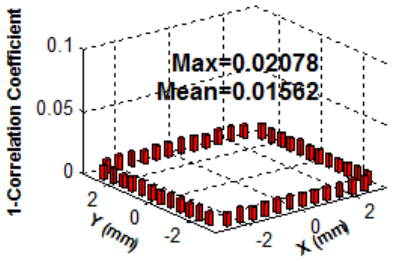

(c) repeatability after two system changes

Figure 2.2.7 Repeatability of P_{inter} offset measurement using flip chip device and MCC

2.3 Energy Density Characterization and Determination of Ablation Threshold

In the laser ultrasonic inspection system, a pulsed Nd:YAG laser causes the device under inspection to vibrate by generating ultrasound in the thermoelastic regime,

where the energy absorbed by the surface material is relatively low compared to the ablative regime of laser ultrasound generation. Dixon reports that the transition from the thermoelastic regime to the ablative regime occurs at an energy density of 0.20 to 0.24 J/cm^2 in <100> single-crystal silicon [Dixon, S., 1996]. In current electronic packages, a thin passivation layer (usually Si_3N_4, SiO_2, polyimide, or phosphosilicate glass) of approximately 1 μm, or other encapsulation method, protects the underlying silicon. The presence of these coatings alters the reflectivity and thermal properties of the package surface, therefore changing the energy density threshold for the onset of ablation. In laser ultrasonic inspection of microelectronic devices, the ablative regime is avoided to prevent damage to the device or the package. Jian places the damage to MOS-type devices in two categories: soft damage refers to the laser energy causing changes in the electron-hole balance of the different semiconductor impurity materials, while hard damage refers to direct damage to the material or structure of the device. The threshold for hard damage is referred to as the laser energy density under which plasma is generated, with the size of the damaged area increasing with the laser energy level [Jian, L, 1998].

Determining the damage threshold for this particular device was done by measuring the visible surface damage to the coating. The damage is also expressed as a function of the delivered energy density of the pulsed laser. The device utilized was a high-density flip chip package with a gold surface coating. The experimental ablation threshold is presented as a function of the laser energy density, as reported by Dixon [Dixon, S., 1996].

The first step in determining the delivered energy density was to characterize the size of the focused laser spot as a function of the manual stage position. The laser

focusing objective shown in Figure 1.2.3 is mounted on a manual stage that has 25 mm of total travel and is positioned at a 45° angle to the X-Y stage surface, creating a focused elliptical spot on the surface of the package, as shown in Figure 2.3.1. The laser spot area was measured for the 15 mm, 17.5 mm, 20 mm, 22.5 mm, and 25 mm positions on the manual focusing stage. The results, summarized in Figure 2.3.2, show the attainable spot sizes within the travel range of the focusing stage. The area of the laser spot was measured by first taking a high-resolution image (7.4 μm pixels) of the spot on a dark surface. Then, using Matlab, the grayscale image was changed to black and white. Counting the number of white pixels and multiplying by the pixel area yielded a measure of the area of the spot (Appendix A.2).

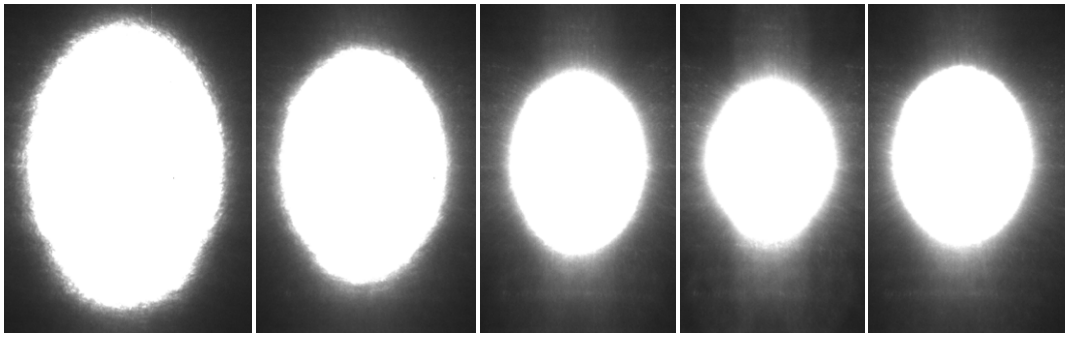

(a) 15.0 mm (b) 17.5 mm (c) 20.0 mm (d) 22.5 mm (e) 25.0 mm

Figure 2.3.1 Laser spot sizes for various positions of the manual focusing stage

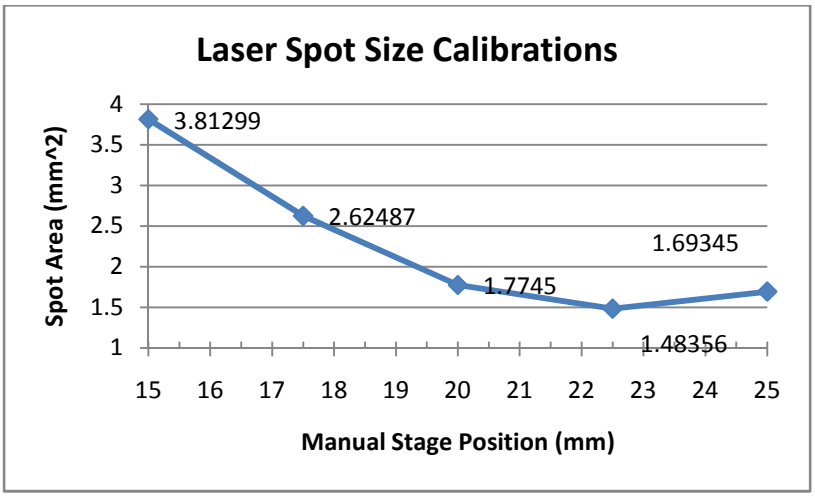

Figure 2.3.2 Laser spot size vs. focusing objective position

The second step was to measure the surface damage caused by the pulsed excitation laser. The laser output was controlled by an optical attenuator, and the power was measured with a calorimeter tuned to the laser's 1064 nm wavelength. Phase I of the characterization was performed with an offset of 22.5 mm, equivalent to an area of 1.48 mm^2, and the laser power was adjusted from 38.0 mW to 61.2 mW. During phase II, both the focusing objective standoff and the laser power were varied to gradually increase the energy density. Surface ablation was detected and measured using the same optical system used in the spot size calibrations. Images of the surface were captured at regular time intervals while the laser was impinging on the device. Figure 2.3.3 shows the progression of the measurement for the highest achievable energy density (0.206 J/cm^2). An image of the surface was taken prior to ablation (a) and five minutes later (c). These two images were then subtracted to find where the surface changed due to ablation. Some of the small visible speckles far from the laser spot area resulted from the ablated material landing on the surface of the die. Figure 2.3.4 shows the ablations observed at different laser energy densities.

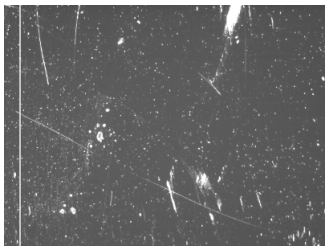

a) beginning

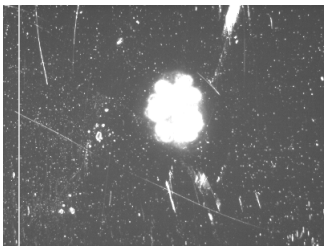

b) focused laser spot

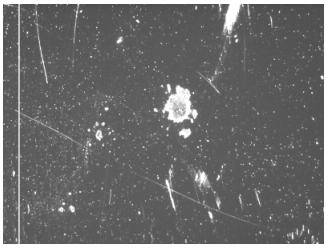

c) surface damage at the end of the interval

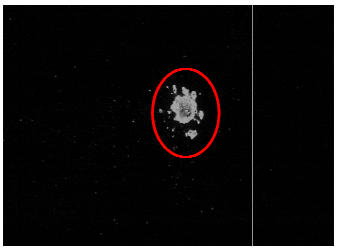

d) difference between final and initial

Figure 2.3.3 Surface damage progression for 0.206 J/cm^2 energy density

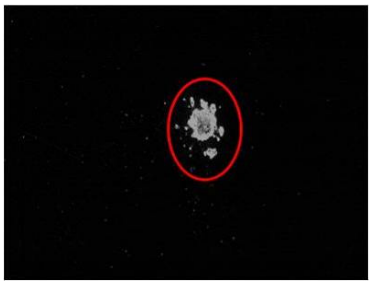

a) 0.206 J/cm^2

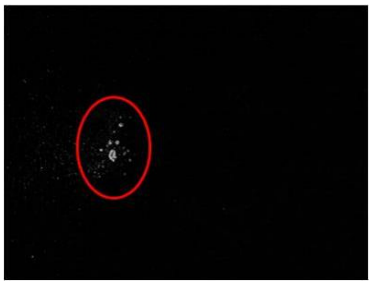

b) 0.150 J/cm^2

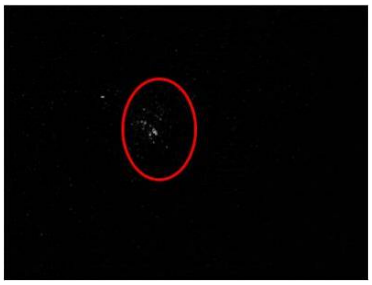

c) 0.133 J/cm^2

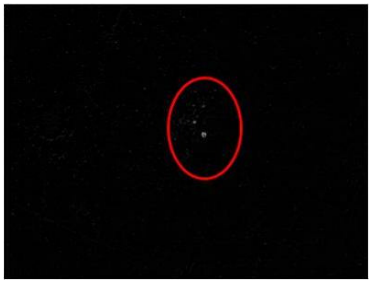

d) 0.128 J/cm^2

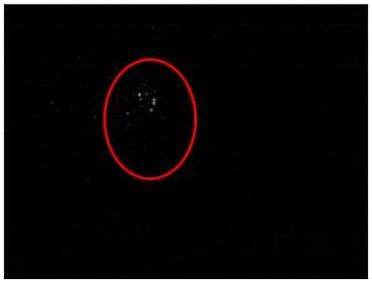

e) 0.110 J/cm^2

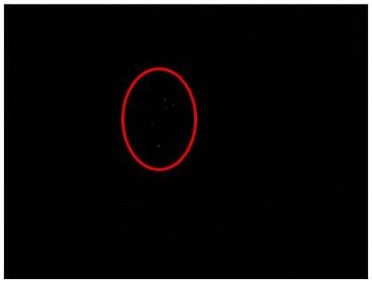

f) 0.100 J/cm^2

Figure 2.3.4 Ablation observed at different energy density levels

The data summarized in Table 2.3.1 shows that when the laser power reached 61.2 mW at the minimum attainable spot area of 1.484 mm^2, the energy density achieved was 0.206 J/cm^2. At this power level, damage was observed on 10 percent of the laser spot area. The ablated area, calculated from the images taken during phases I and II of the experiment, is shown as a function of the laser spot area in Figure 2.3.5. A significant increase in the ablated area is observed at energy densities greater than 0.140 J/cm^2. This observed increase in damage is below the ablation transition point found by Dixon (0.20 to 0.24 J/cm^2). It is also important to note that some minimal damage, on the order of a few 7.4 by 7.4 µm pixels, was observed at power levels as low as 0.100 J/cm^2.

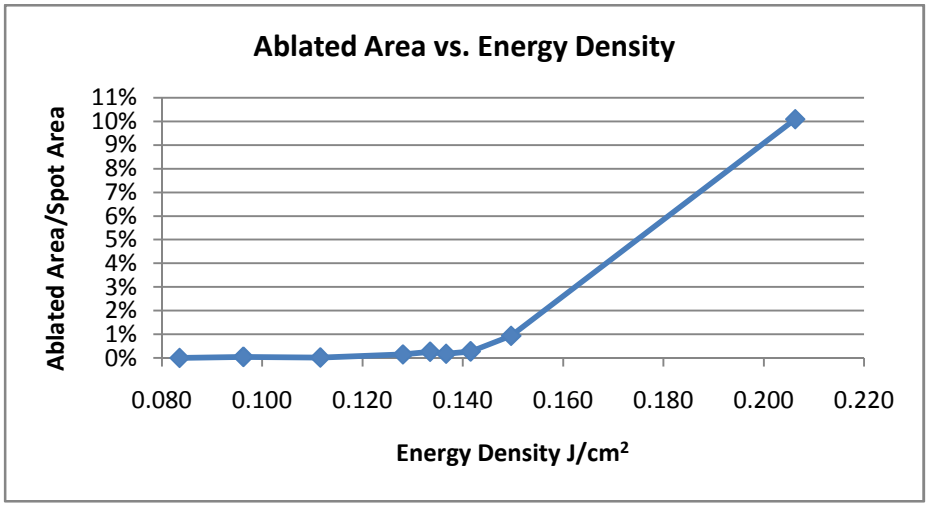

Figure 2.3.5 Ablated area as a function of energy density

Table 2.3.1 Measured energy density and ablated area

Energy Density J/cm^2	Power mW	Area cm^2	Measured Ablation		
			Pixels	cm^2	%
0.084	63.7	0.038	0	0.E+00	0.00%
0.096	73.4	0.038	32	2.E-05	0.05%
0.112	39.6	0.018	5	3.E-06	0.02%
0.128	38	0.015	40	2.E-05	0.15%
0.133	39.6	0.015	71	4.E-05	0.26%
0.137	48.5	0.018	57	3.E-05	0.18%
0.142	42	0.015	75	4.E-05	0.28%
0.150	44.4	0.015	253	1.E-04	0.93%
0.206	61.2	0.015	2734	1.E-03	10.09%

The experimentally determined ablation threshold of 0.140 J/cm^2 was lower than the theoretical threshold due to the surface reflectivity and thermal properties of the surface coating on the device. The irregular device surface, shown in Figure 2.3.6, had multiple scratches and pits in the coating that could act as sources for ablation at low power levels. These surface imperfections have lower reflectivity and increased energy absorption, and the local temperature rise caused some of the material to be ablated at lower energy densities than the theoretical limit for the onset of ablation [Scruby, C.B., 1990].

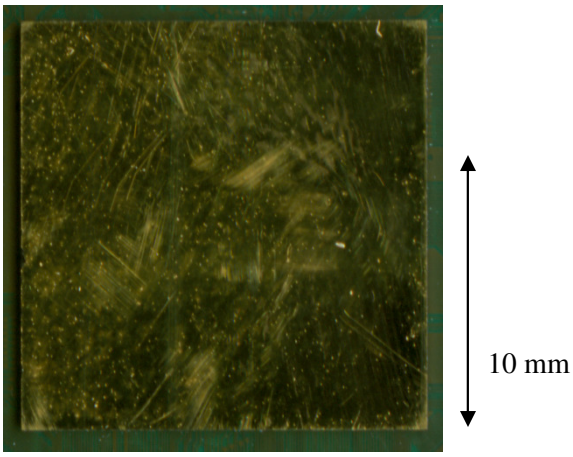

Figure 2.3.6 Device surface defects

2.4 Conclusions

Repeatability measurements performed on a flip chip device showed that the proposed method and fixture for determining the P_{inter} vector provided adequate precision for system calibration. This method will allow data taken before and after any system changes to be comparable using the current signal processing methods which rely on correlating vibration response.

The surface ablation on a flip chip device was tracked for the achievable laser energy density range of the system to provide an experimental measure of the surface damage threshold. This investigation also revealed that surface irregularities, such as scratches or cracks, can significantly increase the laser energy absorption and induce damage at lower power levels. The procedure presented can be applied prior to testing devices with new surface finishes in order to verify that no surface damage will be caused by the laser excitation.

Chapter 3: Local Laser Ultrasound Excitation Method

In the center excitation/measurement scheme, the laser ultrasound generation always takes place at the center of, or other fixed location on, the device surface, while the interferometer measures the vibration response at different surface locations. In very stiff packages, such as BGAs and large, high-density FCPs, the energy supplied by the pulsed laser may be too far from the measurement location to cause sufficiently strong vibrations at the location. The attenuation of mechanical waves in larger devices causes the measured vibration waveform to vary from one inspection location to the next. Also, as the signal becomes weaker, noise can disguise the changes in vibration caused by defects. These conditions can cause problems during time-domain signal processing. The local excitation/measurement scheme presented in this chapter aims to resolve these problems by always placing the laser ultrasound excitation source at the inspection location, coupling the motion of the laser excitation location to the measurement location.

This method of excitation has three distinct advantages: first, regardless of the measurement location, the delivered power level and signal-to-noise ratio will be the same; second, because the excitation source is much closer to the measurement location, very low power levels can be used, greatly reducing the possibility of damaging the device, especially for such over-molded packages as BGAs or coated flip chips, which have much lower maximum allowable power levels than silicon; and third, this system is simpler to implement than the current method and also reduces the level of automation or operator input required to set each device up for inspection. The hardware implementation of this system can be rearranged to eliminate the need for a fragile and expensive optical fiber delivery system. With the application of this

excitation/measurement scheme, laser ultrasonic inspection will be more effective in detecting defects, such as cracked and missing solder bumps, in larger devices with more interconnects.

3.1 Hardware Implementation

The current system hardware, shown in Figure 3.1.1, places the laser focusing objective on a manual X-Y positioning stage with linear encoders. The manual stage is mounted on top of a planar positioning stage, which moves the devices from one inspection location to the next. Since the motion of the focusing objective is coupled to the motion of the device, the laser spot stays at a fixed location on the device's surface throughout the inspection.

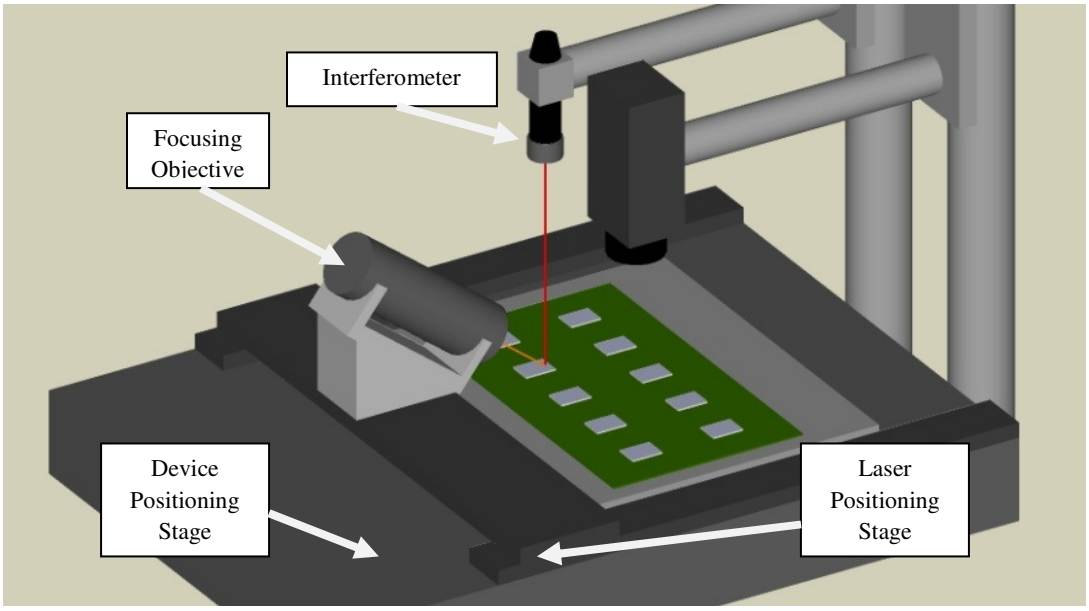

Figure 3.1.1 Current hardware implementation for excitation-measuring scheme

The local excitation method changes this scheme, requiring the laser spot to stay at a fixed distance from the interferometer; in this case, they will coincide. Coupling the

motion of the interferometer and the laser spot is achieved by mounting the focusing objective on a cantilevered beam attached to the base of the system, as shown in Figure 3.1.2. The beam is supported by a column mounted on a linear stage. This stage is used to control the distance between the interferometer location and the laser spot. To preserve spot size calibrations, the new mounting position places the focusing objective at the same height as the configuration for center excitation.

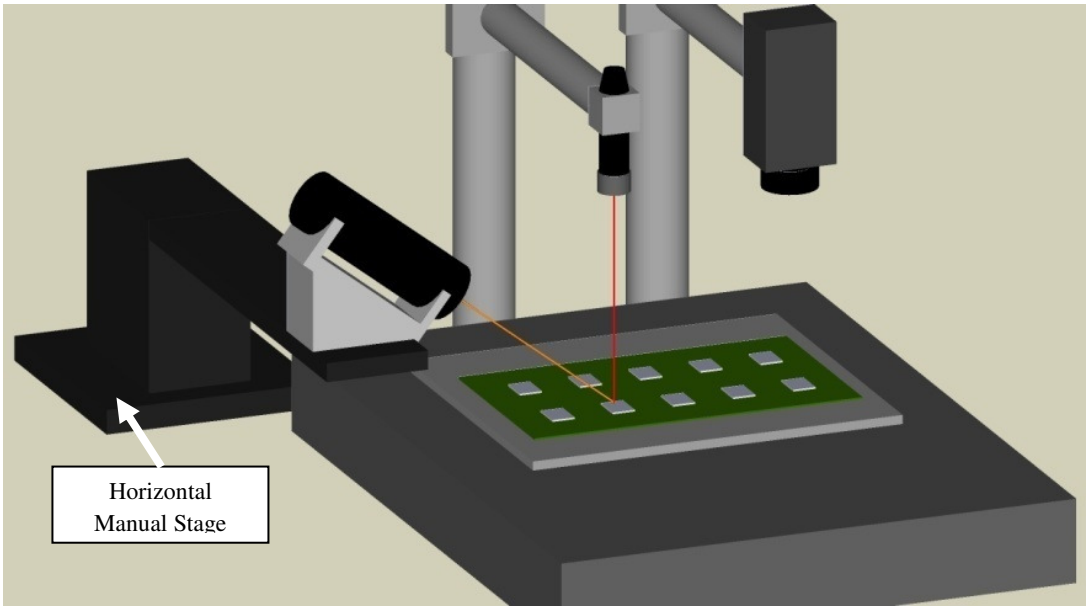

Figure 3.1.2 System hardware implemented for proposed excitation-measuring scheme

The local excitation/measurement concept was validated using a scheme that placed the laser on the same location on the package surface as the interferometer. Since the focusing objective is mounted at a 45º angle from the device surface, the intersection of the interferometer and excitation laser beams depends on the device height, as shown in Figure 3.1.3. To compensate for devices of different height, the horizontal manual stage position was characterized for a variety of device heights. The manual stage position corresponding to the point of intersection at different device heights was found

by moving the laser spot on orthogonal sweeps while measuring the average signal intensity. The interferometer and excitation lasers coincide at the location with the maximum signal intensity. The stage position was found for zero height (surface of the vacuum fixture) and up to a height of 2.21 mm, as shown in Table 3.1.1. A linear regression for the stage position as a function of device height is shown in Figure 3.1.4. The slope of 1.04 is indicative of the 45° angle of the focusing objective. This calibration can be used in the future to arrange the hardware for devices of different heights.

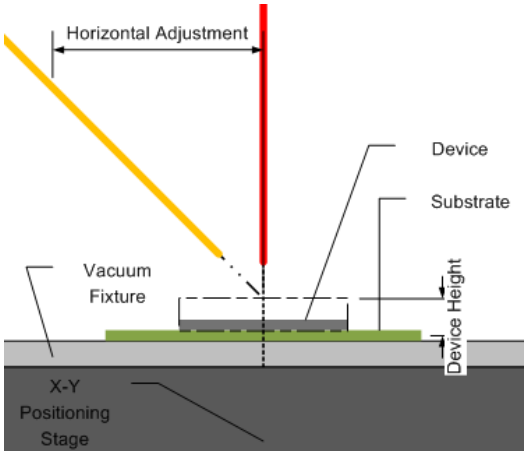

Figure 3.1.3 Intersection of interferometer and excitation laser beams

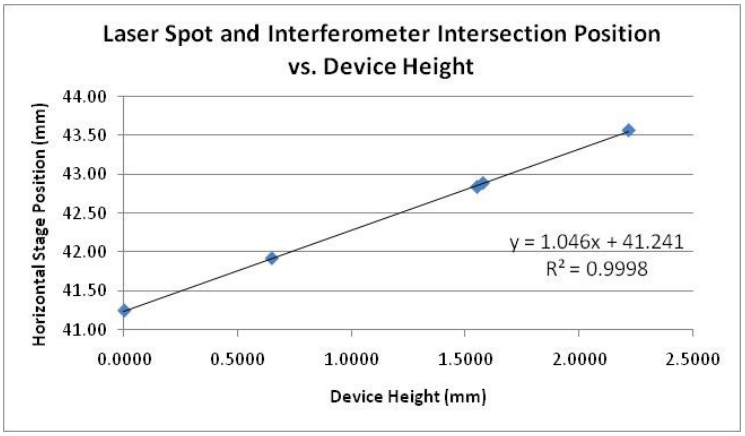

Figure 3.1.4 Regression for stage position as a function of device height

Table 3.1.1 Intersection point calibration data

Test Surface	Stage Position (mm)	Height (mm)	Δ Stage	Δ Height	Δ Stage/Δ Height
Vacuum Fixture	41.25	0.000	N/A	N/A	N/A
FC-48 Flip Chip	43.57	2.214	2.33	2.2149	1.05
Pb-18 Flip Chip	42.84	1.549	-0.73	-0.6655	1.10
Ceramic Substrate	41.92	0.647	-0.92	-0.9017	1.02
Organic Substrate	42.89	1.574	0.97	0.9271	1.05

3.2 Validation of Local Excitation

The test vehicle chosen to validate the proposed excitation and measurement scheme was a flip chip device with 48 solder bumps located along the perimeter and without underfill. The die, 6.35 mm by 6.36 mm by 0.6mm, had a solder bump diameter of 190 µm and a pitch of 457 µm. These devices were assembled with either corner or center defects, as shown in Figure 3.2.1. Removing the copper pad from the substrate caused the solder bump to not adhere, therefore simulating a through crack or open bump. Three devices were tested for each defect type, with one to three defective connections.

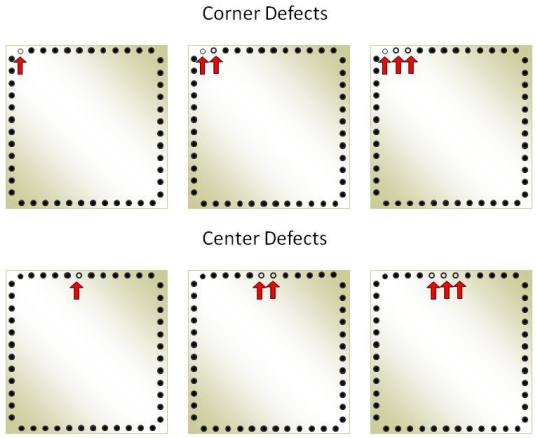

Figure 3.2.1 Corner and center defect locations for FC48 flip chip device

The devices were inspected with a 48-point inspection pattern, by taking measurements above each solder bump, using a power level of 34 mW and focusing on a

3 mm^2 spot. Measurement repeatability was assessed by measuring the same device multiple times and correlating measurements using the Modified Correlation Coefficient (MCC) method shown in Table 3.2.1. These measurements also served the purpose of establishing the levels of the MCC values, which change depending on the general shape of the waveform and the mean value of the time-domain waveform.

Table 3.2.1 Measurement repeatability for all inspected devices using MCC

Device Type	Sum	Max	Mean
1 Center	0.01823	0.00026	0.00019
2 Center	0.03053	0.00289	0.00009
3 Center	0.02099	0.00110	0.00006
1 Corner	0.01634	0.00363	0.00029
2 Corner	0.03858	0.00254	0.00009
3 Corner	0.01238	0.00080	0.00034
No Defects 1	0.04588	0.00041	0.00001
No Defects 2	0.04546	0.00268	0.00022
No Defects 3	0.04870	0.00256	0.00023
No Defects 4	0.01549	0.00342	0.00039
Average	**0.02926**	**0.00203**	**0.00019**

The MCC method results in Figure 3.2.2 show that the local excitation method was able to identify the cracked solder bump defects in the corners and center of the FCPs. Figure 3.2.3 uses the sum of all of the MCC values as a metric to show the trend of increasing change in vibration response from non-defective to three open bumps defects.

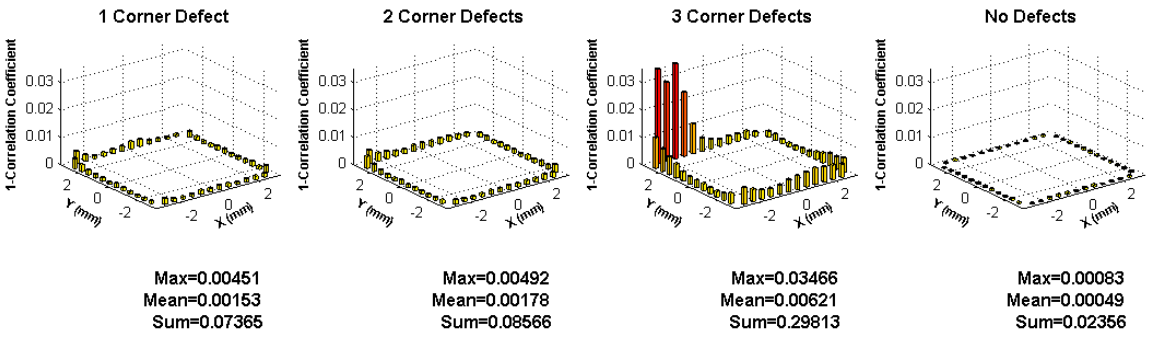

(a) corner defects

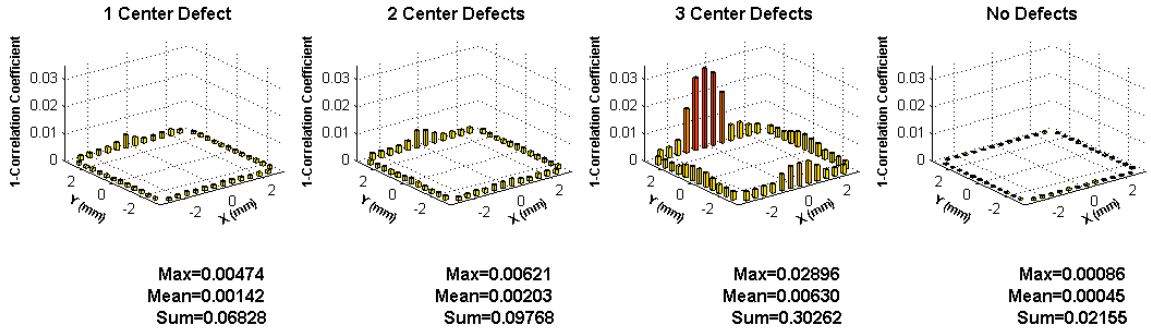

(b) center defects

Figure 3.2.2 Defect detection using local excitation and MCC methods

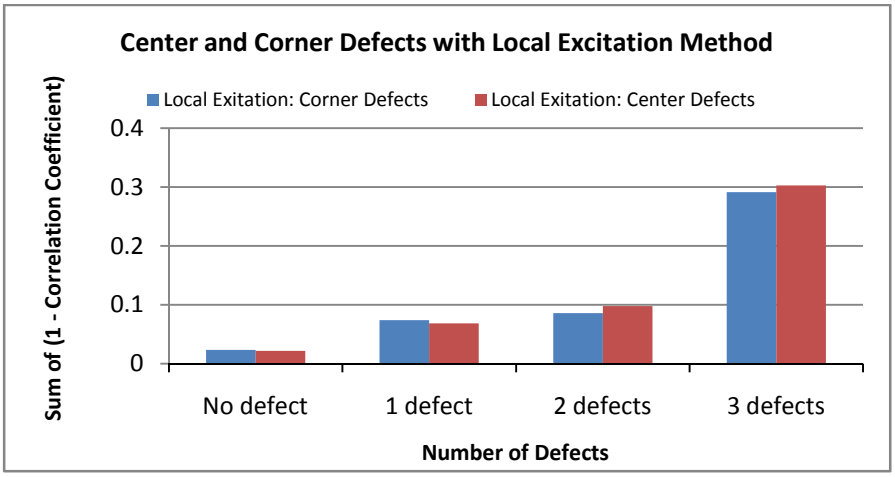

Figure 3.2.3 Correlation Coefficient Method values for 1 through 3 solder bump defects in center and corner configurations

The vibration response of the device was inherently different depending on the location of the laser ultrasonic excitation. Figure 3.2.4 shows the difference in the

vibration response at a corner of the device (inspection point 36). From these waveforms, several observations can be made. First, the signal was much stronger with local excitation, for the same laser energy density. This is very important in stiffer packages, where plastic molding or other encapsulation methods attenuate the ultrasonic waves. The larger signal amplitude also diminished the effect of electrical noise from the measurement system. Second, in local excitation, there was a large spike from 0 to 5 µs. This spike is due to the bulk upwards motion of the thermoelastic expansion of the device surface; it is captured as a spike instead of a DC offset because the interferometer controller filters out the low frequency components. The bulk upward motion at the excitation location was also present during center excitation, but it occurred far from the measurement location. Last, the signals at the corner inspection points for both methods showed changes in the vibration response with a progressively increasing number of defects.

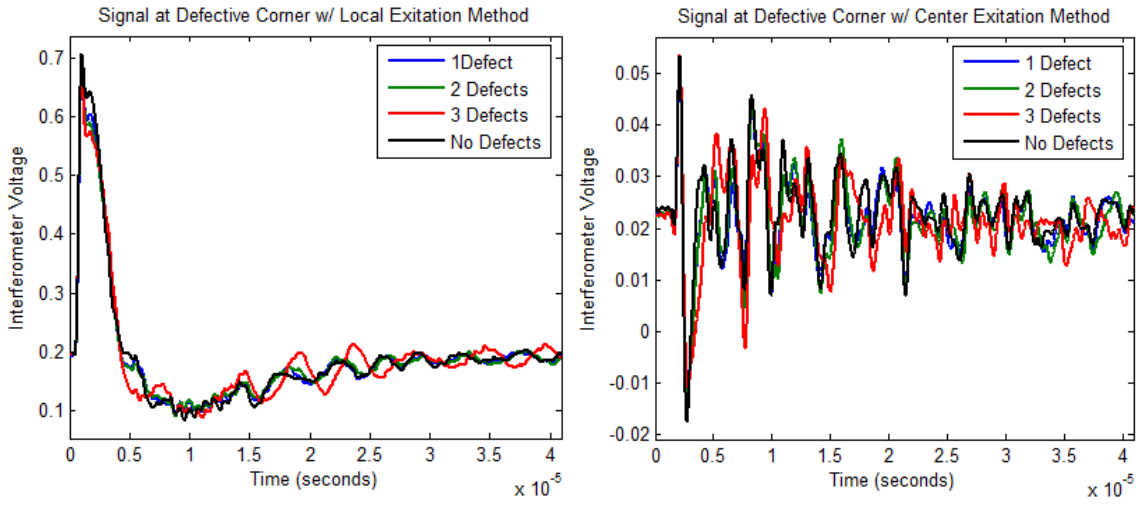

(a) local excitation (b) center excitation

Figure 3.2.4 Difference in vibration response due to change in excitation location

Figure 3.2.5 shows the periodogram for both excitation methods. It is immediately noticeable that, as expected from the time-domain signals, these methods produce very different frequency responses. The local excitation method was not able to achieve the higher frequency modes generated by center excitation. Yang, using the same test vehicle, found that some vibration modes are more sensitive to the defects. He reported that the mode at approximately 100 kHz was the least sensitive and the modes at approximately 230 kHz and 420 kHz are the most sensitive to corner and center defects [Yang, J., 2008]. This means that, with the local excitation method, only one of the sensitive modes is present; thus, this method could reduce sensitivity in terms of frequency domain analysis. The changes in mode excitation are dependent on the device structure and therefore will change from one test vehicle to another.

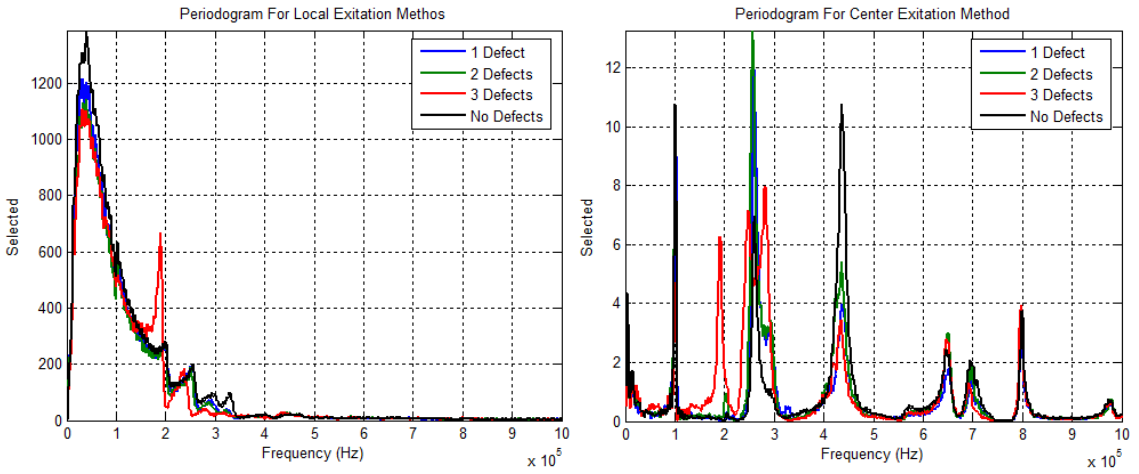

(a) local excitation (b) center excitation

Figure 3.2.5 Frequency content of vibration response

The local excitation method had the advantage of localizing the change in vibration caused by solder bump defects. Figure 3.2.6 shows the inspection results for a

device with three corner defects, using the local and center excitation methods. When center excitation was used, the changes in vibration response caused by the defects occurred at the defect locations, but also on the other corners of the device. It is still possible to identify the corner with the defects, because the largest change in vibration occurs there. In contrast, the correlation results for local excitation show that the change in vibration response due to the defects is localized to the defect location. The localization of the changes in vibration response is due to the different modes excited by each of the excitation/measurement schemes.

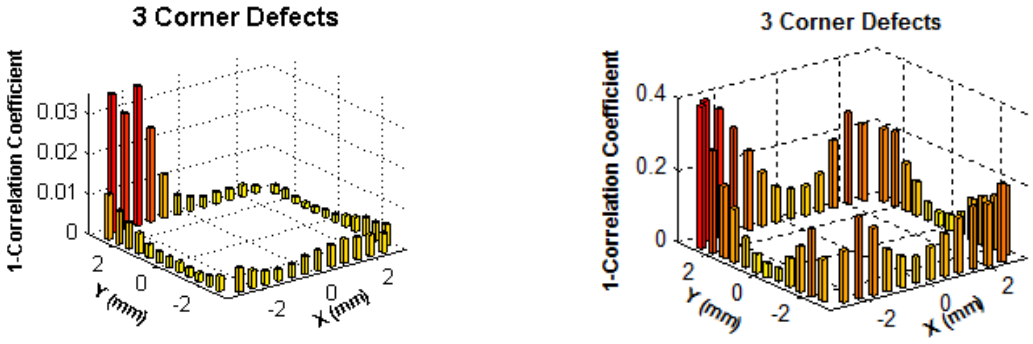

(a) local excitation (b) center excitation

Figure 3.2.6 Correlation of results from local and center excitation methods

3.3 Impact of Local Excitation Method

3.3.a System Throughput and Automation

The immediate advantage of using local excitation is that it reduces the inspection time by eliminating the manual operation of repositioning the laser focusing objective for every inspected device. This operation takes approximately 45 seconds per device and requires a user to be present. Removing this step allows the inspection process to be completely automated and to operate as a standalone system. This level of automation

greatly increases the utility of the laser ultrasonic inspection system for on-line and large-volume inspection applications. Furthermore, in future systems, local excitation can be achieved by placing the laser source directly on the focusing objective, removing the cost of the optical fiber delivery system. The hardware configuration for local excitation also allows the complete system to be placed on a fixed frame above the automated X-Y positioning stage, making it simpler and cheaper to design an inspection system that is integrated with the manufacturing equipment.

3.3.b Defect Detection in Larger Devices

In small devices with few solder bumps, the response signal captured with center excitation is very similar at all inspection points. On larger devices with more interconnects, the signal strength and shape vary significantly from one location to the next. This causes a problem when using the MCC method to identify defects. In the MCC method, the variance between the two signals is normalized by the product of their mean values. Therefore, a drastic reduction in signal strength or waveform shape causes a drastic change in the MCC values. This can be observed in the repeatability measurements for the two excitation methods. In center excitation, the repeatability — i.e., the measurement of system variation — was in the order 10^{-3}; with local excitation, it was 10^{-4}. The local excitation/measurement scheme reduces this problem by delivering the same power to all inspection locations.

3.4 Conclusion

The validation experiments showed that the local excitation/measurement scheme was able to detect the open solder bump defects in multiple locations on the flip chip test vehicle. Analysis of the difference in response between the local and center excitation

methods showed that the advantages of each of these methods depend on the structure of the device under inspection. In the flip chip test vehicle, the local excitation method localized the changes in vibration caused by defects, making it easier to identify the defective solder bumps.

The hardware implementation of the local excitation method allows it to be interchangeable with the center excitation method, making it easier to experiment with either option. The experiments also showed a potential for system simplification and for inspection time reduction, making the local excitation method more suitable for on-line and high-volume inspection applications. Further experimentation with different test vehicles is needed to make further claims about the improvements to system sensitivity and other capabilities of the local excitation/measurement scheme.

Chapter 4: Defect Detection without a Pre-established Reference Device

The laser ultrasonic and interferometric inspection technique does not detect defects directly. Instead, it identifies defects by quantifying the differences in vibration responses of the devices under inspection to the vibration response of a known-good reference device. This approach requires the validation of a non-defective reference device through other non-destructive inspection methods. The cost and time required make this approach impractical in many applications. Although this method is effective in finding defects and has been used to great success, it fails to accommodate manufacturing variations within non-defective devices by using a single device to represent the set of good devices. The approach presented in this chapter provides an alternative inspection and defect detection procedure that can be applied more directly to on-line testing and other manufacturing applications where a non-defective reference device has not been established and where large quantities of devices need to be tested while accounting for manufacturing variations.

4.1 Test Vehicles

The test vehicle utilized in the experiments discussed in this chapter was a chip capacitor. Figure 4.1.1 shows the cracks of the sort that have been observed by the manufacturer in this type of devices. These images also show that the two capacitors were not soldered the same. Differences in how devices are constrained to the board affect their structural support, which changes their vibration response under laser ultrasound excitation. Such variations in response will cause large Modified Correlation Coefficient (MCC) values when correlating the captured signals from the different

devices, even if neither is defective. Therefore, utilizing a single device as reference might lead to false positives.

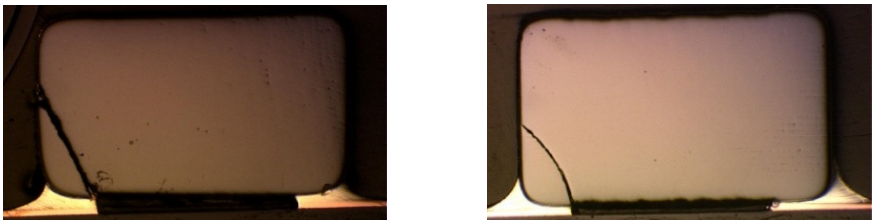

Figure 4.1.1 Cracked capacitors showing difference in solder supports and variations in assembly

The capacitors were inspected by generating ultrasound at the center of the device and taking measurements at 15 separate locations, as shown in Figure 4.1.2. This pattern was chosen to cover the capacitor surface, as well as the solder covering the terminals. For this inspection, a laser power level of 54 mW was used to provide an adequate signal-to-noise ratio while staying in the thermoelastic regime.

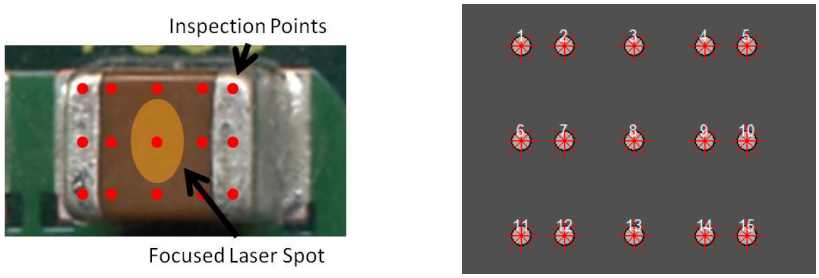

Figure 4.1.2 Inspection pattern and ultrasound generation location

The repeatability of the measurements was demonstrated by testing the same devices multiple times. Their responses at each inspection point were correlated to reveal the difference between two measurements. The quantification of the difference in vibration response by the Modified Correlation Coefficient (MCC) method shows that

the system repeatability for this particular device and inspection pattern was on the order of 10^{-2}. Table 4.1.1 shows the MCC values for the repeatability measurements.

Table 4.1.1 MCC repeatability measurement correlations for chip capacitor devices

Device Name	Sum	Max	Mean
Board A Capacitor 1	0.18360	0.03019	0.01224
Board A Capacitor 2	0.16277	0.02720	0.01085
Board B Capacitor 1	0.17290	0.02128	0.01144
Board B Capacitor 2	0.16512	0.02609	0.01205
Average	**0.1711**	**0.02619**	**0.01165**

The inspection results for the four devices showed large variations in response. Figure 4.1.3 shows the time-domain measurements at inspection point 4 for each of the capacitors. It can be observed that capacitor 2 on board A (BoardACap2A) differs significantly from the other three samples and, therefore, is most likely a defective device.

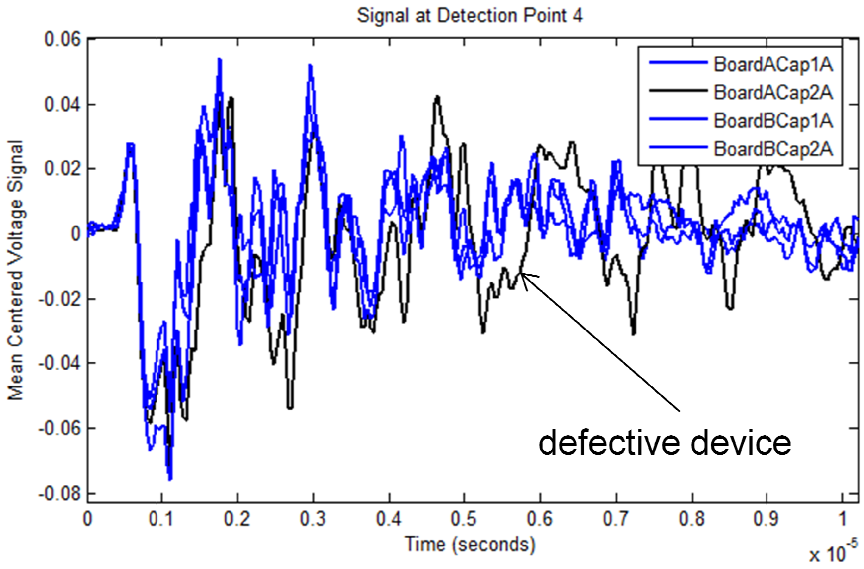

Figure 4.1.3 Vibration responses of chip capacitors at inspection location 4

The second device investigated was the daisy chain flip chip package shown in Figure 4.1.4. These devices were provided by the manufacturer in four distinct sample sets: unstressed single reflow (SR), multiple reflow (MR), rework type one (R1) and rework type two (R2). The number of devices in each set are shown in Table 4.1.2 The purpose of the single reflow (SR) devices was to serve as vibration response references for comparison with the stressed devices (MR, R1 & R2). The measurements were performed using the local laser ultrasound excitation-measurement scheme discussed in Chapter 3. The laser power level was 34 mW, focused on a 3 mm^2 spot. A sixteen-point inspection pattern, shown in Figure 4.1.4, was chosen to measure the transient displacement at two locations in each corner and in the middle of each edge.

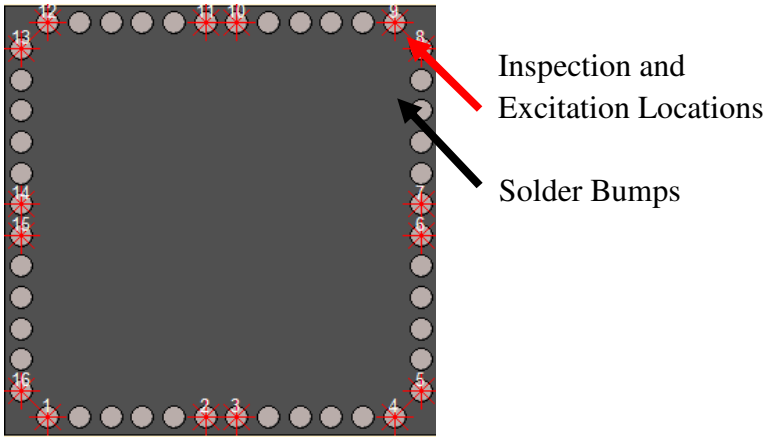

Figure 4.1.4 Sixteen point inspection and laser ultrasound excitation pattern

Table 4.1.2 Flip chip packages sample sets

Device Set		Number of Samples
Single reflow	SR	30
Multiple reflow	MR	22
Rework-type 1	R1	9
Rework-type 2	R2	18
Total		79

Table 4.1.3 shows the repeatability measurements using the MCC for ten devices and the sum, maximum, and average MCC values for the 16 inspection locations. These values were used to establish a measurement of system repeatability in terms of the MCC. Device SR-02 has a larger repeatability value because it had a chipped edge that coincided with an inspection location. The angle of the chipped edge caused high levels of noise for the interferometer; therefore, the signal quality at that location was very poor. Although the effect of a chipped edge can cause changes in vibration response, the signal quality only degrades at the chip location, as shown in Figure 4.1.5. Figure 4.1.6 shows four different measurements of the same device taken at inspection location 1 to demonstrate the repeatability of the measured response.

Table 4.1.3 MCC repeatability measurement correlations for flip chip devices

Device Name	Sum	Max	Mean
SR - 01	0.00355	0.00038	0.00022
SR - 02	0.01227	0.00883	0.00077
SR - 03	0.00697	0.00076	0.00044
SR - 04	0.00521	0.00066	0.00033
SR - 05	0.00344	0.00031	0.00021
SR - 06	0.00362	0.00056	0.00023
SR - 07	0.00339	0.00058	0.00021
SR - 08	0.00363	0.00039	0.00023
SR - 09	0.00516	0.00071	0.00032
SR - 10	0.00492	0.00050	0.00031
Average	**0.00522**	**0.00137**	**0.00033**

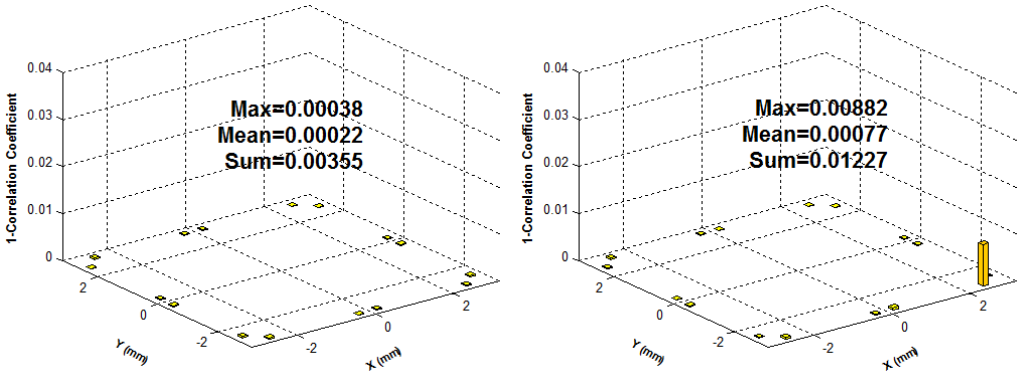

a) normal device b) device with chipped edged

Figure 4.1.5 Example of measured repeatability for a normal device and a device with a chipped edged

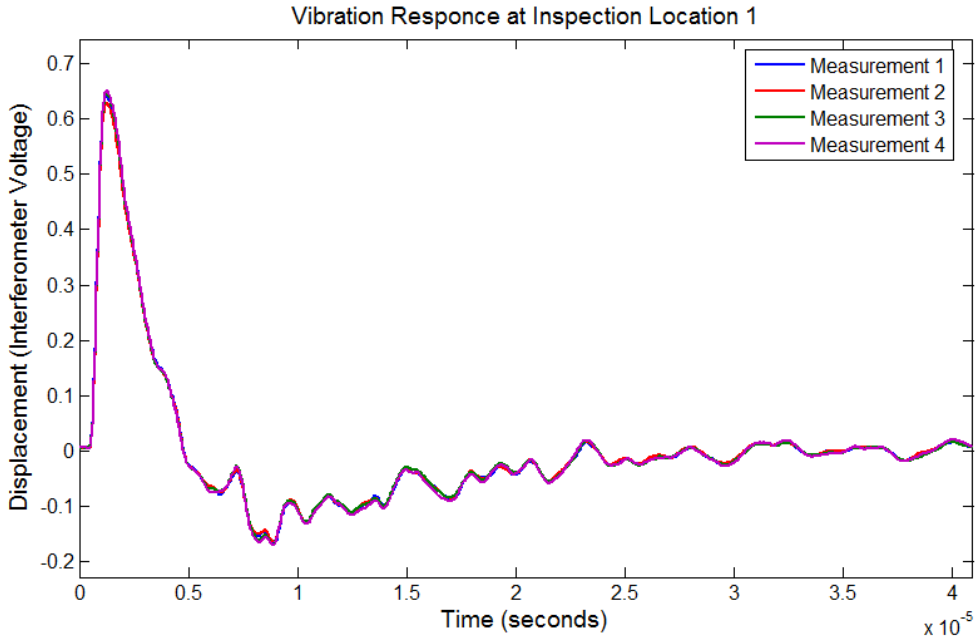

Figure 4.1.6 Response for four independent measurement at inspection location 1

4.2 Simultaneous Signal Comparison Matrix

The purpose of the Simultaneous Signal Comparison (SSC) method is to provide a means to analyze the data from device inspections without requiring a pre-established

known-good reference device. This method assumes that the signal correlation among non-defective devices is better than the signal correlation among defective devices. Therefore, the differences in vibration response caused by manufacturing variations must be smaller than the differences in vibration response caused by defects or quality degradation.

The SSC approach was used to analyze the responses of the inspected devices and to determine which responded most similarly (good devices). These devices could then be used as references for defect detection using signal processing methods, such as the Modified Correlation Coefficient method (MCC), [Zhang, L.,2006], Wavelet Analysis, [Yang, J., 2008], Local Temporal Coherence, [Yang, J., 2008], and Error Ratio, [Howard, T., 2002]. The SSC method identifies the reference devices prior to performing an inspection or statistical sampling plan.

The analysis was performed through a Matlab graphical user interface (GUI) that loads the measurement data for each inspected location and stores it in a matrix M. The discrete measurement data (of dimension n) is arranged so that every column contains the values for the time-domain signals of each device. Therefore, the data for the chip capacitor test vehicles with four devices and fifteen measurements locations is stored in fifteen matrices $M_{n\,x\,4}$. Once the data matrix is assembled, the correlation coefficient matrix R is calculated for each matrix M. The $(i,j)^{th}$ element of R is related to the covariance matrix C by Equation 4.2.1.a, where the element $R_{i,j}$ contains the correlation coefficient between the signals in the i^{th} and j^{th} column of M. The values in the correlation coefficient matrix R are normalized by the square root of the product of the expected values for each of the signals being correlated. These operations will yield a set of

matrices (one for each inspection location) containing the correlation combinations among all the devices and for each inspection location.

$$(a) \qquad Correlation\ Coefficient = R(i,j) = \frac{C(i,j)}{\sqrt{C(i,i)C(j,j)}}$$

where

$$(b) \qquad C(i,j) = Covariance\ Matrix\ (i,j) = \frac{\sum_{i=1}^{n}(X_i - \bar{X})(X_j - \bar{X})^T}{n-1} \tag{4.2.1}$$

and

$$(c) \qquad C(i,i) = variance\ of\ column\ i$$

$$column\ i = X = \begin{bmatrix} X_1 \\ \vdots \\ X_i \end{bmatrix} = \mathrm{E}[(\mathrm{X_i} - \mathrm{E[X]})^2]$$

The correlation coefficient matrix R contains all of the data needed to assess the quality of the selected devices relative to each other and to identify those suitable as references. The result of each correlation is a number *R(i,j)* between 0 and 1, which represent no-correlation and exact-correlation, respectively. To make the results of these correlations the same as the Modified Correlation Coefficient the 1-*R(i,j)* values are stored in the Simultaneous Signal Comparison (SSC) matrices. The diagonals in the SSC matrices represent the correlation of a device with itself and therefore have a 1-*R(i,i)* value of zero; it can also be observed in Equation 4.2.2 that the SSC matrix is symmetric.

$$SSC = 1 - \begin{bmatrix} \text{Device 1 vs. Device 1} & \cdots & \text{Device 1 vs. Device } j \\ \vdots & \ddots & \vdots \\ \text{Device } i \text{ vs. Device 1} & \ldots & \text{Device } i \text{ vs. Device } j \end{bmatrix} per\ inspection\ location \tag{4.2.2}$$

Once the SSC matrix was computed for each inspected location, the correlations were used to determine which devices are most similar and also to reveal the variations in vibration response among the inspected devices. The following sections will demonstrate how the SSC matrices were used to identify the most suitable reference devices for the chip capacitor and flip chips test vehicles.

4.3 Hybrid Reference Signal

Once the reference devices have been identified, it is necessary to perform one-to-one correlations between the responses of the reference devices and the responses of the devices under inspection. These correlations reveal the location and severity of defects and quality degradation. The one-to-one correlations can be performed with the MCC, Local Temporal Coherence, or Wavelet Analysis [Yang, J. 2008]. These analysis methods require the selection of an individual device to serve as a unique benchmark for the vibration response of non-defective devices. One of the shortcomings of choosing the signal from a single device as the reference is that, as shown in Figure 4.3.1, there can be large variations in response among non-defective devices. Therefore, choosing a single reference device neglects the changes in vibration response caused by manufacturing variations.

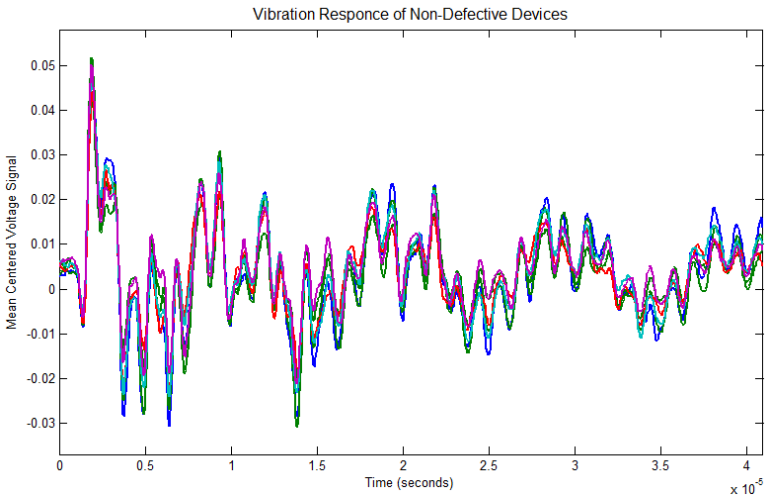

Figure 4.3.1 Variation in vibration response among non-defective devices

The effect of manufacturing variations on the chosen vibration response benchmark is addressed by using an average reference signal made by averaging the time-domain signals of non-defective devices at each of the inspection locations and creating a complete data set referred to as a hybrid reference signal. This new signal is recorded in a space-delimited file so that it can be opened with the *SuperAnalysis* Matlab GUI and compared to any inspected device.

4.4 Inspection of Cracked Chip Capacitors

The SSC method was first applied to the inspection of chip capacitors. The SSC matrices for these four capacitors were used to identify the most suitable reference devices to generate the hybrid reference signal, which was later used for inspection using the MCC method. After the inspection, the four capacitors were cross-sectioned, and a crack was found on the top right side corner of device 2 (BoardACap2A), shown in Figure 4.4.1. The cross-section results confirmed the previous observations of the vibration response at inspection point 4. The inspection and analysis of the chip

capacitors will be used to explain the SSC approach to quality inspection of microelectronic devices.

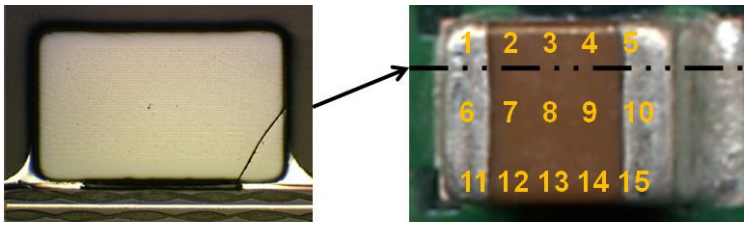

Figure 4.4.1 Cross-section results for defective capacitor and inspection locations

The SSC matrix was calculated for the chip capacitor test vehicles. The results are shown in Figure 4.4.2. Each subplot corresponds to the SSC matrix for each of the 15 inspection locations, with the numbers 1, 2, 3, and 4 representing each of the inspected devices. The plot can be interpreted by columns or by rows with the color scale defined by the maximum and minimum values from the correlations. For example, in the plot for inspection location 1, the matrix location (1,4) contains the MCC value for the correlation of devices 1 and 4 at inspection location 1. Since the MCC for device 1 versus device 4 is the same as device 4 versus device 1, the SSC matrix is symmetric. Also since the correlation of a device n versus a device n is 0, the diagonal is empty.

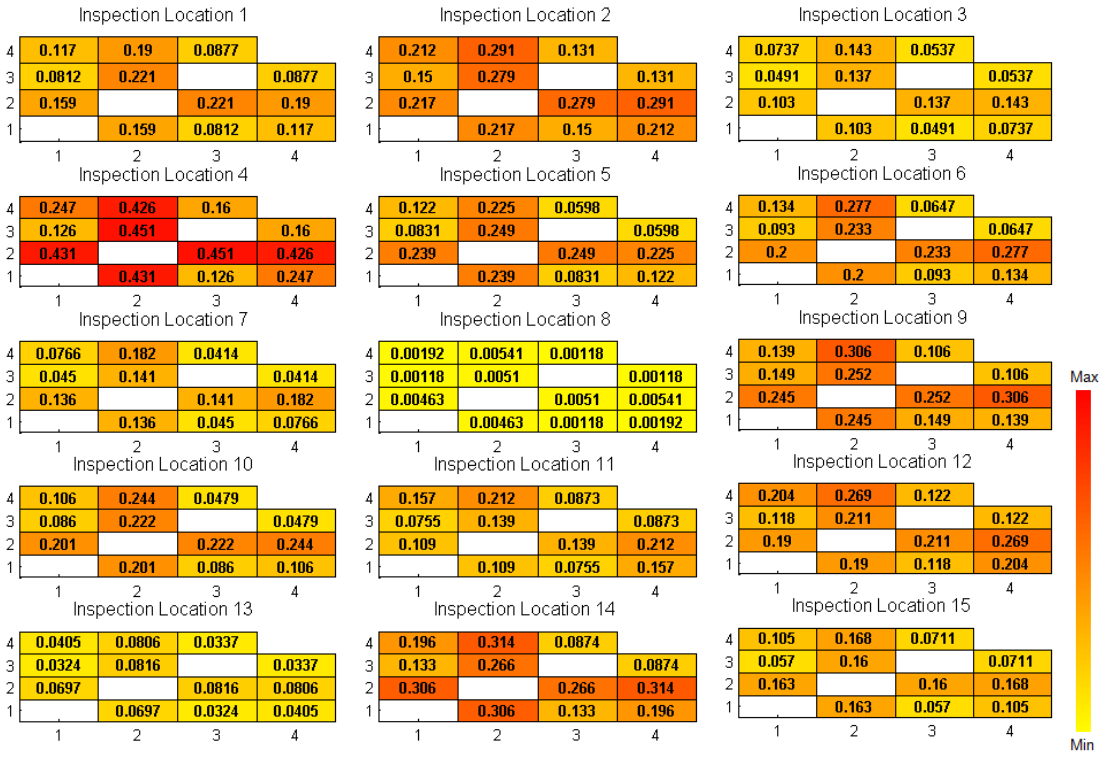

Figure 4.4.2 SSC matrices at each inspected location for the chip capacitors test vehicles

To help visualize the SSC results in Figure 4.4.2 with a single matrix, the maximum SSC matrix *A* in Figure 4.4.3 will be used. This matrix displays the highest MCC value among all the inspected locations for the correlation of device *i* and device *j*, according to Equation 4.4.1. For example, element $A_{i,j}$ contains the maximum MCC values in the i^{th} and j^{th} locations of the SSC matrices for all of the inspected locations. The maximum MCC values for the correlation among the inspected locations of device *i* and device *j* were selected as metrics because they provide the best contrast between a defective and a non-defective device. If two non-defective devices are correlated, the maximum MCC value will always be lower than the maximum from the correlation between a defective and non-defective device. In Figure 4.4.3, it can be seen that

whenever the defective capacitor (device 2) was correlated with a non-defective capacitor (devices 1, 3, and 4) high MCC values resulted, but correlating two non-defective devices with each other yielded a lower MCC value.

$$A_{i,j} = \max_{0 \le l \le L} \left(SSC_{i,j} \right)_l$$

$$where \begin{cases} L \; is \; the \; total \; number \; of \; inspected \; locations \\ (SSC)_l \; is \; the \; SSC \; matrix \; for \; inspected \; location \; l \\ i \; is \; the \; test \; device \\ j \; is \; the \; reference \; device \end{cases} \tag{4.4.1}$$

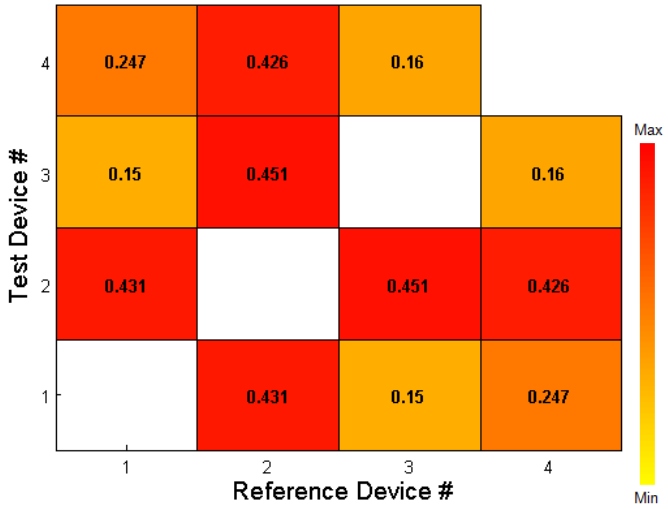

Figure 4.4.3 Matrix *A* — Maximum MCC values from the SSC matrices for each inspected location

Using the SSC matrix for each inspected location, the following steps are followed to select the non-defective reference devices to generate a hybrid reference signal:

1. From Figure 4.4.2, sum all of the MCC values resulting from correlating device *i* with device *j,* for each inspected location *l.* This gives a single value

to the correlation of device *i* with device *j,* resulting in the 4-by-4 matrix *B,* shown in Figure 4.4.4. For example, the MCC values for the correlation of device 1 and device 4 are added for each inspected location, and the results lie in $B_{1,4} = \sum_{l=1}^{15}(SSC_{1,4})_l$.

$$B_{i,j} = \sum_{l=1}^{L}(SSC_{i,j})_l \tag{4.4.2}$$

$$where \begin{cases} L\ is\ the\ total\ number\ of\ inspected\ locations \\ (SSC)_l\ is\ the\ SSC\ matrix\ for\ inspected\ location\ l \\ i\ is\ the\ test\ device \\ j\ is\ the\ reference\ device \end{cases}$$

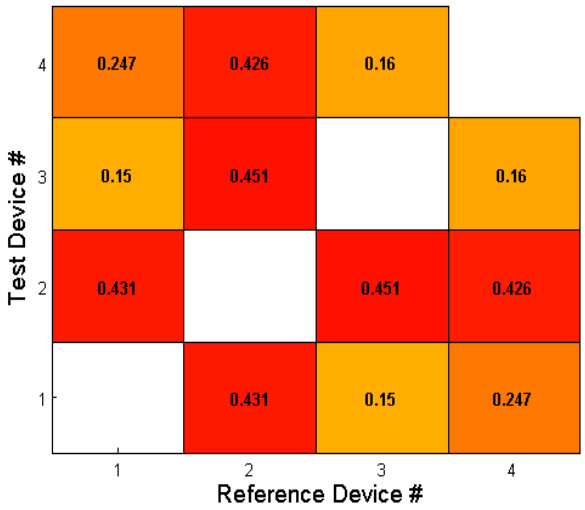

Figure 4.4.4 Matrix *B* — Sum of the MCC values of all inspected locations for the correlation of reference device *i* and test device *j*

2. The values across each row of matrix *B,* shown in Equation 4.4.3, are added; the resulting value *S(j)* contains the sum of the all correlations performed using device *j* as a reference. To make the results comparable with other inspections, regardless of the number of inspected locations and

devices, the sum is normalized by the product of the total number of inspection locations and devices. The resulting *S(j)* values for each of the four inspected capacitors are shown in Figure 4.4.5.

$$S(j) = \frac{1}{D*L}\sum_{i=1}^{D} B_{i,j} \tag{4.4.3}$$

$$where \begin{cases} D\ is\ the\ total\ number\ of\ inspected\ devices \\ L\ is\ the\ total\ number\ of\ inspected\ locations \\ B\ is\ the\ matrix\ derived\ from\ Equation\ 4.4.2 \\ i\ is\ the\ test\ device \\ j\ is\ the\ reference\ device \end{cases}$$

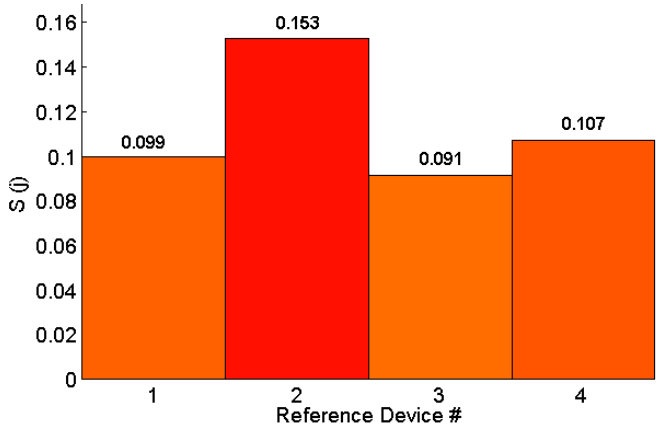

Figure 4.4.5 Normalized sum for all inspected capacitors at all inspection locations

3. The *S(j)* value for device 2 is considered an outlier because, *S(2)* is greater than μ + 0.5σ, where μ is the mean and σ is the standard deviation. This conservative threshold selects only the devices that respond most similarly, therefore making them suitable as references for the vibration responses of non-defective devices. Section 4.5 will provide an algorithm for rejecting these outliers when more devices are inspected. The time-

domain responses of the remaining devices, capacitors 1, 3, and 4, are then averaged at each inspected location and recorded as the hybrid reference signal.

Once the hybrid reference signal was established, the MCC method was used to correlate it with the signals from each of the four inspected capacitors. Even though the MCC method was used in this example, other signal processing methods, such as error ratio, wavelet analysis, and local temporal coherence, could have been used to correlate the responses of the hybrid reference signal and the inspected devices, and they would have produced similar results. Figure 4.4.6 shows the results of using each capacitor as a reference and correlating its time-domain responses with those of the other three capacitors at each inspected location. It was observed that some of the non-defective devices did not correlate well with each other. This showed that the differences in responses among the non-defective devices were large enough to make it difficult to determine whether or not they were defective. These large variations were, in large part, due to variations in these devices' boards, which were manually cut and of different dimensions. For all of the correlations performed, the highest MCC values occurred whenever the defective capacitor was correlated to a non-defective capacitor. These MCC results show that the manufacturing variations among non-defective devices may be large enough to produce misleading MCC results. For example, in Figure 4.4.6a, using capacitor 1 (BoardACap1) as a reference device, the MCC results appear to indicate that capacitor 4 (BoardBCap2) is defective. In contrast, when correlating the responses of capacitors 1 to 4 with the hybrid reference signal at the same inspection locations, it is clear that the defect is in capacitor 2 (BoardACap2). The correlation using the MCC with

the hybrid reference signal instead of the signal from a single non-defective device reduced the risk of falsely rejecting a good device.

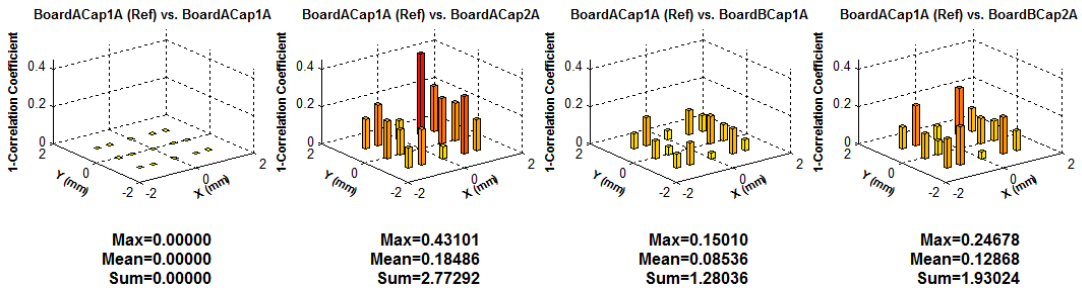

a) Capacitor 1 as reference

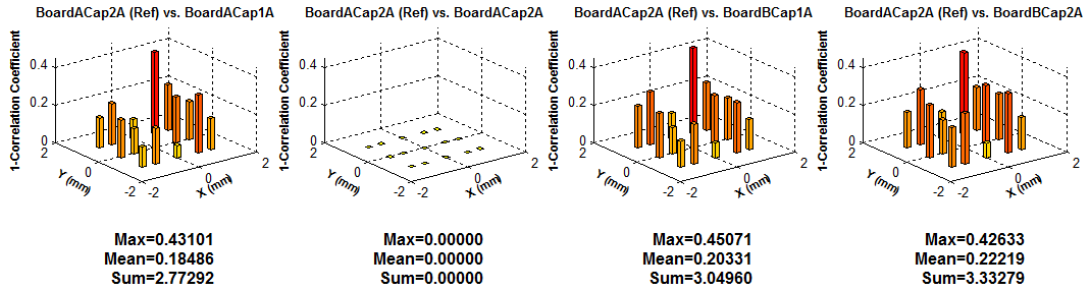

b) Capacitor 2 as reference

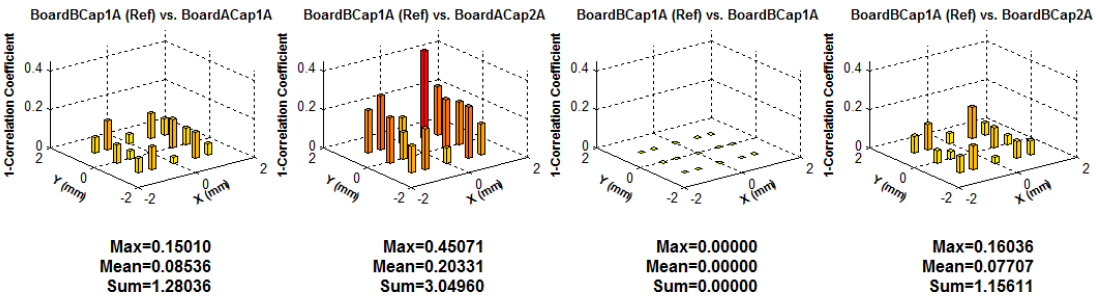

c) Capacitor 3 as reference

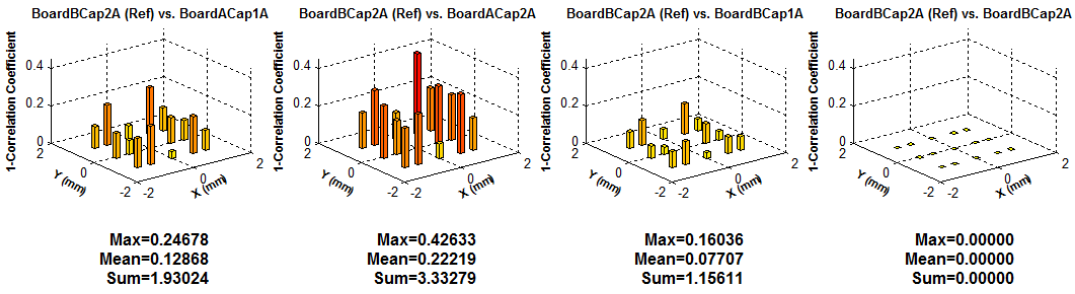

d) Capacitor 4 as reference

Figure 4.4.6 MCC method correlations with each inspected device used as reference

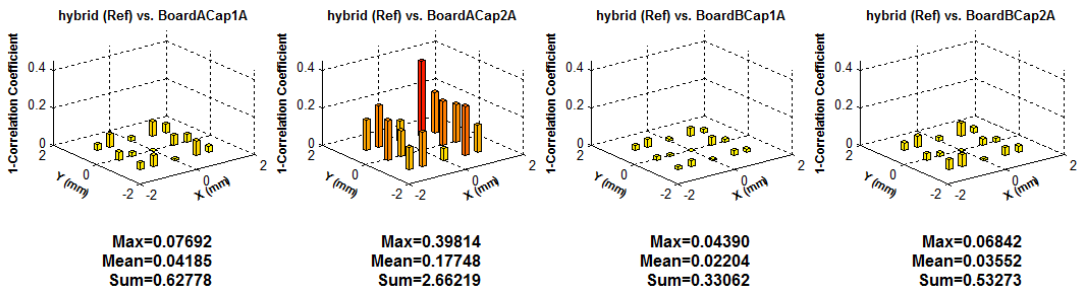

Figure 4.4.7 MCC method correlations with hybrid reference signal

4.5 Inspection of Flip Chip Packages

The inspection of the flip chip test vehicles was used to demonstrate the application of the SSC method to selecting the most suitable reference devices. These reference devices, selected from set SR, were then used to generate the hybrid reference signal.

The process begins with the calculation of the SSC matrix for all of the devices. Figure 4.5.1 shows the maximum SSC matrix for all inspected FCPs. The results immediately show that whenever a device in set SR (0 through 30) was correlated with a device in sets MR, R1 or R2 there was a larger MCC value (i.e., poor correlation). This indicates that, as a group, these two sets of devices respond differently and provides a quick indication that quality degradation has occurred in the solder bumps of the reworked and multiple reflow devices. Figure 4.5.2 illustrates that more variations in vibration responses were present in sets SR and MR than in sets R1 and R2. The single reflow devices (SR) were used to establish the reference vibration responses, which were then correlated with the reworked (R1 and R2) and multiple reflow devices (MR) using the MCC method.

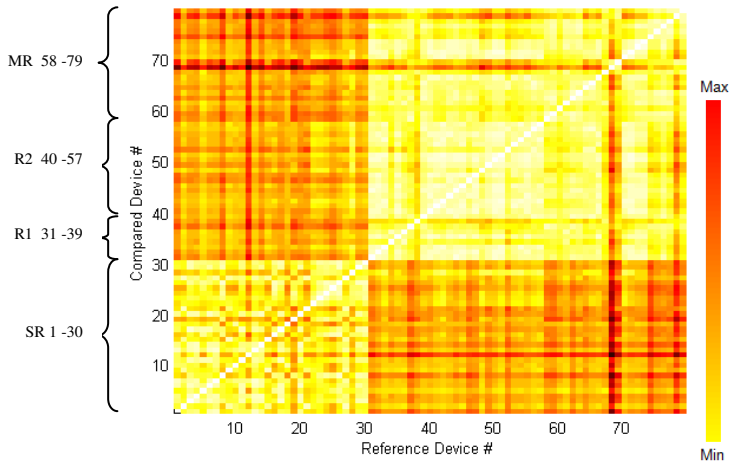

Figure 4.5.1 Maximum SSC matrix (*A*) shows the variations in response among all inspected flip chip devices

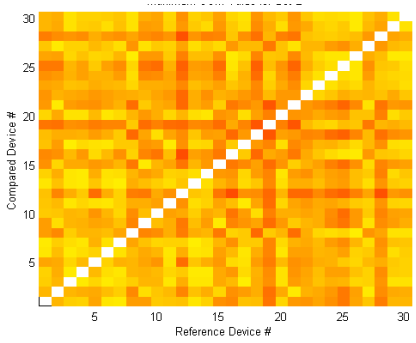

(a) maximum SSC matrix (*A*) for set SR

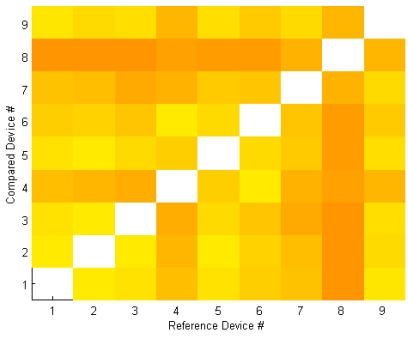

(b) maximum SSC matrix (*A*) for set R1

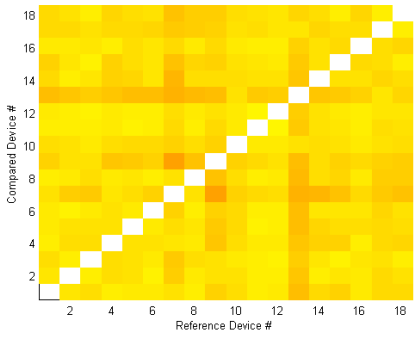

(c) maximum SSC matrix (*A*) for set R2

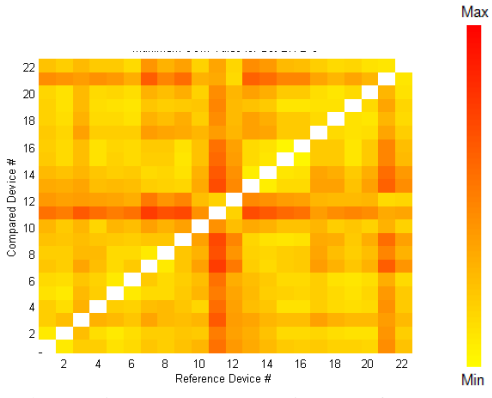

(d) maximum SSC matrix (*A*) for set MR

Figure 4.5.2 Variations in response among the devices within each sample set

Unlike the chip capacitor test vehicles, when there is a large number of samples it becomes increasingly difficult to identify outliers. Therefore, an algorithm was implemented to automatically identify the outliers, which were not included in deriving the hybrid reference signal.

The selection of the reference devices in set SR begins by calculating the SSC matrix at each inspected location. This information is then reduced to a single value *S(j)* for each device, according to Equation 4.5.1, The result of this operation for the devices in set SR are shown in Figure 4.5.3.

$$S(j) = device\ (j) = \frac{1}{D * L}\sum_{j=1}^{D}\sum_{l=1}^{L}\left(SSC_{i,j}\right)_l$$

$$where \begin{cases} l \text{ is the inspection location} \\ L \text{ is the total number of inspection locations} \\ j \text{ is the device} \\ D \text{ is the total number of devices} \end{cases}$$

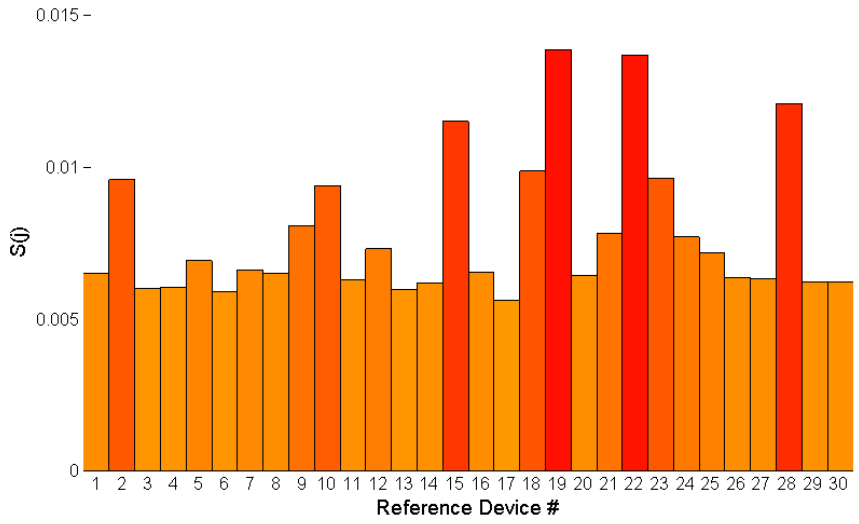

Figure 4.5.3 Selection value *S(j)* for all single reflow devices

The reference selection process was performed iteratively using the following procedure:

1. The S(j) value of the first five devices are used to calculate a mean, μ_0, and standard deviation, σ_0. If S(j) for any of these devices is greater than $\mu_0+0.5\sigma_0$, it is rejected and removed from the analysis. The mean μ_1 and standard deviation σ_1 are calculated for the remaining devices.

2. The S(j) value for the next device is then compared to $\mu_1 + 0.5\sigma_1$ from step 1. If it is greater than $\mu_1 + 0.5\sigma_1$, the device is rejected, otherwise it is added to the selection. Then a new mean, μ_2, and standard deviation, σ_2, are calculated for the selected devices.

3. The S(j) values for the currently selected device is then compared to $\mu_2 + 0.5\sigma_2$ to determine if there are outliers. A new mean, μ_3, and standard deviation, σ_3, are calculated.

4. Repeat steps 2 and 3 for all remaining devices.

Figure 4.5.4 shows that devices 3, 4, 6, 11, 13, 14, 17, 26, 27, 29, 30 were selected as reference devices through the above process.

The devices selected through this process were used to generate a hybrid reference signal for each inspected location. Figure 4.5.5 shows the response at inspection location 7 for all devices in set SR and the hybrid reference signal. The SSC method did not need to select all the good devices; it just needed to identify which

devices would make the best reference signal. A conservative selection threshold (μ+σ) reduces the risk of utilizing a defective device as part of the reference signal.

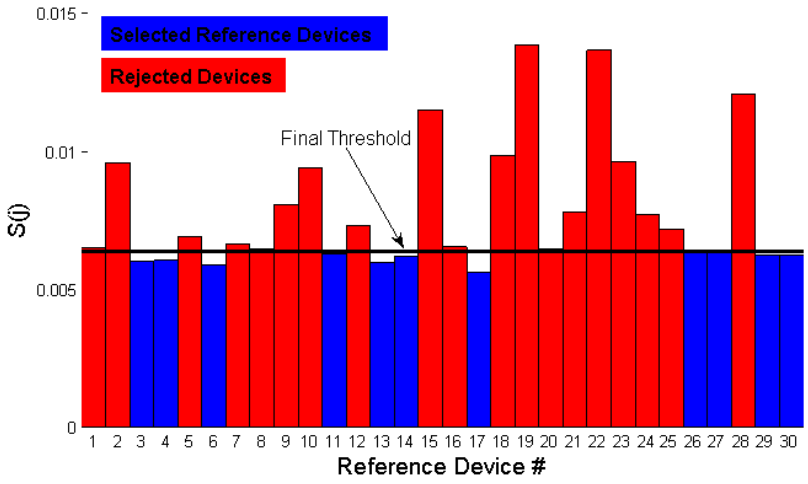

Figure 4.5.4 Results of iterative reference selection process

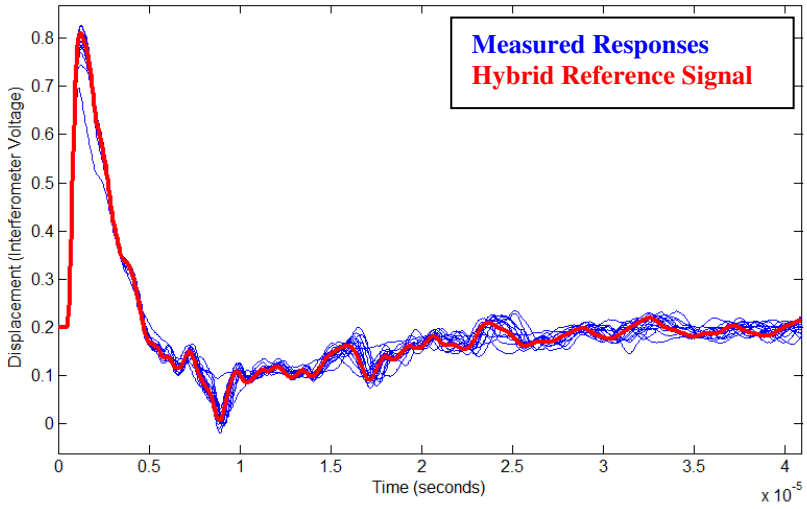

Figure 4.5.5 Hybrid Reference Signal and response from all devices in set SR at inspection location 7

Once the hybrid reference signal is generated and recorded, it is used for correlation with the individual responses of each of the devices. These correlations reveals the severity and locations of any defects and any quality degradation caused by the reflow or rework processes. The MCC method results are shown in Appendix F for all inspected devices. The MCC values for three selected devices in set SR are shown as examples in Figure 4.5.6: panel a) shows a non-defective device; b) shows one with quality degradation; c) shows the local effect of die chipping at the corner of the device. Figure 4.5.7 shows the results for devices in sets MR, R1, and R2. These results illustrate quality degradation due to the thermal cycling undergone by these devices.

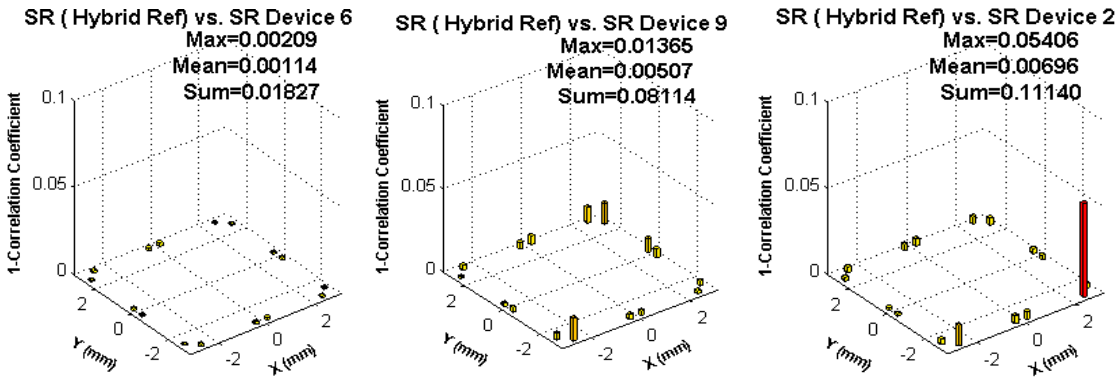

(a) non-defective (b) quality degradation (c) chipped edge

Figure 4.5.6 Selected results for devices in single reflow set SR

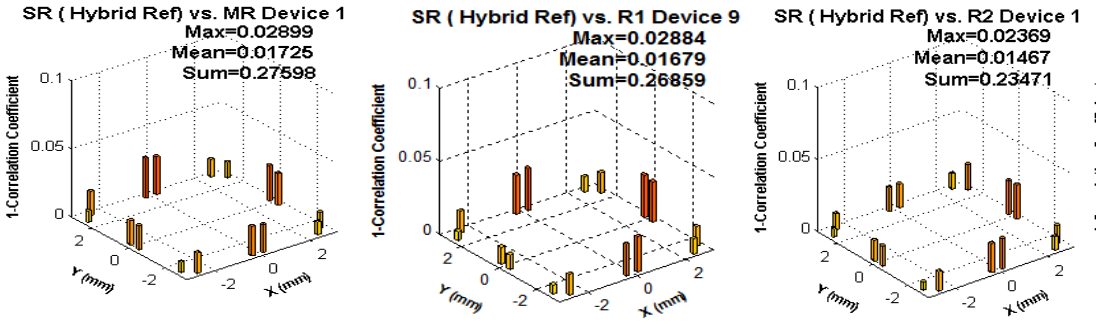

(a) multiple reflow (b) rework type I (c) rework type II

Figure 4.5.7 Selected results showing the quality degradation of the solder bumps in the devices in the multiple reflow and rework sets

The final step in the inspection was defining a threshold MCC value to identify the defective devices (including quality degradation due to thermal fatigue). Since the inspection results provided by laser ultrasonic inspection do not provide an explicit measure of the defects, the threshold for defective devices is defined as a function of the change in response. The threshold is determined from the MCC values for reference devices in set SR identified by the SSC method and it is defined as the maximum MCC value plus one standard deviation. The maximum MCC value for these devices was 0.0083, with a standard deviation of 0.0018. Therefore, the threshold for determining a defective device was 0.01 (MCC).

4.6 GUI Implementation of Simultaneous Signal Comparison Method

The SSC method was added to the set of analysis tools in the *SuperAnalysis* Matlab GUI used by this research group to process the measurement data collected by the laser ultrasonic inspection system. The changes to the GUI allow the user to perform the SSC analysis, to reselect only the devices that were automatically selected as references, and to create a hybrid reference signal.

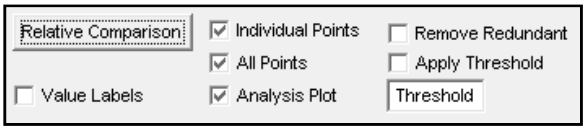

(a) simultaneous signal comparison panel

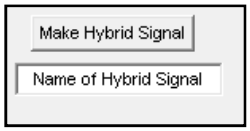

(b) hybrid signal panel

Figure 4.6.1 Additional GUI panels for SSC method and hybrid reference signal

4.7 Conclusions

The inspection of the chip capacitor and flip chip test vehicles demonstrated the use of the SSC method to identify the best reference devices. The responses of these selected reference devices were then used to make an average hybrid reference signal to serve as the vibration response benchmark. This new signal was used with the MCC method to identify the presence, severity, and location of defects in all of the inspected devices. The measurements also showed how the correlations in the SSC matrix can be used to access the manufacturing variations and distribution of defects within a set. The utilization of a hybrid reference signal instead of a single non-defective device reduces the risk of false identification due to the reference being far from the mean vibration responses of non-defective devices.

As previously discussed, an inspection plan using the laser ultrasonic inspection technique under development requires the establishment of a reference vibration response to be able to assess product quality. To determine which devices are suitable references, other non-destructive methods can be used prior to laser ultrasonic inspection or destructive methods after laser ultrasonic inspection. Since laser ultrasonic inspection is sensitive to process changes affecting solder bump material properties, a new reference

will be required and a constant reference response cannot be used. Therefore, a quick method for determining the appropriate reference devices is required.

The capability of determining the reference devices on-line will increase the application scope of the technique to manufacturing applications by enabling the quick determination of the reference response after any new batches are manufactured or when process changes are made. Continuous sampling of a small number of devices can be performed to establish the reference devices; then, a batch inspection approach can be utilized to inspect and determine the quality of boards with multiple devices.

The analysis performed in this chapter was limited to measuring quality degradation due to thermal cycling during multiple reflow and rework. Defects such as missing, misaligned, open, and starved solder bumps were not explicitly studied. Although these defects can be detected with the laser ultrasonic technique, their localized effects on the changes in vibration response may affect the results of the SSC approach. Further study will be needed to determine how multiple devices with the exact same defect (in severity and location) will impact the analysis results.

Chapter 5: Detection of Solder Bump Cracks in High-Density Flip Chip Packages

Previous work by Yang and Zhang has shown the ability of laser ultrasonic inspection to detect open, cracked, and missing solder bump defects induced during assembly or through thermal fatigue in a variety of flip chip, LGA, and BGA packages [Yang, J., 2008, Zhang, L., 2006]. With solder bump interconnects becoming smaller and being used in greater density, it is increasingly challenging to inspect these devices at high speed and low cost. This rapid progression in the requirements for non-destructive inspection of electronic packages makes it necessary to continuously assess the capabilities of the laser ultrasonic inspection technique. This chapter presents a preliminary study of the application of laser ultrasonic inspection to detecting cracked solder bumps in a high-density flip chip device.

5.1 Flip Chip Test Vehicle

Two samples of the high-density flip chip package shown in Figure 5.1.1 were inspected. This high density 11 mm by 11 mm device has over 4000 solder bump interconnects at a pitch of approximately 150 μm. One was a known-good reference device, and the other had corner solder bump crack defects that the manufacturer created by carefully bending the substrate corner. The presence of these solder bump cracks was verified by x-ray inspection prior to performing the laser ultrasonic inspection. The location of the solder bump interconnects shown in Figure 5.1.2 was supplied by the manufacturer, but the fiducials and device locations were extracted using high-resolution images, as described in Chapter 2.

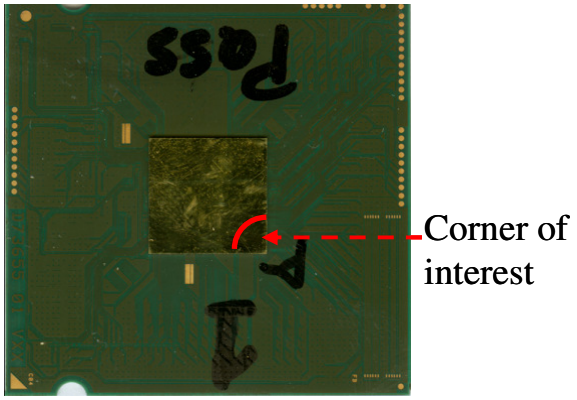

Figure 5.1.1 High-density flip chip package

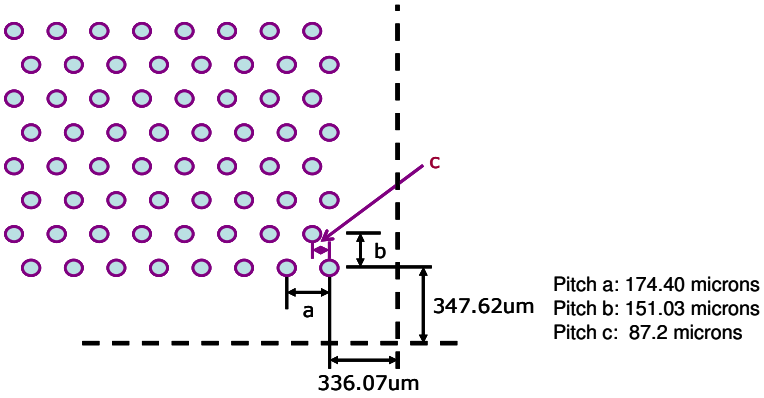

Figure 5.1.2 Solder bump layout at the inspection corner

The chosen inspection pattern, shown in Figure 5.1.3, has 25 inspection locations: points 2 through 25 lie on top of the solder bumps in the corner of the die, and points 1 and 2 are diagonal from the corner. The purpose of inspection points one and two is to investigate whether a single measurement taken at the corner of the die can capture the change in vibration response caused by the defective solder joints. A laser power density of 0.120 J/cm^2 was chosen to avoid damaging the surface of the device, using the experimental determination of the ablation threshold and energy density calibration

presented in Chapter 2. The focused laser spot was located at (1.0 mm, - 0.5 mm) from the corner of interest.

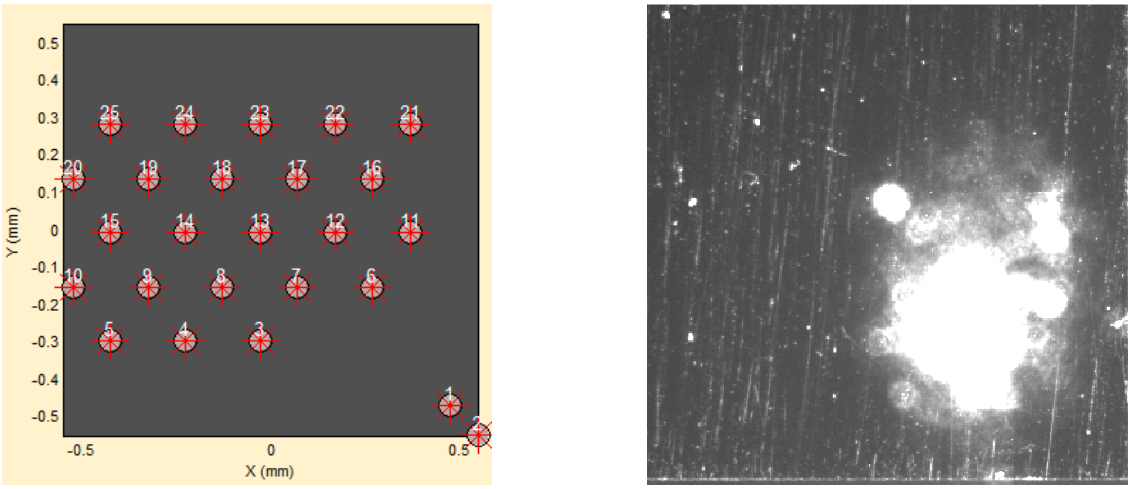

(a) inspection locations on die corner (b) scattered light from focused laser spot

Figure 5.1.3 Inspection locations on chip corner and focused laser spot

5.2 Results and Discussions

The measurement repeatability of the laser ultrasound inspection system for these flip chip devices was demonstrated by correlating two independent measurements of each device. The repeatability measurement results using the Modified Correlation Coefficient (MCC) method are shown in Figure 5.2.1 for the reference chip (Board A) and the chip with cracked solder bumps (Board B). These correlations demonstrate the system repeatability and also serve the purpose of establishing the scale for the MCC correlations between the reference and defective devices.

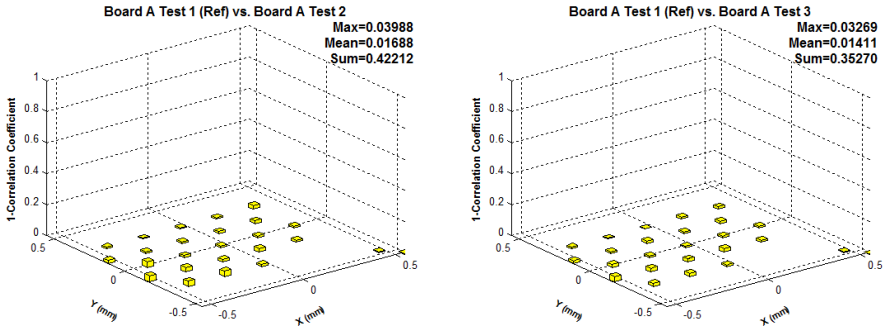

(a) know-good device

(b) know-good device

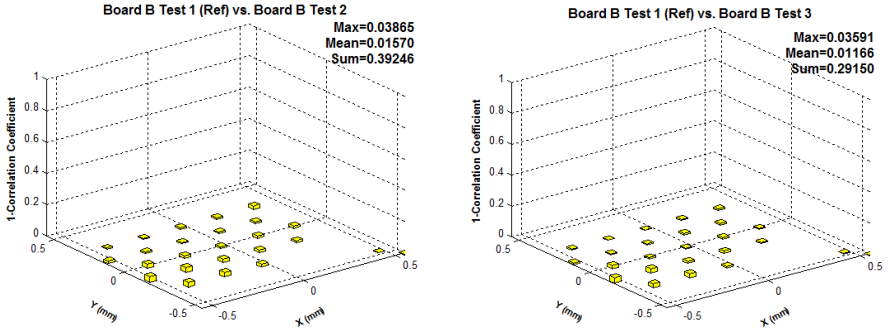

(c) defective device

(d) defective device

Figure 5.2.1 Measurement repeatability study of high-density flip chip packages

The time-domain response at inspection point 1 of each device is shown in Figure 5.2.2. It can be clearly observed that the two devices have a very different vibration response. This change in local vibration response is caused by the cracked solder bumps of device on Board B. The three measures of the defective device were correlated to those of the known-good device using the MCC method, and the results are displayed in Figure 5.2.3. The large correlation values for the measurements at the corner show that the cracked solder bumps were detectable using the laser ultrasonic technique.

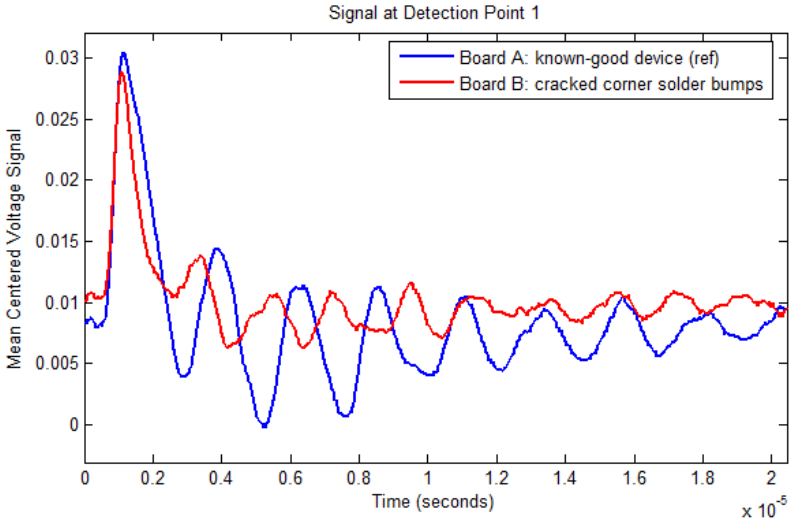

Figure 5.2.2 Time domain signals at inspection point 1 of both the flip chip with cracked solder bumps and the know-good reference device

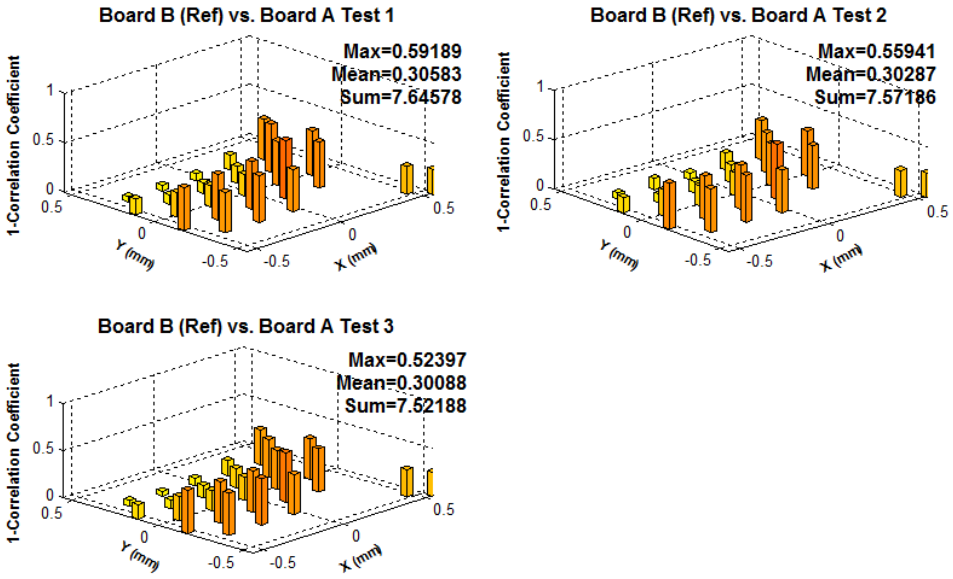

Figure 5.2.3 Correlation between known-good reference device and flip chip with cracked corner bumps

Chapter 6: Summary, Contributions, and Recommendations

6.1 Summary

The realization of the research objectives presented in this thesis directly addresses some of the current limitations in the use of laser ultrasonic inspection for on-line and high-volume applications.

The implementation of a local excitation/measurement scheme will allow the current system to inspect higher density devices. This method is able to identify the presence of open bump defects in flip chip devices. The local excitation/measurement scheme also localizes the effects that defects have on structural vibration, allowing easier identification of the defect location. The hardware implementation of this scheme also simplifies the automation of the system by making it unnecessary to go through the process of repositioning the focusing objective for every device, saving approximately 45 seconds per inspected device.

Another important development was the Simultaneous Signal Comparison (SSC) method, which uses the data from a sample set of inspected devices to determine which are most likely to be non-defective. These devices are then selected to make a hybrid reference signal, which is then used as a reference for defect detection. The implementation of this method makes it possible to identify defective devices without a pre-established known-good reference and removes the need to utilize other expensive and time-consuming non-destructive methods to find a single reference device. The SSC method is also used to analyze the variation among the inspected samples.

6.2 Contributions

My contribution to the development of the laser ultrasonic technique focused on expanding the application scope towards on-line and high-volume inspection. My research can be summarized as follows:

1. Development of a fixture and a method for measuring the distance between the interferometer and camera. This measurement was utilized to perform coordinate transformations during the inspection setup process. The developed method was able to precisely measure the distance and to maintain system repeatability after hardware changes were made. The application of this method will allow data taken before and after any system changes to be compared.

2. Characterization of the delivered energy density as a function of laser power level and the offset of the focusing stage. This characterization was used to experimentally determine the onset of ablation for a gold-coated flip chip device. The surface ablation on the FCP was tracked for the achievable laser energy densities to provide an experimental measure of the surface damage. This investigation also revealed that surface irregularities, such as scratches or cracks, can significantly increase the laser energy absorption and induce damage at lower power levels. The method utilized to perform these measurements can be used in the future to determine the appropriate power level when inspecting new devices.

3. Development of an image processing algorithm to make measurements of the device and reference fiducial locations. This algorithm was required to set the inspection system up for every new device and board configuration. Future researchers can use the

method to quickly acquire this coordinate information whenever it has not been provided by the device manufacturer.

4. Implementation and validation of a new excitation/measurement scheme, which was developed to address the testing problems caused by stiffer devices. The local excitation method provided a consistent energy level for all inspection locations and demonstrated its ability to identify defects in flip chip devices. Also, because ultrasound generation is localized, the vibration response changes due to defective interconnects are more localized.

5. Development of an algorithm for selecting reference devices. The SSC method was used to identify non-defective devices that serve as vibration response references and used to derive a hybrid reference signal. The responses of the selected reference devices were averaged at each inspection location to build a hybrid reference signal; this signal was then be used with the modified correlation coefficient (MCC) method, local temporal coherence, or wavelet analysis to identify defective devices. The results showed that, for the test vehicles that were investigated, this approach was able to select non-defective devices. Analyzing the responses of the inspected devices using the MCC method and the hybrid reference signal made it possible to measure the quality degradation due to thermal cycling in flip chip devices and cracked chip capacitors. Further validation work is needed to demonstrate that this approach to establishing a set of reference devices will work for other test vehicles and will detect and measure different types of defects.

6. Demonstration of the capability of the laser ultrasonic inspection technique to detect cracked solder bumps in high-density flip chip devices.

6.3 Recommendations

6.3.1 Finite Element Modeling

Many researchers have developed analytical models of laser-generated ultrasonic waves in semi-infinite media. The solutions for these models are useful in cases where the boundary conditions are straightforward — i.e., where the area of interest is far from the edges and there are few reflections. In the case of laser-generated ultrasound in microelectronic packages, this solution becomes very complex. First, the entire three-dimensional structure must be modeled, making it difficult to apply the boundary conditions for all of the interconnects. Second, the usual areas of interest lie close to the free edges of the structure, requiring very small time steps. Finally, because the wave speed in silicon is on the order of 8700 m/s, many reflections occur within the small boundaries (usually less than 1cm by 1 cm) of a microelectronic device, making the calculations unreasonably complicated. Therefore, approaching the problem as a thermomechanical finite element (FE) simulation is recommended to investigate the following aspects of laser-generated ultrasound in microelectronic devices:

1. Modal analysis has been used to identify which modes of vibration are more sensitive to a particular defect location and it was useful in frequency domain analysis, such as Wavelet Analysis and Local Temporal Coherence methods [Yang, J., 2008]. Knowing which modes were most sensitive to the changes in vibration caused by defects provided a guideline for selecting the bandwidth of the analysis. This analysis was performed for a flip chip test vehicle with 48 solder bumps on the periphery of the device. In this case, the ultrasound excitation generated the two modes with the most sensitivity; but this is not always the case. As seem in the local excitation/measurement

method, different excitation locations and device geometries will affect the modes generated by the laser ultrasound; therefore, modal analysis is not sufficient for simulating and representing the underlying physics of the vibrations caused by laser-generated ultrasound. A time-domain model simulating the generation and propagation of the laser-induced stress/strain field is required to find which modes of vibration are actually generated for the particular device being inspected.

2. Another important motivation for creating an FE model is the need to understand and study the sensitivity of the laser ultrasonic technique. As previously discussed, the change in vibration response caused by a defective solder bump depends on the structure of the device, the geometric configuration of the interconnects, and the location of the defect(s). Experimental results for a variety of test vehicles have showed that the effect of defective solder bumps is not necessarily localized to the defect locations but affects the whole structure. This is due to the excitation of the complete package and the shift in mode shape caused by the defect(s) [Yang, J.,2008]. Therefore, it is imperative to perform a time-domain FE simulation of the laser-ultrasound-induced vibrations to determine: 1) whether the change in vibration is always larger at the defect location; 2) whether the magnitude of the change in vibration response (as measured with a method such as MCC) remains the same regardless of the location of the defect and how this affects the sensitivity of the technique; and 3) what locations on the device are most sensitive to the changes in vibration caused by defective interconnects.

The FE simulation of laser-ultrasound-induced vibration can be approached as a thermomechanical simulation. First, the laser pulse is modeled as a transient heat flux incident on the device surface. The resulting transient temperature field is applied to the

structure to calculate the thermal stresses/strains. The resulting out-of-plane displacement can then be extracted and analyzed using any of the signal processing methods generally used.

The thermomechanical approach has been extensively used by Xu to achieve a numerical solution for the temperature field generated by the laser and to perform an FE simulation of the subsequent wave propagation [Xu, BQ., 2004]. The geometric model used in that research was straightforward, the size of the medium was small and a high mesh density could be used to completely resolve the temperature field. This presents a challenge when modeling a device which is several orders of magnitude thicker than the micron-sized temperature gradient. FE simulation of the laser ultrasonic technique is a challenging task when a complete device must be modeled, particularly in 3D.

Developing an FE model of a microelectronic device will be crucial in understanding the vibration behavior of the structure under laser ultrasonic excitation and the effects that defective interconnects have on its vibration response.

6.3.2 Automation and System Integration

A fully automated system is needed to demonstrate the capabilities of the laser ultrasonic and interferometric inspection system as a tool for on-line inspection of microelectronic devices. Automating the system will increase throughput, improve repeatability, reduce the overall operating costs, and minimize the training required to operate it. Automation is also required to be able to inspect larger devices with more inspection locations. Furthermore, a fully automated system would aid researchers in

performing more extensive studies. The automation of the system encompasses the following:

1. Automatic auto-focusing of the interferometer is needed to seamlessly automate the data capture process. Current advances will make this possible, but the auto-focusing system and data capture must be integrated to fully realize the potential of this feature.

2. Currently, when the local excitation method is not used, an operator must relocate the manual X-Y stage supporting the focusing objective for every device inspected. Automating this process would require the addition of another computer-controlled X-Y positioning stage, along with the supporting hardware and software. The hardware implementation of this approach may require extensive modification of the current system because of the added weight and possible interferences. The local excitation method presented here may avoid this problem, but further research is needed to analyze the impact of this option.

3. Currently, five different programs are used during the setup calibration: to generate the motion control file for the X-Y positioning stage, to capture images for setup calibration, to control manual X-Y positioning stage motion, and to acquire data. This fact adds complexity and time to the process of setting each board up for inspection. A single program is needed to perform all of these functions with a user-friendly graphical user interface (GUI). Creating this software will involve communicating with the automated X-Y stage, digital camera, data acquisition card, and interferometer autofocusing system. The GUI must also provide a standardized way to input the board and device coordinates.

4. System calibration plays a crucial part in maintaining repeatability in this inspection system. Without a precise calibration process, measurements taken after any system modifications will not be comparable to those from prior inspections. Two particular calibration measurements are critical and should be added to any software created to control the system: first, the measurement of the vector (P_{inter}) that describes the position of the interferometer relative to camera; second, the distance between the center of the camera and the zero position of the manual stage (P_{laser}). These two calibrations should be added to the program to make the process more streamlined and consistent between different operators.

Once all of the listed steps towards integration have been accomplished, the inspection system would be able to make the setup calibration measurements and inspect multiple devices on a single board completely autonomously.

6.3.3 Testing of Advanced Devices

In order for the capabilities of the inspection technique to continue to be relevant to advances in the electronic packaging industry, the laser ultrasonic technique needs to be continuously applied to modern devices. Experiments on these new devices must be performed to identify the challenges presented by over molding and other surface coatings, higher solder bump density, and decreased pitch. Although flip chips, chip scale and chip capacitors have been successfully tested, BGA packages still present a challenge. The two main challenges identified by the work presented in this thesis are:

1. The scattering of light caused by the rough opaque surfaces of most BGA devices makes it difficult to effectively focus the interferometer. This causes an increase in the

amount of noise from the interferometer controller. The noise in the signal is sufficient to mask the vibration changes caused by defective interconnects. It was also observed that markings on the device surface further reduced the quality of the interferometer signal.

2. Variations in power levels from one inspection location to another have been observed when testing BGA devices. This is due to the attenuation of the mechanical wave by the plastic molding on the device. The reduced vibration amplitude causes the adverse effects of noise to be more predominant. Also, when testing BGA devices, the energy density must be lower than in flip chip devices, because of material properties of the molding. This problem can be addressed by using the local excitation/measurement scheme presented in this thesis.

6.3.4 Further Development of the Automated Reference Selection Algorithm

The SSC method for reference selection must be studied further to identify how the distribution of defective devices affects the analysis results. This study may be performed through the use of a model that can simulate the variations in vibration response caused by manufacturing variations and defects. By applying the SSC method to this model, the results of the reference selection algorithm can be studied for many different cases and distributions of defects. The model can also be used to simulate on-line reference selection and the inspection process. This approach would allow for a known distribution of defects and for manufacturing variations.

The derivation of the threshold used to determine defective devices must also be further developed. This threshold (in terms of MCC value or other signal comparison method) can be established with the use of a training set of devices. First, the initial

devices can be inspected to establish a priori distribution of the vibration response and manufacturing variations. Second, progressive thermal cycling followed by laser ultrasonic inspection and destructive testing can be used to determine the changes in vibration response caused by *n* thermal cycles, which will eventually lead to through cracks and failure of the solder joint [Yang, Jin.,2008]. Finally, the acceptance level can be chosen according to the manufacturer's quality requirements for solder bump quality. The same procedure can then be followed for assembly defects, such as missing, open and misaligned solder bumps.

Appendix A: Matlab Code for Image Processing Algorithms

A.1 Damage Threshold Measurements

```
close all
clear all
clc

T=100;                                  %threshold

A=imread('corner.bmp');                 %before
E=imread('corner6.bmp');                %after
Damage=E-A;                             %difference

blobs=bwlabel(im2bw(Damage,T/256));     %extract blobs( grayscale to binary)
imshow(bwlabel(im2bw(Damage,T/256)))    %plot image
Props=regionprops(blobs,'Area');        %measure blob area

Area=0;
for i=1:size(Props,1)                   %extract blobs
   if Props(i).Area>2
      Area=Area+Props(i).Area;
   end
end
% Area=(7.4^2)*(1/(1000^2))*Area
eval(['Area' int2str(42/1.4835)  '=' int2str(Area) ])
```

A.2 Laser Spot Size Measurements

```
clc
clear all
close all
im_01=imread('focus002.jpg');
[x,y,z]=size(im_01);
spots=[15,17.5,20,20.5,21,21.25,21.5,21.75,22,22.25,22.5,22.75,23,23.5,24,25];
im_02=zeros(x,y,z);
split=[1,1,1]

im_02(i,j,1)=split(1)*im_01(i,j,1)/255+split(2)*im_01(i,j,2)/255/2+split(3)*im_01(i,j,3)/
255/2;
for i=1:x
   for j=1:y
      if im_01(i,j,1)>10
         im_02(i,j,1)=1;
      end
   end
end

blobsA=bwlabel(im2bw(im_02,.1));

Areas=regionprops(blobsA,'Area');
Centroids=regionprops(blobsA,'Centroid');

blob_count=length(Areas);
count=1;
for i=1:blob_count
   if Areas(i).Area(1)>1000
      blob_data(count,1)=spots(17-count);
      blob_data(count,2)=Areas(i).Area(1);
      blob_data(count,3)=Centroids(i).Centroid(1);
      blob_data(count,4)=Centroids(i).Centroid(2);
      count=count+1;
   end
end
% Gives results from bottom to top of page
imshow(blobsA)
```

A.3 Fiducial Locations Measurement

```
clc
clear
BoardA=imread('Board003 - Copy.jpg');
BoardB=imread('Board004 - Copy.jpg');

% BoardA_HSV=rgb2hsv(BoardA);
% BoardB_HSV=rgb2hsv(BoardB);

Ax=size(BoardA,2)
Ay=size(BoardA,1)
Bx=size(BoardB,2)
By=size(BoardB,1)

MaskA=BoardA(:,:,1)-BoardA(:,:,3);
MaskB=BoardB(:,:,1)-BoardB(:,:,3);

% MaskAA=imadjust(MaskA,[30/255,100/255],[],0.5);
% MaskBB=imadjust(MaskB,[30/255,100/255],[],0.5);

MaskAA=imadjust(MaskA,[30/255,80/255],[],0.5);
MaskBB=imadjust(MaskB,[30/255,80/255],[],0.5);
MaskAA=medfilt2(MaskAA,[3 3]);
MaskBB=medfilt2(MaskBB,[3 3]);

% MaskAAA=im2bw(MaskAA,100/255);
% MaskBBB=im2bw(MaskBB,100/255);

MaskAAA=im2bw(MaskAA,100/255);
MaskBBB=im2bw(MaskBB,100/255);

imshow(MaskBBB)

blobsA=bwlabel(MaskBBB);
Areas=regionprops(blobsA,'Area');
Centroids=regionprops(blobsA,'Centroid');
Major=regionprops(blobsA,'MajorAxisLength');
Minor=regionprops(blobsA,'MinorAxisLength');
Ecent=regionprops(blobsA,'Eccentricity');
blob_count=length(Areas);
```

```
count=1;
for i=1:blob_count
   if Areas(i).Area(1)>200 && Areas(i).Area(1)<6000
      blob_data(count,1)=Ecent(i).Eccentricity(1);
      blob_data(count,2)=Areas(i).Area(1);
      blob_data(count,3)=Centroids(i).Centroid(1);
      blob_data(count,4)=Centroids(i).Centroid(2);
      count=count+1;
   end
end
count=1;
for i=1:size(blob_data,1)
   if blob_data(i,3)/Ax>300/Ax && blob_data(i,3)/Ax<6000/Ax
      reference(count,1)=blob_data(i,1);
      reference(count,2)=blob_data(i,2);
      reference(count,3)=blob_data(i,3);
      reference(count,4)=blob_data(i,4);
   end
   count=count+1;
end
reference
```

Appendix B: Matlab Code for P_{inter} Measurements and Calibration

B.1 Surface Fit and Moment Method

```
clc
clear all
close all
filename='C:\Users\mako\Documents\School\Research\System Calibration\fIBER
cALIBRATION.xls';

Data=xlsread(filename,'Xsweep');
lines=size(Data,2)/3+0;
hold off
index=0;
for i=1:lines
   m=(i*3)-2;
   Data(:,m+2)=Data(:,m+2)+(rand(size(Data,1),1).*(Data(:,m+2)))*.01;
   plot3(Data(:,m),Data(:,m+1),Data(:,m+2),'-ro','MarkerFaceColor','b');
   for d=1:size(Data,1)
      AllData(d+index,:)=Data(d,m:m+2);
   end
   index=index+d;
   if i==1
         hold on
   end
   Rxx(i)=dot(Data(:,m),Data(:,m+2))/sum(Data(:,m+2));
end
Rx=dot(Data(:,1),Data(:,3))/sum(Data(:,3));

Data=xlsread(filename,'Ysweep');
lines=size(Data,2)/3+0;
for i=1:lines
   m=(i*3)-2;
   Data(:,m+2)=Data(:,m+2)+(rand(size(Data,1),1).*(Data(:,m+2)))*.0000001;
   plot3(Data(:,m),Data(:,m+1),Data(:,m+2),'-ko','MarkerFaceColor','b');
   for d=1:size(Data,1)
      AllData(d+index,:)=Data(d,m:m+2);
   end
   index=index+d;
   Ryy(i)=dot(Data(:,m+1),Data(:,m+2))/sum(Data(:,m+2));
end
```

```
Ry=dot(Data(:,2),Data(:,3))/sum(Data(:,3));


line([Rx,Rx],[Ry,Ry],[0,5],'LineWidth',2)
legend('X direction sweep','Y direction sweep','Calculated FiberCenter ')


xlabel('X Stage Location (absolute steps)','FontSize',12)
ylabel('Y Stage Location (absolute steps)','FontSize',12)
zlabel('Measured Intensity (V)','FontSize',12)
Title('Intensity Profile of Vertical Optic Fiber','FontSize',12)
% grid on

R=(170e-3)*12800/2;
theta=[0:.1:2*pi];
Temp=ones(1,size(theta,2))*4.7;
for l=1:size(theta,2)
   X(l)=R*cos(theta(l))+Rx;
   Y(l)=R*sin(theta(l))+Ry;
end
% plot3(X,Y,Temp,'-k','LineWidth',4)
% plot3(X,Y,Temp-.5,'-k','LineWidth',4)
% plot3(X,Y,Temp-1,'-k','LineWidth',4)
close all
figure
XX=[min(AllData(:,1)):25:max(AllData(:,1))];
YY=[min(AllData(:,2)):25:max(AllData(:,2))];
ZZ=griddata(AllData(:,1),AllData(:,2),AllData(:,3),XX,YY');
mesh(XX,YY,ZZ)
xlabel('X Stage Location (absolute steps)','FontSize',12)
ylabel('Y Stage Location (absolute steps)','FontSize',12)
zlabel('Measured Intensity (V)','FontSize',12)
Title('Intensity Profile of Vertical Optic Fiber','FontSize',12)

RX=0;
RY=0;
SZZ=0;
for i=1:size(XX,2)
   for j=1:size(YY,2)
      if 0==isnan( ZZ(j,i) )
```

```
        RX=RX+XX(i)*ZZ(j,i);
        RY=RY+YY(j)*ZZ(j,i);
        SZZ=SZZ+ZZ(j,i);
        end
    end
end

RXXX=RX/SZZ
RYYY=RY/SZZ
line([RXXX,RXXX],[RYYY,RYYY],[0,5],'LineWidth',2)
```

B.2 Polynomial Fit Method

```
clear all
close all
clc


nx=10; %poly-fit parameters
ny=6;

CCD=[255680-352300]; %Camera Location

%%%% [Steps,Intensity] for X direction sweep
XS=[-11580    0.81
-11480 4.75
-11380 4.84
-11330 4.85
-11280 4.85
-11230 4.85
-11180 4.85
-11170 4.86
-11160 4.86
-11150 4.86
-11140 4.86
-11130 4.86
-11120 4.85
-11080 4.85
-10980 4.78
-10880 1.16];

%%%% [Steps,Intensity] for Y direction sweep
YS=[-395990  0.16
-395890        2.2
-395790        4.84
-395740        4.85
-395730        4.85
-395720        4.86
-395700        4.86
-395690        4.86
-395680        4.86
-395670        4.86
```

```
-395660         4.85
-395640         4.85
-395590         4.85
-395490         4.84
-395390         4.79
-395290         0.5
-395190         0.08];

%%%% X axis
[p,s] = polyfit(XS(:,1),XS(:,2),nx);
FX=[min(XS(:,1)):10:max(XS(:,1))];
FZ = polyval(p,FX);
for i=1:size(FX,2)
   if FZ(1,i)>=4
      FZZ(1,i)=FZ(1,i);
   else
      FZZ(1,i)=0;
   end
end
RX=(FX(1,:)*FZZ(1,:)')/sum(FZZ(1,:));

figure
subplot(2,1,1)
plot(XS(:,1),XS(:,2),'-o')
hold on
plot(FX,FZ,'r')
plot([RX,RX],[0,5])


%%%% Y axis
clear FX FZZ p s YX
[p,s] = polyfit(YS(:,1),YS(:,2),ny);
FX=[min(YS(:,1)):10:max(YS(:,1))];
FZ = polyval(p,FX);
for i=1:size(FX,2)
   if FZ(1,i)>=4
      FZZ(1,i)=FZ(1,i);
   else
      FZZ(1,i)=0;
   end
```

```
end
RY=(FX(1,:)*FZZ(1,:)')/sum(FZZ(1,:));

subplot(2,1,2)
plot(YS(:,1),YS(:,2),'-o')
hold on
plot(FX,FZ,'r')
plot([RY,RY],[0,5])

MXX=MX*ones(1,size(XS,1));
MYY=MY*ones(1,size(YS,1));
figure
plot3(XS(:,1),MXX(1,:),XS(:,2),'b')
hold on
plot3(MYY(1,:),YS(:,1),YS(:,2),'r')
plot3([RX,RX],[RY,RY],[0,5],'g')

%Calculate P Inter Method
Pinter=[RX-CCD(1,1),RY-CCD(1,2)]*(2.54/12800)*1e-3;  %in m
Pinter=[RX-CCD(1,1),RY-CCD(1,2)]
```

Appendix C: Matlab Code for Hybrid Signal Generation

C.1 Make_Hybrid Functions

```
function Make_Hybrid(Good_ref_name, Good_ref, h, eventdata, handles)

dirs = handles.dirs;
scan_dir_index = handles.scan_dir_index;
total_samp = str2num(get(handles.text_tot_samp_mod,'String'));
samp_rate = str2num(get(handles.text_samp_rate_mod,'String'));
period = 1/samp_rate;
StartN = str2num(get(handles.edit_start,'String'));
EndN = str2num(get(handles.edit_end,'String'));
total_dect_pts = length(handles.plots_selected);

for i = 1:total_samp                                    %create one time vector for all data
   time(i) = (i-0)*period;
end

% figure
% hold on
for Dpoint=1:size(Good_ref,1)
   good_device=1;
   for Device=1:size(Good_ref,2)
      if Good_ref(Dpoint,Device)~=0
            cd(dirs{scan_dir_index(Good_ref(Dpoint,Device))})
            fid = fopen(strcat(Good_ref_name{Dpoint,Device},int2str(Dpoint),'.txt'));
            file_temp = fscanf(fid,'%f', total_samp);
            fclose(fid);
            Selected_Data(good_device,:)=file_temp';
            good_device=good_device+1;
      end
   end
   average=zeros(1,total_samp);
   for p=1:size(time,2)
      average(1,p)=mean(Selected_Data(:,p));
   end
%     plot(time,average)
   for Device=1:size(Good_ref,2)
      if Good_ref(Dpoint,Device)~=0
         fid = fopen(strcat(get(handles.hybrid_name,'string'),int2str(Dpoint),'.txt'),'w');
```

```
            fprintf(fid,'%f',average(1,:));
            fprintf(fid,'%E',time(1,:));
            fclose(fid);
        end
    end
end
```

Appendix D: Matlab Code for Simultaneous Signal Comparison Method

D.1 Simultaneous Signal Comparison

```
function devices_selected=ERselect2(handles)
   border=0;
   clc

   DATA=Load_Data(handles);
   Threshold=str2num(get(handles.TH2,'String'));

   StartN = str2num(get(handles.edit_start,'String'));
   EndN = str2num(get(handles.edit_end,'String'))-1;
   total_dect_pts = length(handles.plots_selected);
   scans_selected = get(handles.listbox1_scans,'Value');
   scans = get(handles.listbox1_scans,'String');
   devices_selected=scans_selected;
   %list for comparison names
   for i=1:length(scans_selected)
      scan_names(1,i+1)=scans(scans_selected(1,i));
   end


   Results=zeros(size(scans_selected,2),size(scans_selected,2));
   ER_ALL=zeros(size(scans_selected,2),size(scans_selected,2),total_dect_pts);

%Find Absolute Maximum to find plot scale_____________________________________
   for p=1:total_dect_pts
      TEMP(:,:)=DATA(:,p,:);
      ER_ALL(:,:,p)=1-corrcoef(TEMP);
      M(p)=max(max(ER_ALL(:,:,p)));
   end
   MAX=max(M);
%_____________________________________________________________________________
%__________________Plot Individual Detection Point Comparisons________________
%_____________________________________________________________________________

   if get(handles.IndividualPoints,'Value')==1
```

```
%plot options
border=1;   %border around patches drawns by drawcolumn
col=2;      %number of rows and columns per figure
row=2;

figure
count=1;
SUM=zeros(length(scans_selected),length(scans_selected));
%plot
for p=1:total_dect_pts
%calculate values
TEMP(:,:)=DATA(:,p,:);
ER=1-corrcoef(TEMP);
SUM=SUM+ER;
%deside when new window
if p > count*(col*row)
   count=count+1;
   figure
end
subplot(2,2,p-(row*col)*(count-1))
axis([(0+.5) (length(scans_selected)+.5) (0+.5) (length(scans_selected)+.5) 0 MAX])
%eliminate redundant?
if   get(handles.RemoveRedundant,'Value')==1
   Comp=tril(ER)';
else
   Comp=ER;
end
th=Threshold;
tl=.005;
%Apply threshold from textbox
for i=1:size(Comp,1)
   for j=1:size(Comp,1)
      if get(handles.relativeTH,'Value')==1
         if Comp(i,j)<th && Comp(i,j)>0
            Comp(i,j)=.001;
            drawcolum(i,j,Comp(i,j),MAX*1.1,border,handles)
         elseif Comp(i,j)>0
            Comp(i,j)=1;
            drawcolum(i,j,Comp(i,j),MAX*1.1,border,handles)
         end
```

```
            else
               if Comp(i,j)~=0
                  drawcolum(i,j,Comp(i,j),MAX*1.1,border,handles)
               end
            end
         end
      end
      Results=Results+Comp;
      title(['Inspection Location ' num2str(p)],'FontSize',12)
         axis([(0+.5) (length(scans_selected)+.5) (0+.5) (length(scans_selected)+.5) 0 1])
         VIEW(0,90)
      if get(handles.relativeTH,'Value')==1
         axis([(0+.5) (length(scans_selected)+.5) (0+.5) (length(scans_selected)+.5) 0 1])
         VIEW(0,90)
      end
      set(gca,'XTick',0:1:length(scans_selected))
      set(gca,'YTick',0:1:length(scans_selected))
      end
      end
%_____________________________________________________________________________
%_________________Maxumum SSC Matrix and S(j)Values___________________________
%_____________________________________________________________________________
      border=1;
%make max SSC matrix
      if get(handles.AllPoints,'Value')==1
         if   get(handles.RemoveRedundant,'Value')==1
            MAX_ER=tril(max(ER_ALL,[],3))';
         else
            MAX_ER=(max(ER_ALL,[],3));
         end
      MAX=max(max(MAX_ER));
      figure
      th=1;
      th=Threshold;
      tl=.1;
%Plot Max SSC Matrix
      for i=1:size(MAX_ER,1)
         for j=1:size(MAX_ER,1)
            if get(handles.relativeTH,'Value')==1
               if MAX_ER(i,j)<th && MAX_ER(i,j)>0
```

```
                MAX_ER(i,j)=.001;
                drawcolum(i,j,MAX_ER(i,j),MAX*1.1,border,handles)
            elseif MAX_ER(i,j)>0
                MAX_ER(i,j)=1;
                drawcolum(i,j,MAX_ER(i,j),MAX*1.1,border,handles)
            end
        else
            if MAX_ER(i,j)~=0
                drawcolum(i,j,MAX_ER(i,j),MAX*1.1,border,handles)
            end
        end
    end
end
set(gca,'XTick',0:1:length(scans_selected))
set(gca,'YTick',0:1:length(scans_selected))
% Uncoment to Show Name of Devices
%    set(gca,'XTickLabel',scan_names,'FontSize',10)
%    set(gca,'YTickLabel',scan_names,'FontSize',10)
xlabel('Reference Device #','FontSize',10)
ylabel('Test Device #','FontSize',10)
zlabel('Maximum Correlation Coefficient','FontSize',12)
title('Maximum Value For All Inspection Locations','FontSize',10)
axis([(0+.5) (length(scans_selected)+.5) (0+.5) (length(scans_selected)+.5) 0 1])
VIEW(0,90)

% S(j) Values
figure
for ref=1:size(Results,1)
    for com=1:size(Results,1)
    DeviceCom(ref,com)=sum(ER_ALL(ref,com,:));
    end
end
for i=1:size(Results,1)
    S(i,1)=sum(DeviceCom(i,:));
end
%Plot S(j) values
for d=1:size(Results,1)
        drawcolum2(1,d,S(d,1),max(max(S))*1.1,1,handles,1)
end
title('Sum of All Correlations','FontSize',14)
```

```
    ylabel('Reference Device #','FontSize',14)
    zlabel('S(j)','FontSize',14)
    axis([(0+.5) (1+.5) (0+.5) (length(scans_selected)+.5) 0 max(max(S))*1.1])
    set(gca,'YTick',0:1:length(scans_selected))
    VIEW(90,0)
%Draw Threshold Statistics Lines
    line([1.5,1.5],[0,size(Results,1)+.5],[mean(S),mean(S)],'LineWidth',2)

line([1.5,1.5],[0,size(Results,1)+.5],[mean(S)+std(S),mean(S)+std(S)],'LineWidth',2,'Line
Style','-.')
    line([1.5,1.5],[0,size(Results,1)+.5],[mean(S)-std(S),mean(S)-
std(S)],'LineWidth',2,'LineStyle','-.')
%Legend
    for leg=1:size(Results,1)
        legend_string(leg)=scan_names(leg+1)
    end
    legend_string(leg+1)={'Mean S(j)'};
    legend_string(leg+2)={' + 1 std'};
    legend_string(leg+3)={' - 1 std'};
    legend(legend_string)
    end

%_____________________________________________________________________
%_____________________Plot Analysis Comparisons_____________________
%_____________________________________________________________________
if get(handles.AnalysisPlot,'Value')==1
    for ref=1:size(Results,1)
        for com=1:size(Results,1)
        DeviceCom(ref,com)=sum(ER_ALL(ref,com,:));
        end
    end
%plot MAX SSC Matrix
    figure
    MAX=max(max(DeviceCom));
    for ref=1:size(Results,1)
        for com=1:size(Results,1)
        if DeviceCom(ref,com)>0
            drawcolum(ref,com,DeviceCom(ref,com),MAX*1.1,border,handles)
        end
        end
```

```
    end
    set(gca,'XTick',0:1:length(scans_selected))
    set(gca,'YTick',0:1:length(scans_selected))
    xlabel('Reference Device #','FontSize',10)
    ylabel('Test Device #','FontSize',10)
    title('Maximum Value For All Inspection Locations','FontSize',10)
    axis([(0+.5) (length(scans_selected)+.5) (0+.5) (length(scans_selected)+.5) 0 1])
    VIEW(0,90)

%Calculate S(j) values
    for i=1:size(Results,1)
        S(i,1)=sum(DeviceCom(i,:));
    end

%Analyse initial devices
    initial=5;   %initial devices
    if size(Results,1)<initial
        initial=size(Results,1);
    end
    devices=1;
    GoodCount=0;
    window=mean(S(1:initial))+str2num(get(handles.TH2,'string'))*std(S(1:initial));
    for device=1:initial
        if S(device,1)<=window
        devices_2_selected(1,devices)=scans_selected(1,device);
        devices=devices+1;
        GoodCount=GoodCount+1;
        NewS(GoodCount,1)=S(device,1);
        end
    end
%analyse remaining devices
    for device=initial+1:size(Results,1)

window=mean(NewS(1:GoodCount))+str2num(get(handles.TH2,'string'))*std(NewS(1:G
oodCount));
        win(device)=window;
        if S(device,1)<=window
                devices_2_selected(1,devices)=scans_selected(1,device);
                NewS(devices,1)=S(device,1);
                GoodCount=GoodCount+1;
```

```
            devices=devices+1;
        end
    end
%Final Window
    window=mean(NewS)+str2num(get(handles.TH2,'string'))*std(NewS);
%Draw colums for each device
    figure
    devices=1;
    for d=1:size(Results,1)
        if S(d,1)<=(window)
            devices_3_selected(1,devices)=scans_selected(1,d);
            devices=devices+1;
            drawcolum2(1,d,S(d,1),max(max(S))*1.1,1,handles,1)
        else
            drawcolum3(1,d,S(d,1),max(max(S))*1.1,1,handles,0)
        end
    end
    title('Sum of All Correlations','FontSize',14)
    ylabel('Reference Device #','FontSize',14)
    zlabel('S(j)','FontSize',14)
    axis([(0+.5) (1+.5) (0+.5) (length(scans_selected)+.5) 0 max(max(S))*1.1])
    set(gca,'YTick',0:1:length(scans_selected))
    VIEW(90,0)
%Draw Threshold Line
    line([1.5,1.5],[0,size(Results,1)+.5],[window,window],'LineWidth',2)
    %Legend
    for leg=1:size(Results,1)
        legend_string(leg)=scan_names(leg+1)
    end
    legend_string(leg+1)={'Threshold'};
    legend(legend_string,'FontSize',12)
    end
%select devices in GUI Window
    devices_selected=devices_3_selected;
end
```

D.2 3D Bar Plotting Function

```
function drawcolum(x,y,height,th,border,handles)

location=[x,y];
width=1;

map=colormap('autumn');
% map=colormap('jet');
% map=colormap('hot');

col=map(  64- (round(height/th*64)+1)    ,:);
% col=map(   (ceil(height/th*64)+1)    ,:);
a=col(1,1);
b=col(1,2);
c=col(1,3);


X1=location(1,1)+width/2;
X2=location(1,1)-width/2;
Y1=location(1,2)+width/2;
Y2=location(1,2)-width/2;
Z=0;
Z=height;


vert = [X1 Y1 0
       X2 Y1 0
       X1 Y2 0
       X2 Y2 0
       X1 Y1 Z
       X2 Y1 Z
       X1 Y2 Z
       X2 Y2 Z];

fac=     [4 8 7 3
         4 2 6 8
         3 1 5 7
         1 2 6 5
         5 6 8 7];
```

```
color= [a b c
        a b c
        a b c
        a b c
        a b c];

if border==0

patch('Faces',fac,'Vertices',vert,'FaceVertexCData',color,'FaceColor','flat','EdgeColor','no
ne')
else
    patch('Faces',fac,'Vertices',vert,'FaceVertexCData',color,'FaceColor','flat')
end
if get(handles.valueLabels,'Value')==1

text(location(1),location(2),height+.02,num2str(height,3),'HorizontalAlignment','center','
FontSize',12,'FontWeight','bold')
end
end
```

Appendix F: Results For The Inspection of Flip Chip Packages Using the Simultaneous Signal Comparison Method

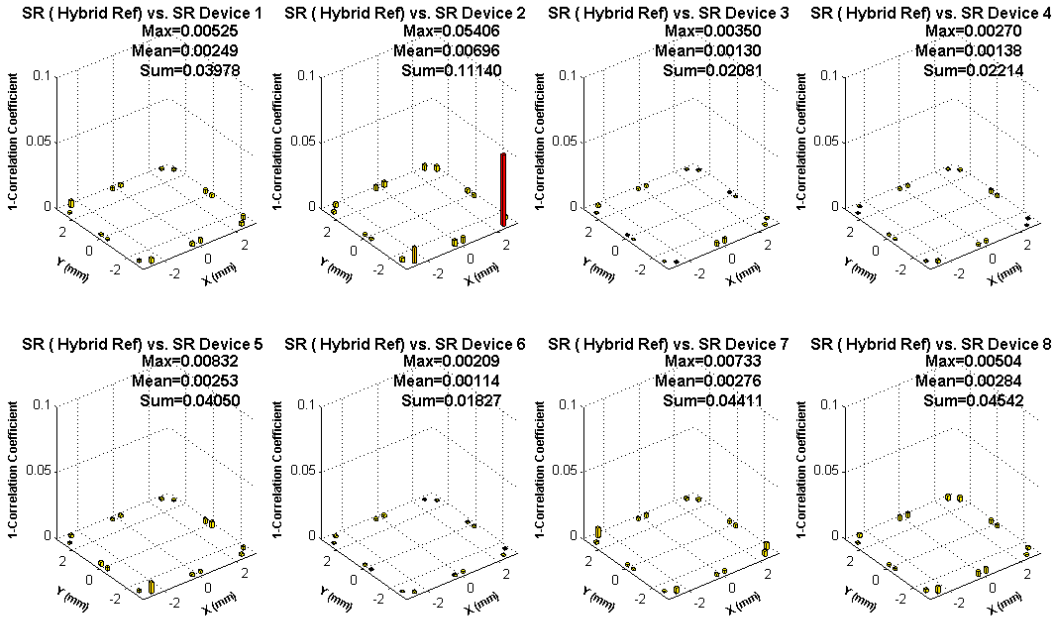

Figure F.2.a Individual MCC comparisons results for single reflow devices

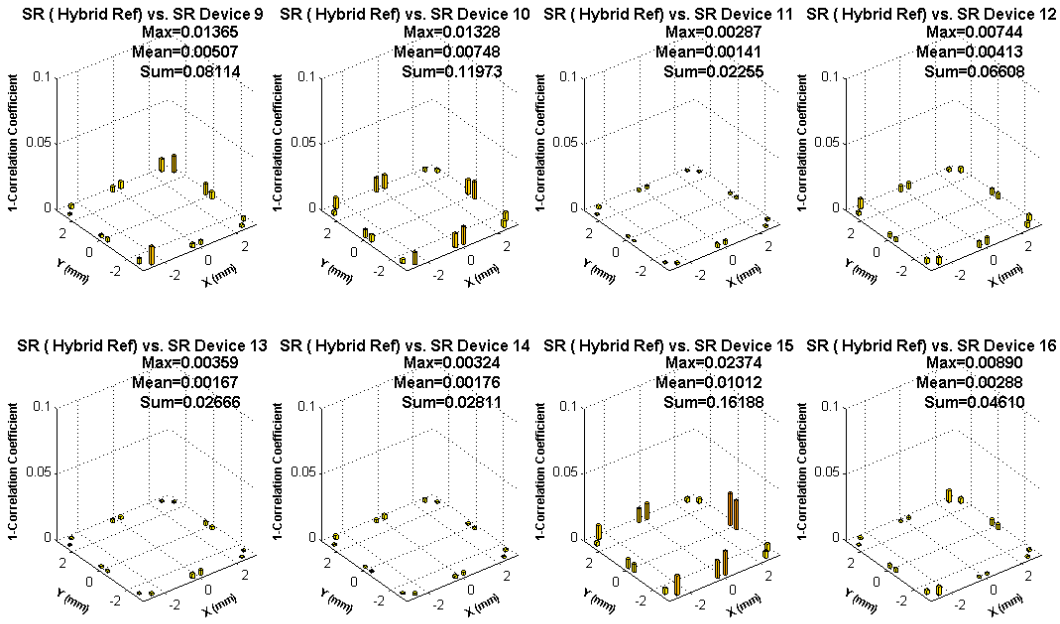

Figure F.2.b Individual MCC comparisons results for single reflow devices

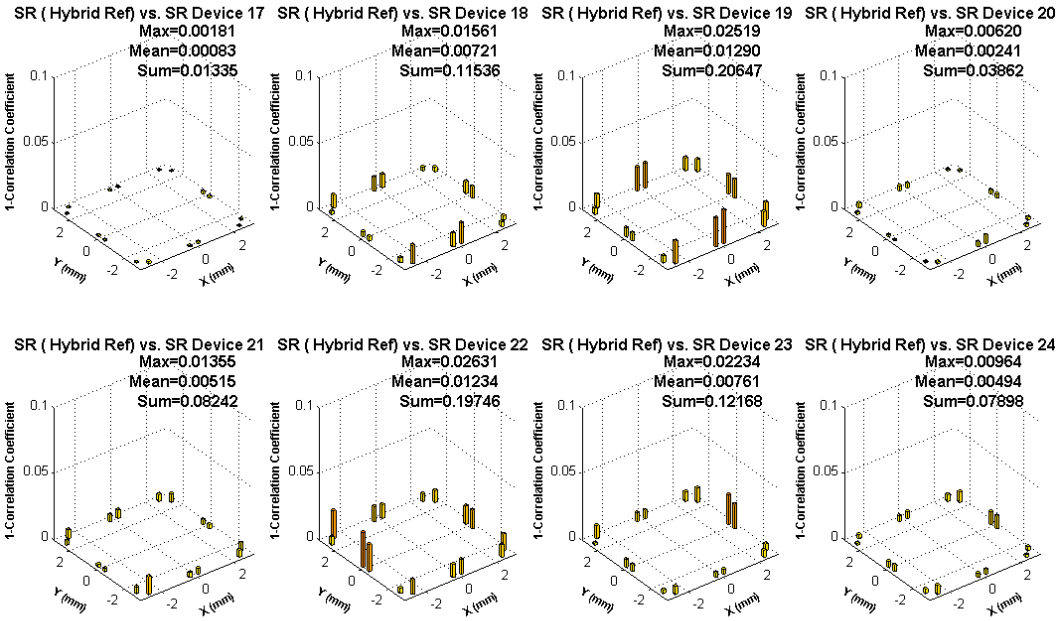

Figure F.2.c Individual MCC comparisons results for single reflow devices

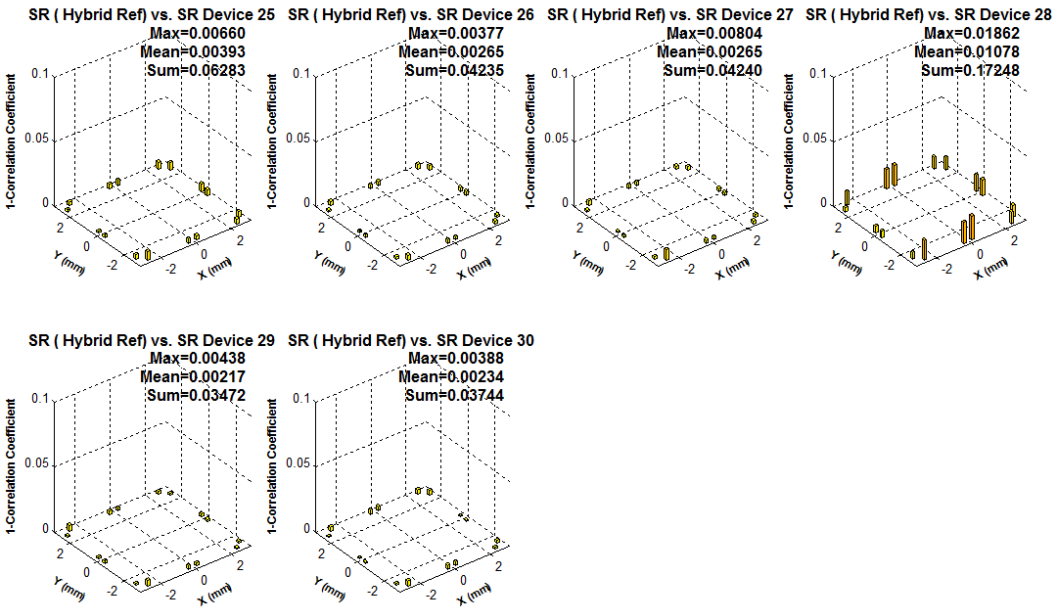

Figure F.2.d Individual MCC comparisons results for single reflow devices

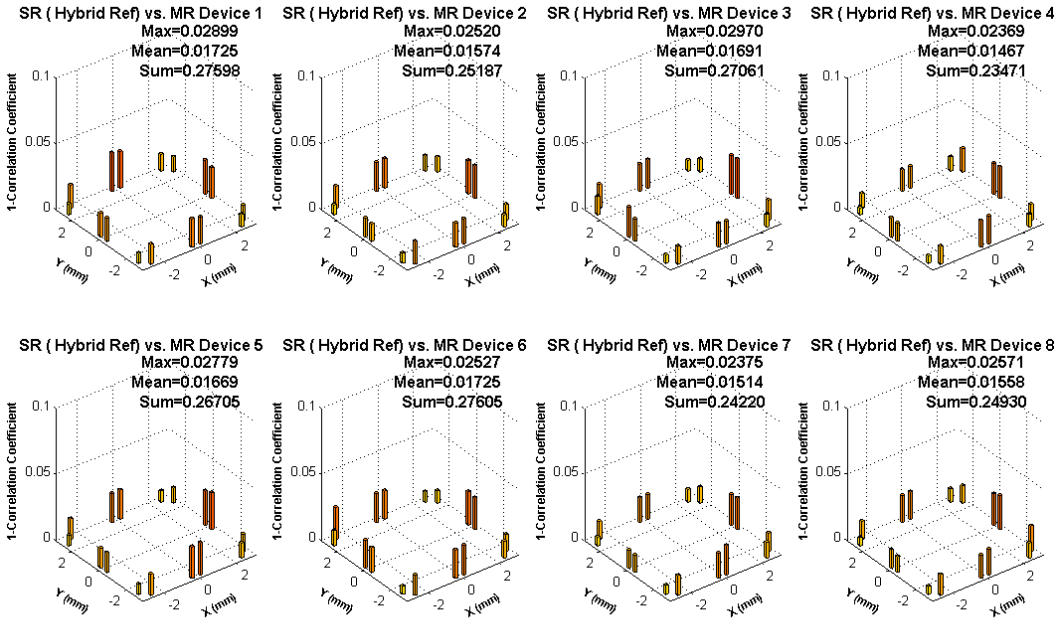

Figure F.3.a Individual MCC comparisons results for multiple reflow devices

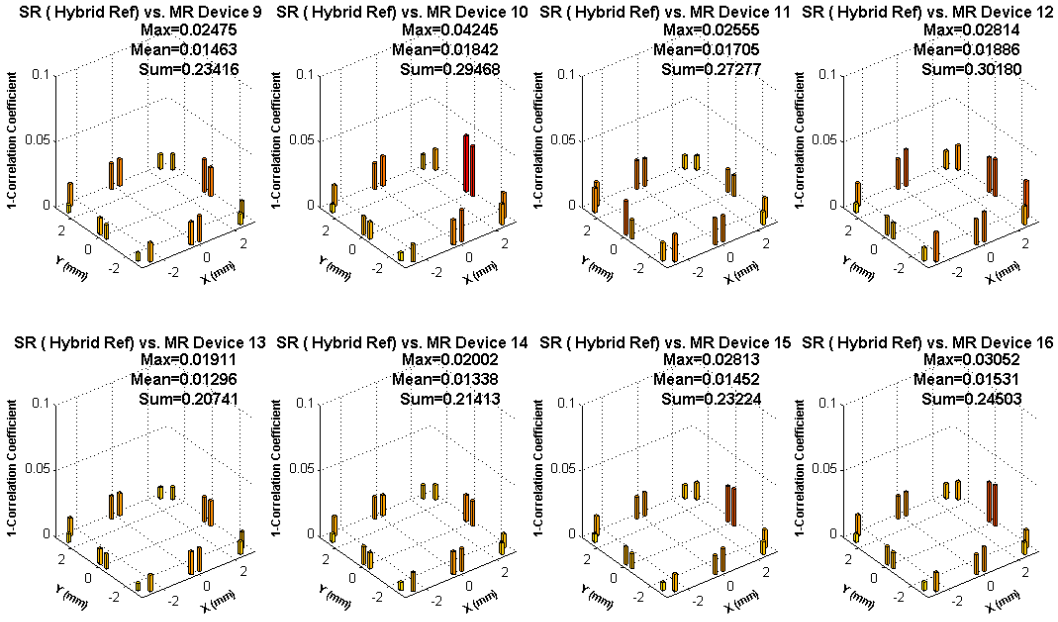

Figure F.3.b Individual MCC comparisons results for multiple reflow devices

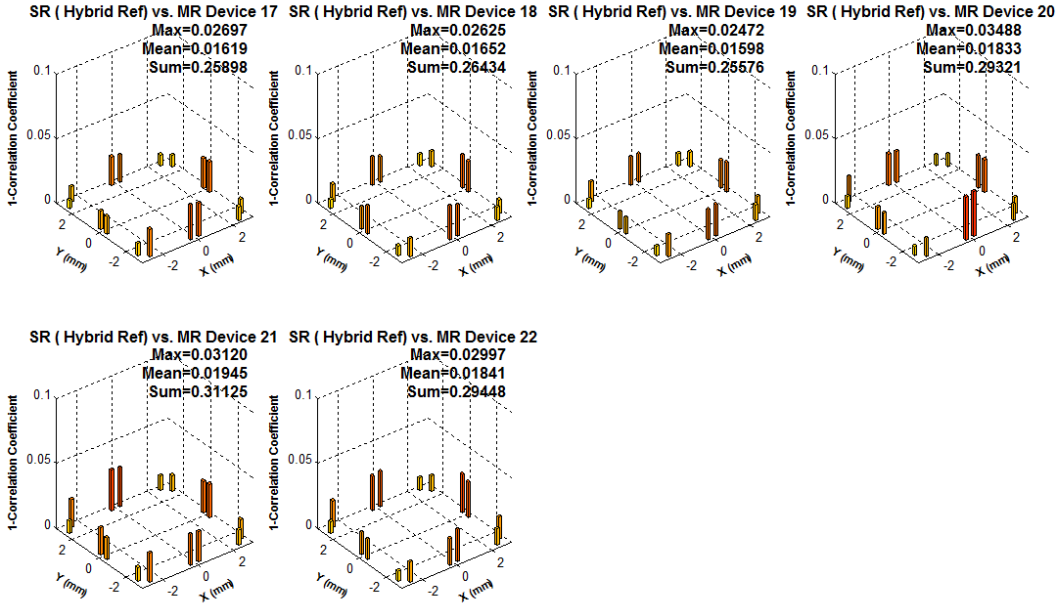

Figure F.3.c Individual MCC comparisons results for multiple reflow devices

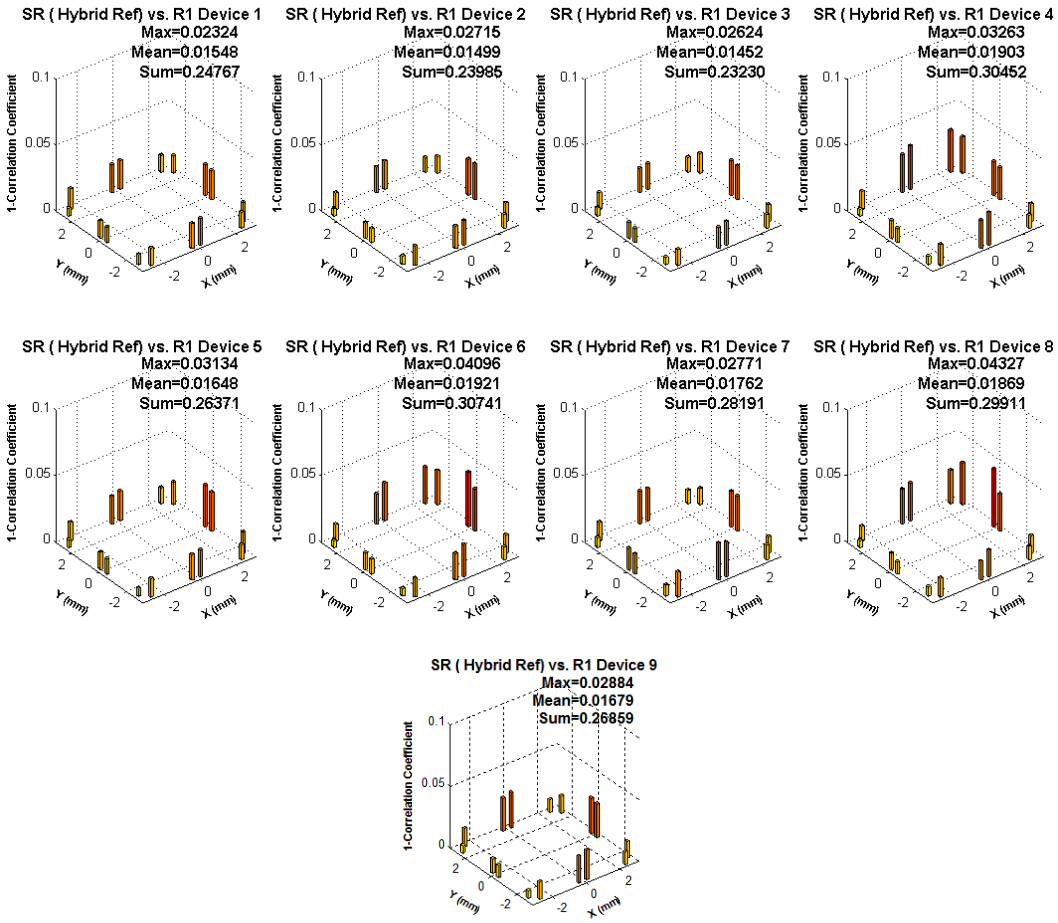

Figure F.4 Individual MCC comparisons results for rework type I devices

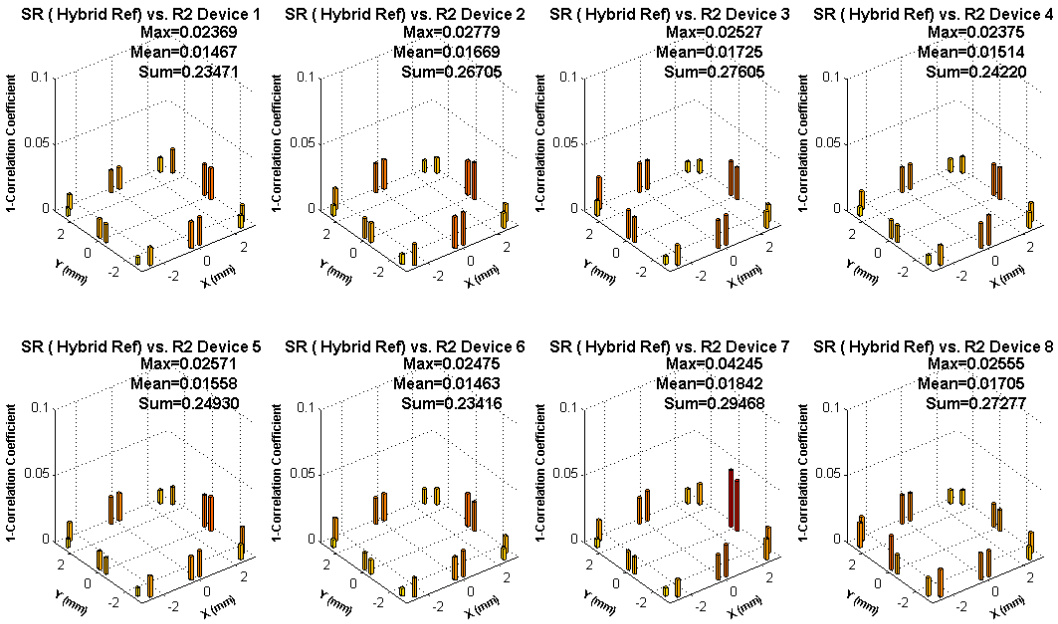

Figure F.5.a Individual MCC comparisons results for rework type II devices

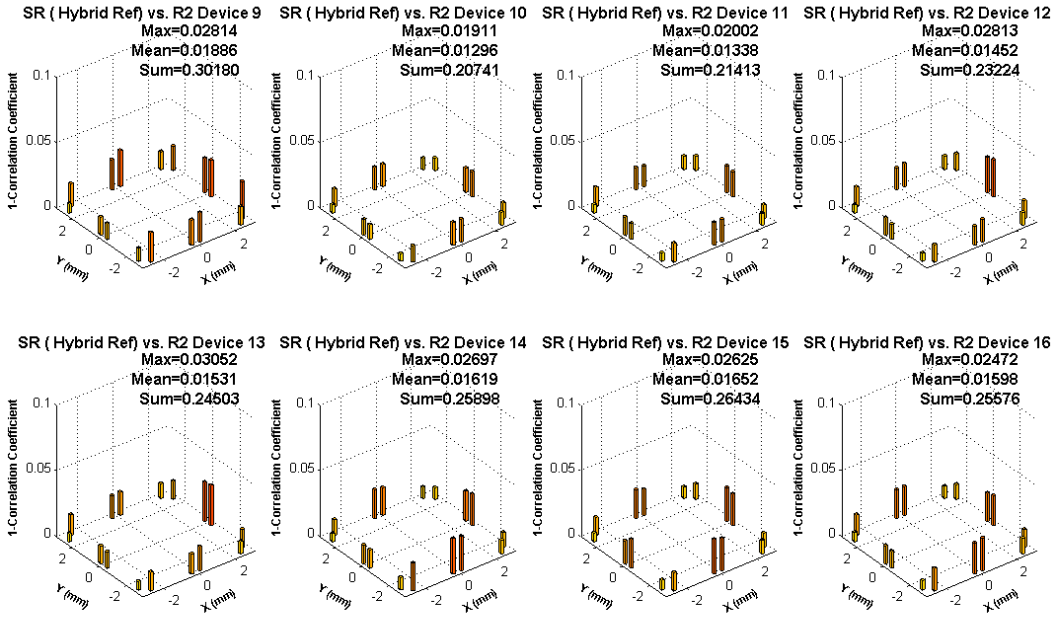

Figure F.5.b Individual MCC comparisons results for rework type II devices

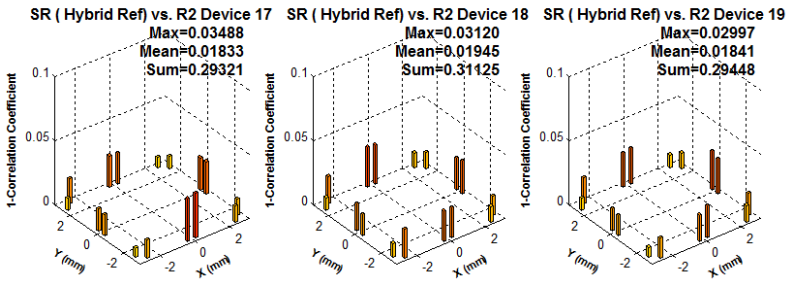

Figure F.5.c Individual MCC comparisons results for rework type II devices

References

B.Q. Xu, Z.H. Shen, X.W. Ni and J. Lu, Numerical simulation of laser-generated ultrasound by the finite element method, J Appl Phys 95 (2004) (4), pp. 2116–2122.

C.B. Scruby, R.J. Dewhurst, D.A. Hutchins and S.B. Palmer, Quantitative studies of thermally generated elastic waves in laser-irradiated metals, J Acoust Soc Am 51 (1980) (12), pp. 6210–6216 .

Davies, S. J., Edwards, C., Taylor, G. S. and Palmer, S. B., "Laser-generated ultrasound: its properties, mechanisms and multifarious applications". Applied Physics, Vol. 26, pp. 329 – 348, 1993.

Dixon, S., Edwards, C., Palmer, S. B., and Schindel D. W., "Ultrasound generation in single-crystal silicon using a pulsed Nd:YAG laser", vol. 29, no. 5, pp. 1345-1348, 1996

Erdahl D. S., and Ume C., "Determination of measurement limit for open solder bumps on a flip-chip package using a lser ultrasound inspection system," IEEE Tran. Compon. Packag., vol. pp, no. 99, pp. 1-8, 2005.

Goyal, D., "Introduction to the Special Issue Of Failure Analysis of Integrated Circuit Devices and Packages", IEEE Transactions on Device and Materials Reliability", Vol. 7, issue 1, page 3-4, March 2007.

Hald, H., Statistical Theory of Sampling By Attributes. Academic, London, 1981.

Howard, T., "Design of Advanced System for Inspection of Microelectronic Devices and Their Solder Interconnections Using Laser-Induced Vibration techniques", Master Thesis, Georgia Institute of Technology, July 2002.

Howard, T., "Design of an Advanced System for Inspection of Microelectronic Devices and Their Solder Connections Using Laser-Induced Vibration Techniques", Master Thesis, Georgia Institute of Technology, July 2002.

J.D. Aussel, A.L. Brun and J.C. Baboux, Generating acoustic waves by laser: theoretical and experimental study of the emission source, Ultrasounics 26 (1988), pp. 245–255.

Jian, L., Xaio-Wu, N., "Measurement of Thresholds of Damage to a Charge Coupled Device by a Q-Switched Laser", Microwave and Optical Technology Letters, Vol. 11 No.4, page 194-196.

Liu, S., “System Implementation, Modeling and Defect pattern Recognition for Flip Chip Solder Joint Inspection Using laser Techniques”, PhD Thesis, Georgia Institute of Technology, May 2001.

Liu, S., and Ume, C., “Digital signal processing in a novel flip chip solder joint defectsinspection system,” ASME J. Electron. Packag., vol. 125, pp. 39-43, Mar. 2003.

Liu, S., Erdahl, D., and Ume, C., “A Novel Approach for Flip Chip Solder Joint Quality Inspection: Laser ultrasound and Interferometric System,” IEEE Transactions on Component Packaging, Vol. 24, No. 4, page 616-624, Dec. 2006.

Liu, S., Erdahl, D., and Ume, C., “A novel approach for flip chip solder joint quality inspection: laser ultrasound and interferometer system,” IEEE Tran. Compon. Packag., vol. 24, no. 4, pp. 616-624, Dec. 2001.

Monchalin, J. P., (1986a) “Laser ultrasonic generation and optical detection a confocal Fabry-Perot interferometer”, Materials Evaluation, Vol. 44, September 1986, pp.1231-1237

Monchalin, J. P., (1986b) “Optical Detection of Ultrasound”, IEEE Transactions on Ultrasonics, Ferroelectrics, and Frequency Control, Vol. UFFC-33, No. 5, September 1986. pp. 485-499

Monchalin, J. P., Aussel1, J. D., Héon, R., Jen, C. K., Boudreault, A. and Bernier, R.,(1989) “Measurement of In-Plane and Out-of-Plane Ultrasonic Displacements by Optical Heterodyne Interferometry”, Journal of Nondestructive Evaluation, Vol. 8, No. 2. 1989, pp. 121-133

O’Conchuir, D., “Survey of non-Destructive inspection Methods for Solder joint Integrity”, Proceedings of IEEE National Aerospace and Electronic Conference, Vol. 3, page 1268-1275, May 1991.

R.J. Dewhurst, D.A. Hutchins and S.B. Palmer, Quantitative measurements of laser-generated acoustic waveforms, J Appl Phys 53 (1982) (6), pp. 4064–4071.

Randolph, T., “Development of High-Speed Autofocus Interferometric Inspection System”, Master Thesis, Georgia Institute of Technology, May 2009.

Scruby, C. B. and Drain, L. E., Laser Ultrasonics: Techniques and Applications. Adam Hilger, Bristol, 1990.

Tummala, R. R., Fundamentals of Microelectronic Packaging, McGraw-Hill, 2001.

Wang, J., Shen, Z., Xu, B., Ni X., Guan, J. and Lu, J., "Numerical Simulation of Laser-Generated Ultrasound in Non-metallic Material by Finite Element Method", Optics & Laser Technology, Vol. 39, page 806-813, 2007.

Wetheril, B.G., Sampling Inspection and Quality Control. Methuen, London, 1969.

Winchell, W. Inspection and Measurement in manufacturing. SME, Dearborn, 1996.

Xu, BQ., Z.H. Shen, X.W. Ni and J. Lu, Finite element model of laser-generated surface acoustic waves in coating–substrate system, J Appl Phys 95 (2004) (4), pp. 2109–2115.

Yang, J., "Quality Inspection and Reliability Study of Solder Bumps in Packaged Electronic Devices: using Laser Ultrasound and Finite Element Methods", PhD Dissertation, Georgia Institute of Technology, July 2008.

Zhang, L., "Development of Microelectronics Solder joint Inspection System: Modal Analysis, Finite Element Modeling, and Ultrasound Signal Processing", PhD Dissertation, Georgia Institute of Technology, May 2006.

Zhang, L., Ume, C., Gamalski, J., and Galuschki, K., "Detection of flip chip solder joint cracks using correlation coefficient and auto-comparison analyses of laser ultrasound signals," IEEE Tran. Compon. Packag., vol. 1, no. 3, pp. 1-7, March 2006.